Master thesis and internship[BR]- Master's thesis : Development of an advanced modelling tool for a four apertures nulling interferometer[BR]- Integration internship

Auteur : De Bortoli, Francesco
Promoteur(s) : Clermont, Lionel; Dandumont, Colin
Faculté : Faculté des Sciences appliquées
Diplôme : Master en ingénieur civil en aérospatiale, à finalité spécialisée en "aerospace engineering"
Année académique : 2024-2025
URI/URL : http://hdl.handle.net/2268.2/23213

University of Liège - School of Engineering and Computer Science

Development of an advanced modelling tool for a four apertures nulling interferometer

Francesco De Bortoli

Thesis supervisor:
Dr. Lionel Clermont

Thesis co-supervisor:
Colin Dandumont

Master's thesis completed in order to obtain the degree of
Master of Science in Aerospace Engineering by De Bortoli Francesco.

Academic year: 2024–2025

Acknowledgements

I would like to express my deepest gratitude to my supervisor, Dr. Lionel Clermont, for his guidance and support over these months, and for his valuable recommendations and suggestions, which crossed many fields of knowledge. I also wish to thank my co-supervisor, Colin Dandumont, whose contributions have been significant to this work.

My heartfelt thanks go as well to my colleague, Claudia Carboni, with whom I shared my two-year mobility programme in Belgium, and with whom I share many fond memories.

I am also grateful to the departments and communities of both institutions, Politecnico di Milano and Université de Liège, for their teaching, support, and the meaningful moments experienced throughout my studies. I will always be thankful for the opportunity to participate in the T.I.M.E. mobility programme, which enriched my academic journey and broadened my perspective.

To the many friends who stood by me, thank you for your presence and support. In strict alphabetical order: Andrea, Antonio, Gianluca, Gilles, Ginevra, Letizia, Maria Vittoria, Maxence, Omar, Pietro, and Quentin. Thank you for sharing both the challenges and the joys of these years, whether near or far.

Finally, a special thank you to my family, for their constant support, patience, and understanding. I would not be here without their strong encouragements.

Contents

1 Review of nulling interferometry for exoplanet detection: between bast and future **7**
- 1.1 Introduction . . . 7
- 1.2 Advantages of nulling interferometers . . . 8
- 1.3 Comparison with coronagraphy . . . 9
- 1.4 Spectrum regions and exoplanets . . . 10
- 1.5 Ground-based Interferometers . . . 12
- 1.6 Bracewell first concept and improvements . . . 16
- 1.7 Space-based Interferometers . . . 19
- 1.8 Conclusions . . . 22

2 Theoretical aspects and optical design considerations **23**
- 2.1 The wave behaviour of light . . . 23
- 2.2 Diffraction of waves . . . 24
- 2.3 Key Optical Components of an Interferometer . . . 25
- 2.4 Space environmental considerations . . . 29
- 2.5 Data processing and analysis . . . 32

3 Modelling of Interferometry **33**
- 3.1 Example configurations . . . 33
- 3.2 Interference Amplitude and Intensity . . . 34
- 3.3 Response Function . . . 36
- 3.4 Optimised Signal Splitting Strategies . . . 37
- 3.5 Transmission Maps and Phase Chopping . . . 40
- 3.6 Baseline Typologies and Configurations . . . 41
- 3.7 Nulling Ratio and Rejection Factor . . . 42
- 3.8 Analysis of the Point Spread Function . . . 44
- 3.9 Comparison of different arrays and final remarks . . . 48

4 Sensitivity Analysis **51**
- 4.1 Classification of systematic errors . . . 51
- 4.2 Instrumental stellar leakage . . . 52
- 4.3 Phase Sensitivity of the Interferometer . . . 55
- 4.4 Role of optical path distance in sensitivity . . . 58
- 4.5 Sensitivity to optical perturbations . . . 61
- 4.6 Conclusions . . . 65

5 Compensator impact on performances **67**
- 5.1 Compensator logic and design . . . 67
- 5.2 Comparison of improved results with compensator . . . 70

5.3 Interferogram analysis . . . 73
5.4 Overview of statistical analysis . . . 79
5.5 Perturbed comparison for multiple arrays . . . 84

6 Model validation **89**
6.1 Overview of the Three Missions: Literature Review and Model Setup . . . 89
6.2 Interferometer Array Design: Choices and Trade-offs . . . 90
6.3 Detecting Exoplanets: Performance and Capabilities . . . 94
6.4 Habitable Zone Analysis and Habitability Potential . . . 96

A Mathematical derivations **i**
A.1 Nulling ratio for a general interferometer . . . i
A.2 Approximate relations for instrumental leakage . . . ii
A.3 Period associated to the nulling ratio . . . iii

B Synthetic exoplanet populations with the P-Pop catalogue **v**
B.1 Overview of the tool . . . v
B.2 Output of the tool . . . v

Introduction

One of the frontiers of today's research is the search for life on other planets beyond Earth. This topic evolved over time, going from being a deep philosophical question, during periods when the scientific method was yet to be established, to being one of the most open aspects of astronomy, opening the road to astrobiology.

This kind of research involves several scientific and technical fields, which need to interface and combine in defining clear and attainable objectives and the tools that can be used to reach this important milestone in human knowledge and history.

It is a fact, however, that current research is limited by the available tools: while the detection of Earth-like planets is possible through many different tools, their characterisation is not, due to unachievable resolutions and difficulties to discern the planets from their host stars[74],[77].

Among the various detection techniques, the one that would allow achieving the desired accuracy is interferometry[57]. Yet limitations linked to atmospheric absorption of many regions of the spectrum[54], especially of the preferred infrared region[77], on one hand, and the complexities of deploying a nulling interferometer in space (despite some emerging projects like the Large Interferometer For Exoplanets, LIFE[91],[21]), on the other have so far prevented to see any practical results.

From the first feasibility analysis, however, technological levels have progressed enough so that it is possible that in the next decades space-based nulling interferometry will see the light and, in anticipation to that moment, this work will analyse the physical behaviour behind these techniques, presenting a mathematical model for their characterisation.

The quest of searching for life in space

Since the discovery of the first exoplanet around a main sequence star in 1995 by Mayor and Quelotz[54], the search for extraterrestrial life officially began and fast progress was rapidly gained with the perfectionism of many detection techniques, which in these years mainly revolved around indirect detection techniques through spectroscopic analysis.

In practice, while many results were achieved in short times with thousands of detections[57], the goal of astrobiology is still far from being reached: technical limitations of today's instruments are one side of the problem which will be partially overcome with the advent of new instruments like space based nulling interferometry, but the lack of deep knowledge on the origin of life opens the road to another side of the topic.

Effectively, many doubts are still left unanswered on the matter: what came first, the DNA or proteins? How "common" is life in the universe? Which astronomical features of the Solar System are hazards to life and which ones, on the contrary, sheltered it[54]?

Lacking sufficient information, the search field is very large, with only some supposition linked to metallicity profile of the galaxy allowing to discard the older population, narrow-

ing the field down to roughly 20% of the Milky Way population[54]. Within these candidate stars, the search for viable exoplanets must be conducted in the so-called habitable zone, being the zone around the star limited by runaway greenhouse and runaway glaciation of water, recognised as the key factor for having Earth-like life.

As in the case of the Solar System, where the habitable zone is generally assumed to be within 0.95 and 1.52 AU[74], it is clear that in the cosmological scales, such suitable planets are located very close to their host stars. While the detection is possible in many cases, exploiting transit or radial velocity methods among many others[74], problems arise when trying to characterise these planets.

In fact, it is clear that simply being in the habitable zone is not sufficient to harbour life: Mars is within the habitable zone, for example, but currently no satisfactory proof of present or past life has been found[54]. A characterisation of the planet must be conducted, with the determination, for example, of the atmospheric composition by looking at strong spectral signatures that can provide information on the state of the atmosphere: one of the most widely recognised gas are carbon dioxide and water vapour, but many other can be detected[74].

Besides that, the definitive proof for the presence of life would be the presence of biosignatures, those being the modifications to the planet induced by life: in the case of our planet, the two most clear examples are the presence of oxygen as a trace gas in the atmosphere (unique to Earth's atmosphere, at least in the Solar System) and chlorophyll over major extensions of surface[54]. Most of these features are best observed in the infrared domain (6-20 µm), which consequently (since the Earth itself, in first place, presents these gases) is one of the most affected regions by absorption phenomena.

Beside the fact that, in many cases, currently exoplanets cannot be resolved and the fact that prolonged observations of the same target, in order to acquire changing features, would be needed, planets lay too close to the harbouring stars and Rayleigh's limit resolution $\Delta\vartheta = 1.22\,\lambda/D$ would require excessively large telescopes to get even close to the required observation, especially in the infrared domain. The only possibility, then, is to use an interferometer, but again, ground observation, while certainly useful, is severely limited by the atmospheric absorption[3].

The role of nulling interferometry

Exploiting the coherent domain of light, interferometry is one of key techniques to combine signals under the wave nature of light: from Fraunhofer's diffraction the creation of fringes in a succession of constructive and destructive interferences leads to many considerations[47]. In addition, it can be proved that the use of multiple telescopes replaces the need of having a large diameter as this last parameter is replaced by the baseline, being the distance between different interferometers: in practice, the larger the baseline, the better the resolution[47],[2].

It is clear, then, that this technique has a very strong advantage. In addition, the possibility to use the fringes to cancel out the star signal (which would otherwise be considerably dominant over the faint signal of the planet), further explains the large interest in this field, despite the technical difficulties: required baselines demands complex deployable system, due to payload fairing limitations of today's launchers, and formation flying must be provided with very tight control[47].

Yet, there are other problems linked to the faint signal of the planet to be measured: the local zodiacal (interplanetary) dust cloud and the assumed exozodiacal dust are among the strongest disturbances, beside the stellar leakage, that would complicate the detection

of the target exoplanet[91]. To counteract on these disturbances, which are symmetric, as being diffused on the orbital plane of the star, different methods starting from Bracewell's rotating design have been proposed[21], beside the optimal placement of such space telescope at distances of 4 to 5 AU to avoid the local zodiacal dust cloud effect[77].

Other aspects, however, including off-axis stellar suppression, are not adequately addressed, as it will be discussed beyond. In this optic, then, multiple evolutions have been proposed, including Angel's Cross or multiple apertures architectures[3], opening different trade-offs in terms of achievable results.

Outline of the work

From this background, many roads can be explored. The purpose of this work is to provide a mathematical characterisation for a four-aperture nulling interferometer, taking into consideration the modelling aspects such as the definition of dependencies of commonly recognised figures of merit and the sensitivity to most disturbances.

Its goal is not to generate a valid, single design, but rather to create a model to study the response of a generic four-aperture system and its sensitivity to the different aspects that contribute to defining the resulting yields, in order to characterise the quality of present and future instruments.

The discussion starts with a review of the state of the art of nulling interferometry in Chapter 1. This chapter aims to provide a general overview of the concepts behind nulling interferometers and how they work compared to other techniques such as coronagraphy. It also presents the current state of ground-based nulling interferometry—an already validated technology—and the paths that have been taken in order to possibly bring these instruments to space.

Therefore, after a qualitative description, Chapter 2 introduces in detail the aspects of interest of an interferometer, providing a theoretical background that will be addressed in subsequent chapters in the formulation of the mathematical models. This chapter discusses the diffraction behaviour of light and how the different components of interferometry exploit it to obtain the desired behaviour.

The mathematical discussion of the working principles and main figures of merit of an interferometer is considered in Chapter 3. By defining two generic configurations for a four-aperture nulling interferometer, it is possible to compute different aspects, including the transmission maps, nulling ratio, inner and outer working angles, and modulation efficiency to visualise how and how well the interferometer works.

The shift from the ideal model presented in Chapter 3 to the reality of disturbances is addressed in Chapter 4 through an initial introduction and classification of disturbances and later the graphical representations of how fundamental elements like the nulling ratio and the modulation efficiency are modified by the main disturbance actor: the phase. Eventually, an introduction to simulated optical disturbances is tackled with the introduction of data from ray-tracing software.

From the conclusions of Chapter 4, it is quite clear that corrections are needed before any further consideration. This is why Chapter 5 provides an overview of possible strategies to implement a compensator in the analysis and how it affects the pupil plane visualisation and descriptors introduced in Chapter 3, such as the transmission maps and the point spread functions, as well as the potential exoplanet yield.

Eventually, Chapter 6 aims to provide a general validation of the model through the comparison of three arrays taken from the literature and discussed in Chapter 1. After a general validation and a study of how the array sizes affect different parameters of the

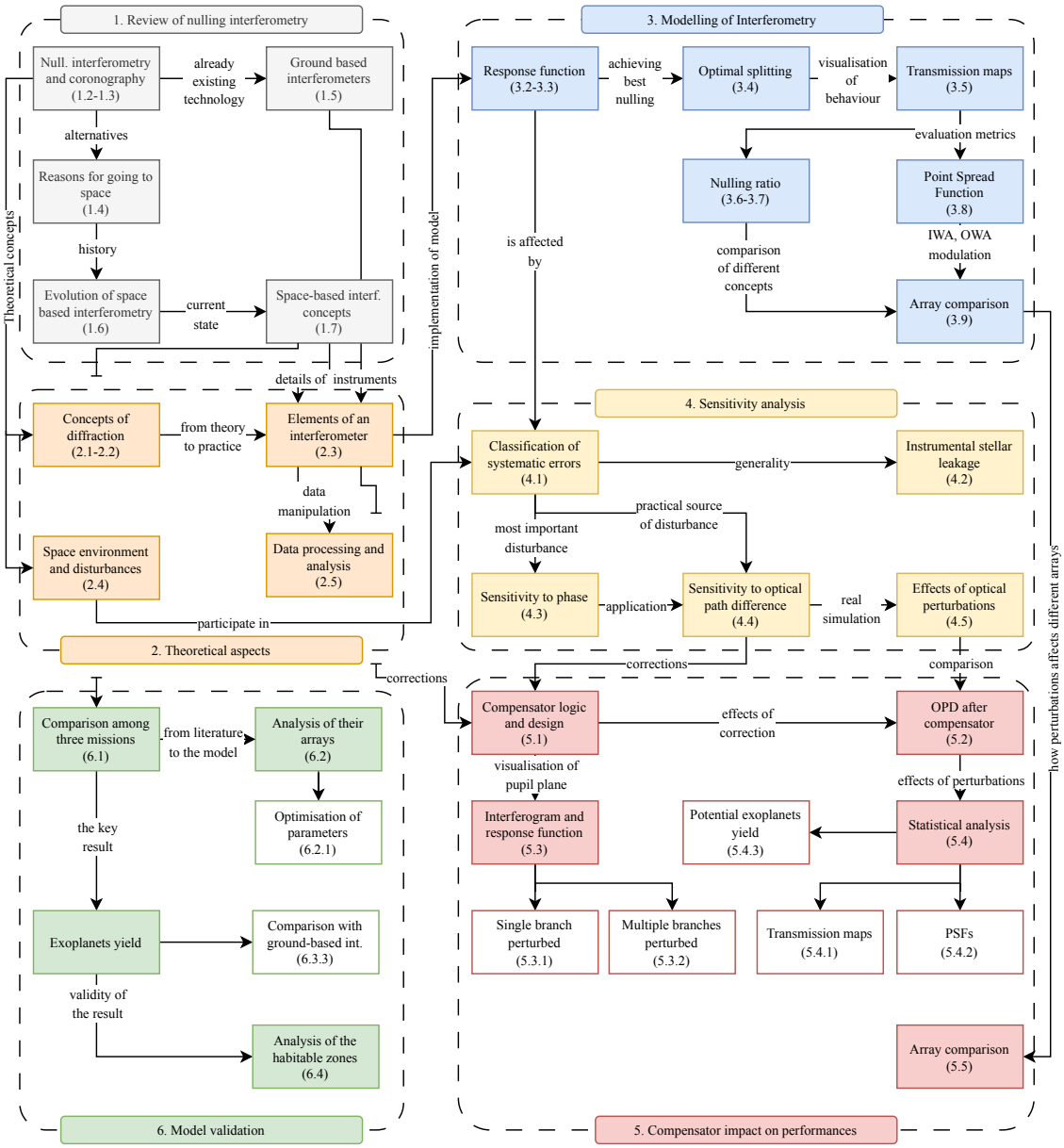

Figure 1: Roadmap of this work, with references to chapters and sections.

interferometry, a general discussion on the yield and its importance is addressed in order to once more validate the role of nulling interferometry in the scientific world.

Figure 1 provides a general roadmap of this work, focusing on the key concepts addressed in each chapter and how they are related to one another through a simple block scheme.

Shared development of an opto-mechanical design

The main focus of this work is the development of a mathematical model for nulling interferometry; in parallel to this work, another study on the development of an opto-mechanical design has been carried out by Claudia Carboni[13], providing a different point of view on the same overall project, with a more practical implementation involving optical considerations developed using Synopsys's CODE V[100] and preliminary design implementations using computer-aided design software.

Throughout the different chapters, several cross-references will be made due to the structure of the work which, especially in later chapters, will make use of some outputs from ray-tracing analysis. Some chapters, notably Chapter 1 and Chapter 5, have been co-authored by Carboni and appear similarly in their work.

In particular, Chapter 1 allowed the creation of a common knowledge ground upon which the two different works could be built, as well as to summarise a topic that has already been addressed multiple times.

While Carboni's work focused more on the creation of an optical model in order to visualise how perturbations affected their design, this work will mainly focus on the implementation of mathematical models valid for N-aperture nulling interferometers and their verification on a generic four-aperture system.

The effects of Carboni's optical model on the system are evaluated using the tools implemented in this work in Chapter 5: a comparison between the nominal system (addressed in Chapter 3) and the disturbed one allows the limits of currently available technology to be observed, as well as how well the system reacts to unwanted effects.

Once more, the two works diverge, with a mechanical model in Carboni's work and the validation of the tools and considerations on the scientific validity of the tool in this work, eventually producing two distinct but complementary analyses on nulling interferometry.

1 Review of nulling interferometry for exoplanet detection: between bast and future

State of the art of nulling interferometry

Note:

This chapter has been co-authored with Claudia Carboni in order to provide the shared ground base and start points on general knowledge on the theme for the developments of the two analyses with the goal of introducing the context of nulling interferometry for exoplanets detection and its relevance in the scientific world.

Abstract:

Detecting and characterising extrasolar planets is one of the most challenging and exciting frontiers in astronomy. Among the various techniques available, nulling interferometry stands alone in its ability to directly identify Earth-like exoplanets and analyse their atmospheric composition. This chapter begins by exploring the fundamental principles of nulling interferometry and its unparalleled advantages, particularly in isolating an exoplanet's spectral signature while suppressing the light glare of its host star. The study then transitions to a comprehensive overview of ground-based interferometers, followed by a comparative analysis of modern optical/infrared interferometers sets the stage for future innovations. However, the fundamental limitations of ground-based observatories—primarily atmospheric absorption and scintillation—highlight the inevitable shift toward space-based solutions. The second part of this chapter delves into the evolution of space-based interferometry, tracing its roots from Bracewell's original concept to refined mission proposals by ESA and NASA. Ultimately, the promising potential of nulling interferometry in exoplanet research is highlighted. As technological advancements continue to bring ambitious space-based concepts closer to reality, a new era of exoplanet discovery may be on the horizon—one that could finally unveil the atmospheres of distant Earth-like worlds.

1.1 Introduction

One of the major milestones in scientific research was reached in 1995 with the discovery of the first exoplanet around a main sequence star by Mayor and Queloz, using an indirect method (the radial velocity method)[31]. Since then, new scientific horizons have gained momentum in trying to answer the next obvious question: is there life outside Earth?

Nowadays, we are still awaiting answers, but besides philosophical considerations that have accompanied mankind throughout its history, technological progress could possibly aid us in this research: in effect, in recent years, missions like Kepler have significantly increased the number of detected exoplanets through the use of indirect methods.

However, simple detection is not enough, and the optical limitations of single apertures greatly reduce the amount of data that can be extracted from smaller exoplanets: while coronagraphy can be employed to image hotter, bigger, more distant (to their host star) exoplanets, the ones that could theoretically harbour life are outside the achievable angular resolution limits. Given the novelty of the topic, as well as the complexity of the matter, at the moment, almost nothing can be said about such planets: how they look like, what features do they present and so on are all open questions. Luckily, the potential of interferometry could change that, thanks to the simulated aperture and the nulling achievable to reduce the star's influence on the data. This work aims to provide a state-of-the-art overview of its current development.

After a brief introduction to the physics behind nulling interferometry, considerations on why this technique is complementary to single-aperture telescopes and motivations on why the mid-infrared region is preferred for research are presented. Ground-based and space-based interferometers of interest are then introduced, along with some considerations on their implementation and development processes. It must be highlighted that, while ground-based interferometry is today a valid instrument (albeit still in development), besides the problematic presence of the atmosphere, none of the studied space-based ones has ever reached a development phase due to the not-yet-mature technologies involved.

The flow of time, however, has brought advancements in the readiness levels of the involved instruments[20],[17]. While important challenges are still considered significant roadblocks in the development of future missions, it is probable that, in the coming years, the full potential of this technology will be realised.

1.2 Advantages of nulling interferometers

Rayleigh's criterion introduces a limitation on a telescope's ability to resolve two closely separated objects. In fact, two objects are distinguished if their angular separation is larger than

$$\Delta\vartheta \geqslant 1.22\frac{\lambda}{D}, \tag{1.1}$$

where λ is the wavelength and D is the diameter of the telescope. This specific value corresponds to the radius of the Airy disc: in order to be resolved, the images of two point sources, being Airy discs, must be such that the centre of one of them is located, at least, at the minimum of the other[47].

The linearity (at least to some extent: non-linear optics does not apply to traditional sources, whose flux densities are not high enough to produce a significant non-linear effect[47]) of the fields that constitute light allows for the existence of the superposition principle of the wave nature of light. This principle states that, given two separate waves at the same place, the resulting wave is simply given by the algebraic sum of the two original waves[47], leading to the possibility of interference.

Interference is, in fact, the key factor in the interferometry process, as the two waves can produce both in-phase and out-of-phase interference, meaning they can be reinforced or annihilated, producing visual effects known as fringes.

The principle of nulling interferometry is to combine the light received by a pair (or more)

Telescopes	**Diameter** [m]	**Wavelength** [µm]	**Limit resolution** [mas]
Spitzer[105]	0.85	3.57	1057
HSO[89]	3.28	363	27850
JWST[38]	6.6	5.6	213.52
GMT[7]	25.4	0.32-25†	2.5937
TMT[86]	30	0.31-28†	2.1314
ELT[33]	39	3-5†	15.866

Table 1.1: Survey of the limit resolutions for different single-aperture infrared telescopes from their parameters: the diameter and the wavelength. The first three entries are existing telescopes, the remaining ones future ones. †When an interval was provided, the best (smallest) value has been taken.

of telescopes in such a way that, when the optical path difference (OPD) between the incoming beams is zero, an achromatic phase shift is applied to create the phase opposition in the line-of-sight of the interferometer and suppress the starlight. However, off-axis sources positioned near constructive fringe maxima can still pass through the system. As a result, while the star is strongly suppressed, planets in favourable locations remain largely unaffected. The key challenge is to design an optical setup that can effectively null starlight across all polarizations and wavelengths within the desired passband[64].

Therefore, in order to detect exoplanets two main problems, among others, have to be solved: the high contrast which require a broad dynamic range and the need for a high angular resolution.

It is assumed that the general angular separation between an Earth-like exoplanet and its star would be below 100 mas[103] and, for example, in the case of Proxima b, being the closest exoplanet, the angular separation is around 37 mas[71]. This requirement is particularly stringent, meaning that currently existing telescopes, as illustrated in Table 1.1, are not able to meet it. Additionally, it is clear that, to reach a sufficient diameter, like that of future telescopes meeting these requirements, the payload size would vastly exceed the fairing of current-generation launchers.

As explained in Section 1.4, however, ground-based instruments are not a viable solution, as they would not be able to offer full-spectrum observations due to absorption windows. Alternative solutions are therefore needed in the domain of interferometry.

Similarly to how Equation 1.1 has been derived—i.e., by looking at the minimum of the Bessel function describing the Airy disc or the diffraction pattern—it can be shown that the angular resolution limit for an interferometer is given by the ratio of the wavelength to the baseline, which acts as an "effective aperture" of the system:

$$\Delta\vartheta \approx 1.22\frac{\lambda}{B}. \tag{1.2}$$

It is easy to see, then, why this technique is superior to single-aperture telescopes for detecting close objects, such as planets within the habitable zone of their host star: if for example VLTI (that will be analysed in Section 1.5.3) is taken into consideration, its 200 m baseline makes it behave like a 200 m classical telescope aperture.

1.3 Comparison with coronagraphy

The last entry in Table 1.1 reports data for the Extremely Large Telescope and one of its instruments, METIS (Mid-infrared ELT Imager and Spectrograph)[33]. This instrument

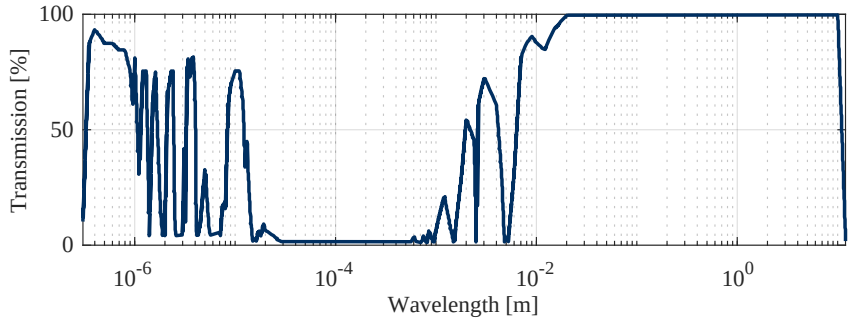

Figure 1.1: Transmission windows of Earth's atmosphere: the main limitation of ground observation is the wide presence of absorption windows due to the composition of the atmosphere. Below 0.3 µm, absorption is complete due to ozone, oxygen, and nitrogen, while above 10 m, scattering of the ionosphere closes that region[54].

has been developed to be used with the aid of a coronagraph, which has been seen as a viable and easier-to-implement alternative to nulling interferometry.

Born as a technique to study the solar corona (hence the name), coronagraphy is a technique that consists of placing a shade in front of the instrument, located at the position of the undesired source. In the case of the Sun, for example, the shade is designed to block the photospheric emissions while allowing the much fainter signals coming from the corona to reach the detector. In the case of exoplanet detection, based on the same principle, the idea is to place the shade in front of the harbouring star.

For this reason, as will be presented later in Section 1.7.2, coronagraphy has been in competition with nulling interferometry for some missions, including NASA's Terrestrial Planet Finder[62]. However, while this technique has been able to image some exoplanets, it does nothing to improve the angular separation of the instrument, making it unfit for detecting very narrow angular separations.

1.4 Spectrum regions and exoplanets

It is common to subdivide the light spectrum into different regions, following different wavelength or frequency intervals. In modern astronomy, each region of the spectrum carries the same importance, showing different effects and contributing to the multi-messenger approach that is currently adopted in the description of important phenomena, some more important than others depending on the application.

Ideally, then, a complete, continuous spectrum is the result of many different actors that emit (as in the case of stars, which act as close as possible to a black body emission), absorb (as for the interstellar medium and dark matter), or modify the spectrum (with contributions from cosmological redshift and the Doppler phenomenon). Exoplanets, too, contribute to the light spectrum reaching the Earth through their emission spectrum (being a function of their effective temperature and emissivity, a normalised parameter which quantifies how far the planet's behaviour deviates from that of a black body) and the reflected light from their host star.

A hyperspectral analysis would allow a deep characterisation of any space region, but many obstacles arise in this type of analysis. On the ground, where space and reliability are less concerning aspects compared to a satellite, the absorption windows, represented in Figure 1.1, originate from the atmospheric composition and simply render some regions completely opaque to external signals. In addition to this, scintillation is a phenomenon that severely diminishes the utility of ground observation with respect to very distant

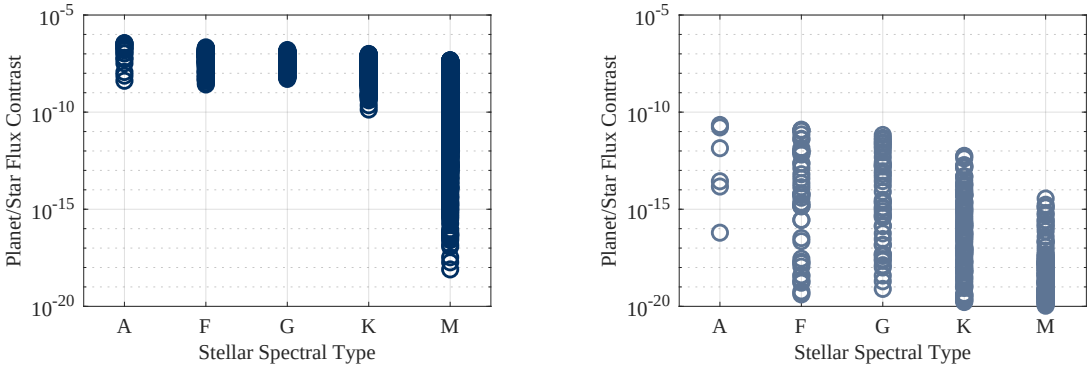

(a) Infrared (10 µm) **(b)** Visible (550 nm)

Figure 1.2: Comparison of the achievable flux ratio between the planet and star flux based on the P-Pop exoplanet population at two different wavelengths[52]. The planet flux includes only the thermal emissions, neglecting any reflection.

sources[54].

To avoid these severe problems, going to space is the only viable solution: in space, scintillation, which is due to turbulent phenomena in the atmosphere, is completely absent, while absorption is only linked to astronomical effects.

The selection of the wavelength is the next important step. It is important to recall that exoplanets are very faint objects in a bright sky. Indeed, nulling interferometry allows for a certain level of suppression of the light of harbouring stars, but stellar leakage will be present in any case.

Following Planck's and Wien's laws, then, it is easy to verify that, assuming Earth-like planets, the best region for observations is the infrared. In fact, following the latter, planets that have an effective temperature comparable to that of our planet display a peak in the mid-infrared region (specifically, for a body which an Earth's comparable temperature, the peak would be around 10 µm), while stars, depending on their class, usually peak at significantly higher frequencies.

This concept is also displayed in Figure 1.2, which shows the contrast level for different simulated exoplanets (generated by the P-Pop catalogue[52]) both in the infrared and visible region: the emissions at the given wavelengths have been computed using Planck's law (neglecting therefore reflections of stellar light by the exoplanets), deriving the ratio. By adopting the same scale on the ordinate range, it is clear that the infrared region allows for far better ratios than the visible range, at least for some of the considered stars.

Even considering that, however, contrasts of 10^{-7} are not enough[4], and levels of 10^{-6} or higher are deemed necessary to effectively detect exoplanets[77]. It is clear, then, that the number of actually detectable exoplanets is severely limited due to the hostile conditions in which such systems will operate.

Besides practical considerations on limitations in detection, the infrared region is particularly remarkable for scientific observations: the atmosphere and, ideally, the surface of exoplanets mostly exhibit signatures in the infrared region[57]. Detections of elements like carbon dioxide, ozone, methane and waters are of great interest in the characterisations of habitability of the planet, hinting at a possible water cycle, radiation shielding and even biosignatures (methane is in fact unstable, as it quickly oxidises, being present on Earth due to bioactivity[20],[58]).

1.5 Ground-based Interferometers

As explained in Section 1.2, interferometric arrays give access to angular resolution scales completely out of reach of single telescopes. In fact, such arrays, to some extent, behave as a huge telescope whose aperture is that of the physical extension of the array on the ground. One of the first ground-base interferometer is the Keck Interferometer (KI), located near the summit of Mauna Kea on the island of Hawaii. Other two examples are the Large Binocular Telescope Interferometer (LBTI) on Mount Graham in Arizona, USA and the Very Large Telescope Interferometer (VLTI) on Cerro Paranal in the Atacama Desert of northern Chile. The different locations around the globe allow for a wider coverage of the observable sky.

Figure 1.3: Picture of the Keck Telescope. Credits: NASA[80].

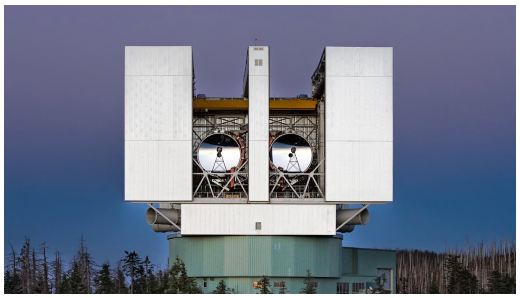

Figure 1.4: Picture of the Large Binocular Telescope Interferometer. Credits: Large Binocular Telescope Observatory[81].

1.5.1 KI

The two 10-metre telescopes of the W. M. Keck Observatory (Figure 1.3) are characterised by primary mirror comprising 36 hexagonal segments, each 1.8 m across the corners. The maximum diameter of the primary is 10.95 m and its focal length is 17.5 m. The telescope aperture area is equivalent to a circular aperture 9.96 m in diameter. The average optical performance of the segments (in combination with the f/15 secondary and the tertiary mirror) is such as to concentrate 80% of a star image within 400 mas diameter[55].

The mirror segments are maintained in mutual alignment both in angle and in position, using measurements of relative axial positions of neighbouring segments, with capacitive sensors accurate to about 5 nm[55].

KI utilized adaptive optics on both Keck telescopes to correct individual wavefronts and employed active fringe tracking across all modes for path-length control. This included the implementation of co-phasing to enable long coherent integration times. Additionally, KI introduced high-sensitivity fringe-visibility measurements in the H (1.6 µm), K (2.2 µm), and L (3.8 µm) bands, as well as nulling measurements in the N band (10 µm), facilitating research across a wide array of scientific topics[16].

1.5.2 LBTI

The Large Binocular Telescope Interferometer, shown in Figure 1.4, has a unique design, comprising of the dual apertures on a common elevation-azimuth mount, which enables a broad use of observing modes. It is a high spatial resolution instrument designed for coherent imaging and nulling interferometry operating in thermal infrared and uses a baseline of 14.4 m[49].

The LBTI is characterised by a modular configuration, as shown in Figure 1.5, featuring

a universal beam combiner (UBC) that can direct light to three separate camera ports. Funded by NASA, the project aims to study nearby stars that could be prime targets for future direct imaging searches for Earth-like planets. The LBTI is specifically designed for the sensitive detection of exozodiacal dust and the imaging of giant planets. The LBTI's architecture is ideated to support multiple science cameras by utilizing adaptive optics and beam combination capabilities[50].

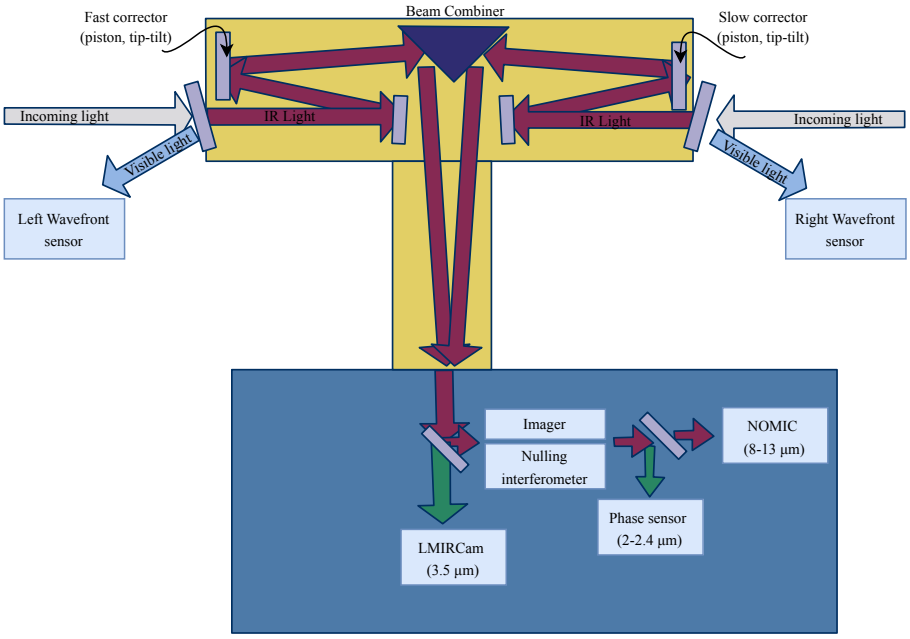

Figure 1.5: Layout of the LBTI and optical path through the beam combiner and the NIC cryostat. Starlight is first reflected by the LBT's primary, secondary, and tertiary mirrors before entering the diagram from the top right and top left. Visible light is reflected off the entrance window for adaptive optics, while infrared light passes into the LBTI, where all subsequent optics operate at cryogenic temperatures. The beam combiner uses steerable mirrors to direct the light and adjust pathlengths for interferometry. Adapted from Defrère et al.[24].

LBTI achieves nulling interferometry by directing each telescope beam through opposite sides of a single-pass, 50% transmissive beam splitter at near-normal incidence. To ensure an achromatic null, a slight difference in the thickness of the zinc selenide substrates (used for both the beam splitter and compensating window) is introduced between the two beams. This is possible since the wavebands considered are restricted, namely N-band ($8-14\,\mu m$ — NOMIC camera) and L/M-bands ($3-5\,\mu m$ — LMIRCAM camera). Precise beam alignment is achieved through adjustments using two three-axis Piezo-electric transducers (PZT) tip-tilt-piston platforms. In particular the interferometer is adjusted for nulling by tuning the phase sensor setpoint, while measuring the flux at 11 μm[49].

1.5.3 VLTI

The Very Large Telescope Interferometer is composed of four 8.2 m Unit Telescopes (UT), set in a fixed location, and four 1.8 m Auxiliary Telescopes (AT) which can be relocated on more than 10 different stations, as displayed in Figure 1.6. The AT stations are connected by rail tracks on which the ATs can be relocated. After passing through a complex system of mirrors and having their light paths equalized by the delay line system, recombination is carried out by PIONIER and GRAVITY instruments in the near-infrared and by MATISSE instrument in the mid-infrared spectrum. It is unique in offering the possibility to combine a maximum baseline of 130 m, and to combine a maximum of four

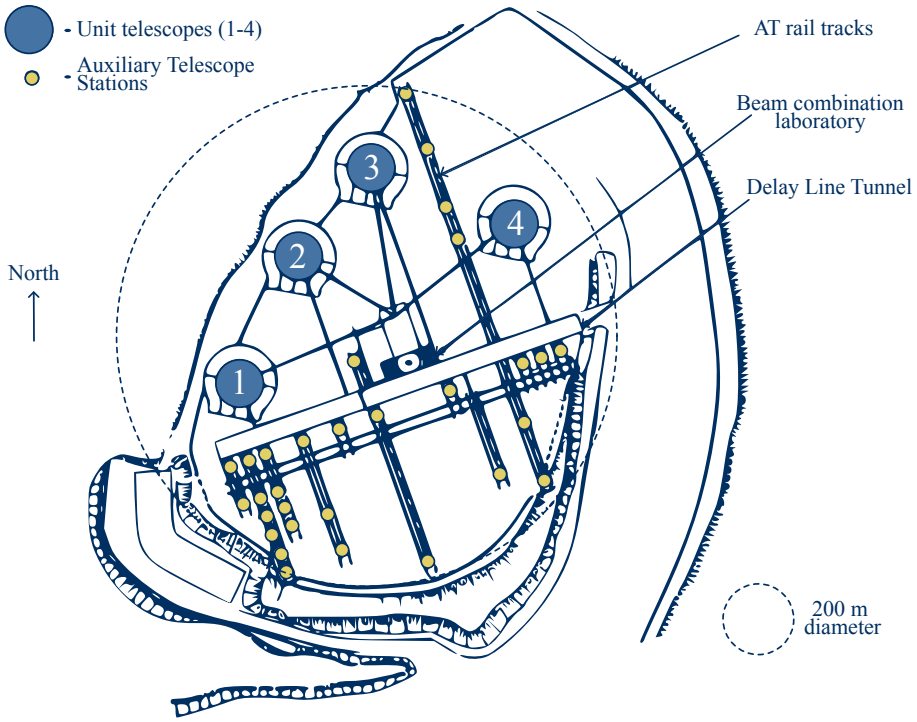

Figure 1.6: Layout of the VLTI. The four 8-meter Unit Telescopes (UTs) and the 30 stations for the 1.8-meter Auxiliary Telescopes (ATs) are represented. The AT stations are linked by rail tracks, enabling the relocation of the ATs. Also depicted are the Delay Line tunnel and the beam combination laboratory. The Delay Line tunnel accommodates eight Delay Lines, allowing the operation of four ATs and providing a total of 28 baselines per exposure. The maximum baseline length between two ATs is 200 meters (represented by a 200m-diameter circle), while the longest baseline between two UTs is 130 meters. Adapted from Glindemann et al., 2003[43].

1.8 m ATs. The ATs can be moved to the different stations with a maximum baseline of 200 m[43].

Thanks to its unique capabilities, the VLTI has become a valuable tool for studying a wide range of astronomical objects, including young pre-main sequence stars and their proto-planetary disks, mass-losing post-main sequence stars, binary systems and their orbits, solar system asteroids, and extragalactic objects such as active galactic nuclei[32].

1.5.4 Comparison and future ideas

Figure 1.7 shows the footprints of ground-based modern optical interferometers. In particular, the telescopes KI, LBTI, CHARA and VLTI-UT's are fixed, whereas the NPOI and the VLTI-AT's telescopes are mobile and can be repositioned. The only major facility under construction today is the Magdalena Ridge Optical Interferometer, which aims to combining up to ten 1.4 m telescopes over 350 m baselines[29].

Interferometry has made significant advancements in recent years, yet current systems remain far from their fundamental performance limits. Several factors contribute to this shortfall, with some of the most significant being the limitations in adaptive optics (AO) performance, optical throughput inefficiencies, metrology laser background noise, detector noise, and structural vibrations. These challenges hinder the full exploitation of interferometers' potential, restricting sensitivity and observational precision[26].

However, ongoing upgrades and technological innovations aim to address these limitations. A major advancement is the GRAVITY+ upgrade, which incorporates laser guide star (LGS) adaptive optics and a wide-field dual-beam capability[29]. This enhancement is

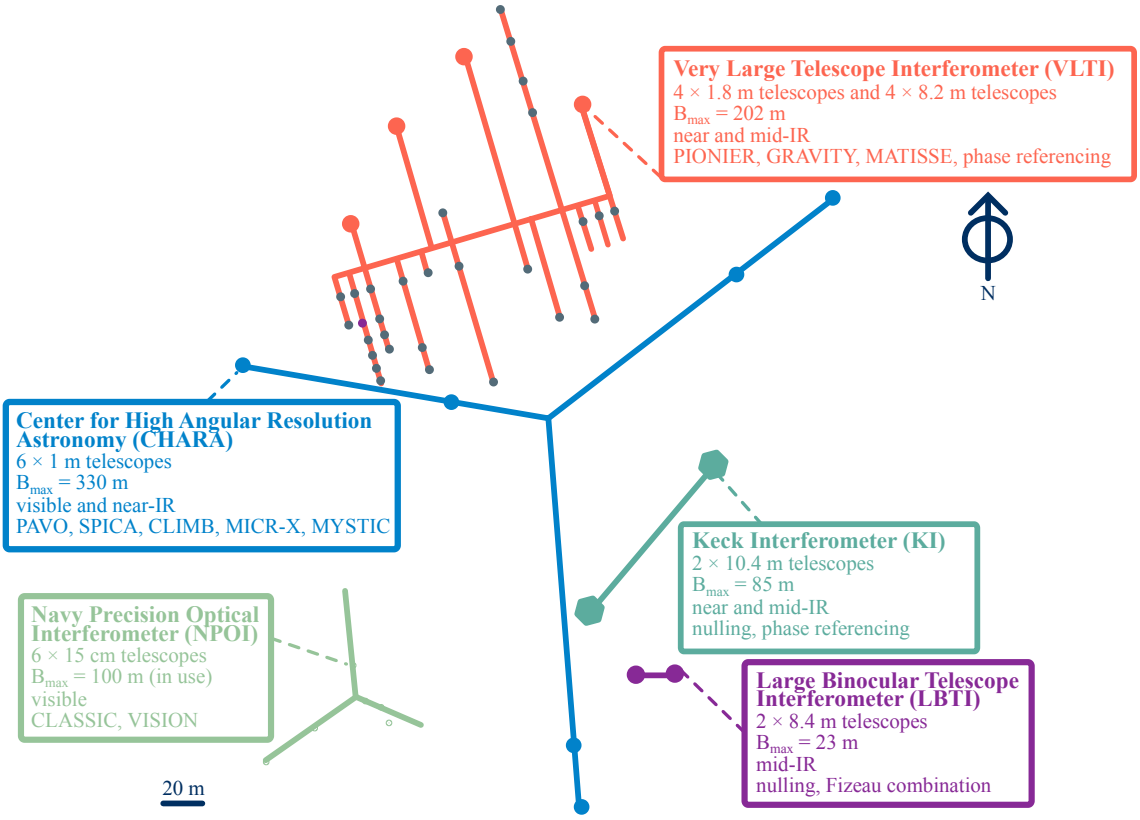

Figure 1.7: Footprints of modern optical interferometers, with telescopes and baselines to scale. The telescopes for KI (teal), LBTI (purple), CHARA (blue), and VLTI-UTs (red large circles) are fixed, whereas the NPOI (green) and VLTI-ATs (red small circles) telescopes are mobile and can be repositioned. Adapted from Eisenhauer et al., 2023[29].

expected to dramatically improve sky coverage, enabling observations of a far greater number of targets than before. Additionally, existing interferometric facilities continue to evolve by broadening their accessible wavelength ranges and serving as platforms for testing emerging technologies, such as nulling interferometry.

While upcoming extremely large telescopes in the 30–40 meter class will vastly outperform current facilities in sensitivity, they will not surpass interferometers in angular resolution. The Very Large Telescope Interferometer (VLTI) and the Center for High Angular Resolution Astronomy (CHARA) will retain their unique advantage in this domain, making them indispensable tools for high-resolution astrophysical studies even in the era of ELTs[29].

An important project involving the VLTI is Asgard/NOTT, a L-band nuller which was officially presented at the VLT 2030 conference in June 2019 by ESO's Scientific Technical Committee (STC) for the visitor focus of the VLTI. Asgard/NOTT follows a series of nulling interferometers that have been deployed over the past three decades on state-of-the-art facilities, both across single telescopes and as separate aperture interferometers[26]. The key innovation is the use of a photonic beam combiner, which has only recently achieved the necessary theoretical raw contrast of 10^{-3} within this spectral range. It enables a more stable and more compact design as well as an easier alignment procedure than with free-space optics[39]. Nulling interferometry observations of exoplanets also demand precise balancing of the four VLTI pupils in terms of intensity, phase, and polarization. The design of the warm optics and the injection system is guided by the need to optimize beam injection into the combiner while meeting the stringent requirements of nulling interferometry. The optical design of the instrument also includes the cold optics located

inside a cryostat and cooled at 90 K. They comprise the injection system, the photonic chip, the spectrograph, and the detector[39]. Asgard/NOTT has the potential to carry out several exoplanet programmes to study young Jupiter-like exoplanets at the most relevant angular separations, and better understand how planets form and evolve[26].

1.6 Bracewell first concept and improvements

Interferometric methods for direct detection of extrasolar planets, which try to overcome the two main difficulties (the high contrast and the high angular resolution), are derived from the initial concept of Bracewell (1978) of a rotating two-telescope interferometer. Since then there has been a substantial body of work in which a variety of array configurations of interferometers has been proposed for exoplanet detection[19]. Figure 1.8 shows a scheme of the evolution of the preferred nulling architectures until 2007.

1.6.1 Bracewell principle

The space-based interferometer proposed by Bracewell is characterised by two apertures and light recombination in phase opposition. This setup creates a dark fringe along the line of sight, significantly reducing stellar emissions. For an off-axis source, light transmission depends on the baseline length and wavelength, which together determine the interferometer's transmission map. In order to retrieve the planet from all signals and distinguish it from the background, Bracewell proposed to rotate the interferometer around its line-of-sight. As the planet moves, it crosses both bright and dark fringes, causing its flux to be modulated, while the uniformly distributed background remains unaffected[21].

Figure 1.9 shows the monochromatic transmission map, namely the intensity response of a typical nulling Bracewell interferometer. Starting from the the computation of the expression of the electrical field produced by a point source of unit flux, it is possible retrieve the interference pattern and define which parts of the field-of-view are transmitted by constructive interference, and which are blocked by destructive interference[25]. The star is positioned at the central dark fringe, while potential planets can appear anywhere in the sky.

By rotating the interferometer around the line of sight, planets pass through different fringes, leading to variations in transmission as shown. To extract the planet's modulated signal, a cross-correlation transform is applied between the expected signals and the actual modulation observed. However, this modulation has a drawback—on average, the detected planetary signal is reduced by 50% in a Bracewell interferometer[21].

The main disadvantage linked to the single Bracewell configuration is that the response on the on the sky is symmetric on either side of the star, therefore, the planet position angle has 180° ambiguity meaning that is difficult to separate the planet signal from other sources of emission and it is not possible to perform phase chopping[25]. As a result, improved configurations with more than two collectors have been proposed to overcome these limitations, as the Angel Cross configuration and the Kernel interferometer.

1.6.2 Angel Cross and asymmetric configuration

In 1990 Angel proposed a configuration of four telescopes in a square shape, combined with multiple beam-splitter for transmission varying as $\sin^4\theta$ instead of $\sin^2\theta$ and named Angel Cross. It is indeed a double Bracewell interferometer, where the two outputs are recombined with no additional phase shift. This configuration allows to overcome the strict constraint on the pointing accuracy[2].

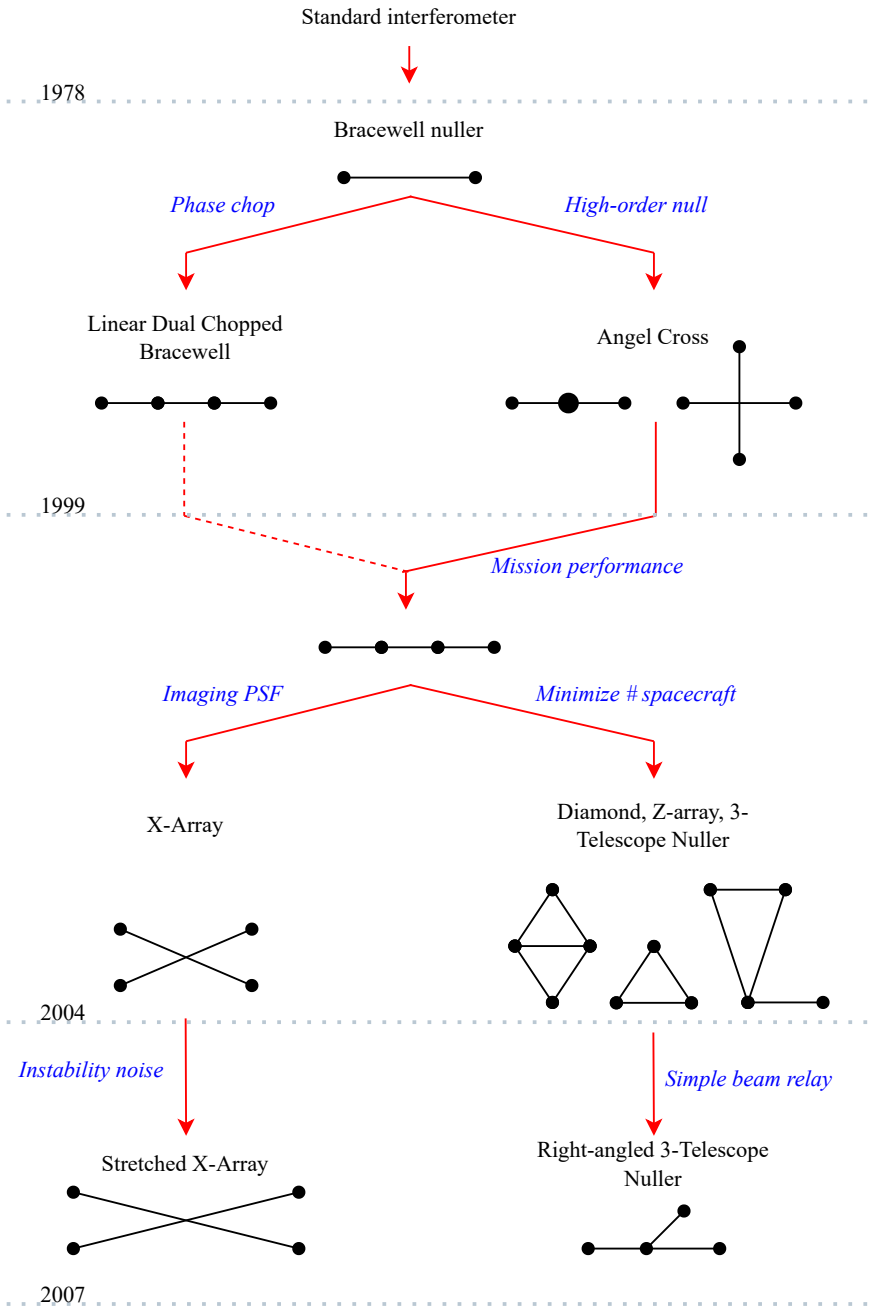

Figure 1.8: Schematic representation of the preferred nulling architecture up to 2007. Readapted from TN2-ESA nulling interferometry[17].

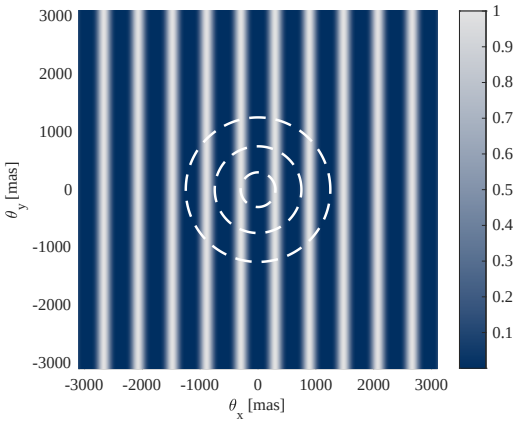

Figure 1.9: Transmission map of a typical Bracewell interferometer. As the interferometer rotates, hypothetical planets (represented by the white line) cross bright and dark fringes.

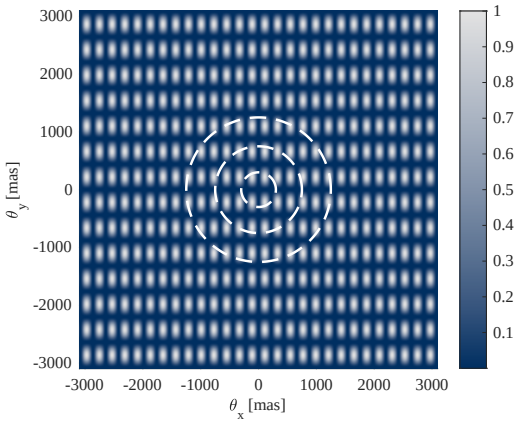

Figure 1.10: Transmission map of a generic X-array interferometer. With respect to the Bracewell interferometer, which produces a mono-dimensional transmission map, if the apertures are on a plane, they will produce a bidimensional transmission map.

Furthermore, in order to detect Earth-like planets despite the fact that the bright exozodiacal light is modulated at the same frequency as the planetary signal, the solution is to design an interferometer with an asymmetric transmission map, so that every planetary system can be treated the same way, independently of their inclination. In 1996, Léger et al.[70] proposed an asymmetric array, made up of five telescopes, regularly located on a circle. Subsequently, Mennesson and Mariotti[77] proposed an improvement of the circular array, based on an elliptical configuration. The elliptical configuration produces an irregular transmission map, allowing precise localization of the planet. Additionally, when the array rotates around its centre, azimuthal holes are eliminated, ensuring that all angular separations maintain a strong modulation amplitude. As a result, a variable baseline is no longer necessary.

In general, transmission map will change depending on the number and the position of the apertures, as shown in Figure 1.10, which represents the transmission map of a generic X-array interferometer. While the Bracewell interferometer produces a mono-dimensional map, considering in-line apertures, in this case a bi-dimensional transmission map is observable.

However, this setup introduces a new challenge: because the telescopes are positioned at varying distances from the central recombining hub, continuously adjustable long delay lines are required to equalize the optical path lengths of the incoming beams[3].

1.6.3 The importance of phase chopping

In order to modulate the desired signal in presence of varying backgrounds and detector shifts, the phase chopping technique is necessary. If the desired signal can be intentionally modulated (chopped) at a frequency that is unlikely to be mimicked by other signals, the chopped planetary signal will average to a stable value, while drifts will tend to cancel out. In practice, the chopping frequency is determined by the detector's minimum readout time, ensuring that readout noise remains significantly lower than the detected photon flux. As a result, typical chopping frequencies range between 0.1 and 0.01 Hz. This approach also significantly reduces constraints on the interferometer's rotation frequency. In particular, regarding nulling interferometry, the principle is to use two or more subsets of nulling interferometers, and combine them is such a way that the point-like planetary signal is

strongly modulated whereas the extended background sources are not[3].

1.6.4 Kernel improved interferometer

To address the limitation related to the extreme sensitivity of the instrumental response to tiny optical path differences between apertures, the Kernel-nuller architecture has been proposed. In particular, the idea is to alleviate this effect with an integrated combiner design that allows the generation of observables that are inherently resistant to residual optical path differences[61].

The architecture and methodology of the Kernel-nulling interferometry concept enables simultaneous advantages: leveraging the high-contrast enhancement of the nuller while preserving the ability to detect the otherwise degenerate effects of varying observing conditions. This allows for the construction of observables that remain resilient to such spurious influences. Much like closure-phase, the kernel-nulled outputs also resolve the symmetry degeneracy inherent in a classical nuller's output, with the signs of different kernels indicating the location of asymmetric structures within the field of view[73].

1.7 Space-based Interferometers

For the reasons presented in Section 1.4, in past years there has been a strong interest in developing a space-based interferometry mission. Absorption- and scintillation-free missions would fully unlock the potential of this technology, but the novelty of the technology on one hand and the high technical difficulties and costs on the other have prevented the practical realisation of a real mission.

That being said, over the years, there have been many proposals from both the two largest space agencies, ESA and NASA, which followed two different approaches: either simplifying the design and reducing the number of involved spacecraft for the former or increasing the imaging properties of the system for the latter[17].

1.7.1 Darwin

Darwin was a proposed four-aperture space-based interferometer formed by a constellation of five satellites, with the main objective of studying exoplanets and advancing specific topics of ESA's Cosmic Vision project[70], such as planet formation and habitability.

Its design was based on the need for high angular resolution, equivalent to 100 m class telescopes in the mid-infrared range, to target habitable zones between 10 and 100 mas[70]. However, the design underwent multiple revisions over time: for example, until 2004, a six-free-flying 1.5 m telescope configuration arranged in a hexagonal pattern, launched by a single Ariane 5 vehicle, was considered[36],[18], as well as a three-telescope nuller configuration[18]. The final array configuration, adopted around the possible merging with TPF-I, called the "Emma X-Array" after Charles Darwin's wife, utilised four collectors in a planar configuration, followed by a collector that was out of plane, increasing sky coverage and reducing design complexity[70].

Clearly, the main drawback of having such a large baseline is linked to the necessity of formation flying, which significantly increases the likelihood of failures and risks: if any of the spacecraft, for any reason, is unable to sustain its role, the mission is lost. In addition to this fundamental aspect, the precision and stability required for formation flying are considered a major challenge[70],[36],[37].

A minimum null depth requirement of 10^{-5} was established, enabling a search strategy targeting more than 200 stars (with a focus on F, G, K, and M-type stars), leading to the

characterisation of 25 to 50 exoplanetary atmospheres and biosignatures over a five-year baseline mission[70],[36].

In conclusion, Darwin was the subject of many development papers[3], which led to a deep understanding of its behaviour and were extensively used in future missions like LISA. However, due to technical and budgetary constraints, as well as a shift in the strategy for exoplanet searches and immaturity of the technologies[18], the mission was indefinitely shelved in 2007[30].

Nowadays, if the mission were to be recovered, it would indicate as possible precursors, inheriting their knowledges and developments, missions like COROT (CNES), Kepler (NASA), PRISMA (SSC), PROBA-3 (ESA), and Pegase (CNES), which all introduced some progress in the research[70].

1.7.2 Terrestrial Planet Finder Interferometer

NASA's development of a mission for terrestrial planet finding followed a similarly long development phase to Darwin, where both a coronagraph (the TPF-C version) and an interferometer (TPF-I version) were considered in the initial phases. The former had advantages in requiring smaller apertures and no cooling in the visible domain[102].

Similarly to the European project, TPF-I involved (at least in one version, since a structurally connected interferometer with a truss structure was also considered, but this choice led to lower achievable baselines[102]) formation flying with spacecraft separated by up to 100 m (in a proposed X-Array[62]) for the survey of 150 stars in the F, G, and K classes and the characterisation of detected exoplanets in the mid-infrared region[102].

The four subsystems that required intensive testing were summarised by the COST acronym: controls, optical, structural, and thermal. Each of them proved particularly complex, with tight control and strong thermal modelling requirements (below 40 K for the optical surfaces[104]). The flight formation interferometer was conceptualised with over 100 optical elements and primary mirrors exceeding 4 metres in diameter[104].

Starting in 2007, a common architecture was defined in collaboration with ESA, significantly simplifying the design and increasing the coverage in space[62] by exploiting the Emma X-Array. During the following decade, plans were proposed to increase the TRLs of both formation flying and nulling interferometry to acceptable thresholds, with the aim of initiating a possible Phase A around 2020[62].

This project, however, was indefinitely deferred, likely for reasons similar to those that led to the shelving of Darwin, although other investments in space interferometry have continued[62]. Again, precursors missions to a new, possible return, were the COROT and Kepler missions[88].

1.7.3 Large Interferometer For Exoplanets

The LIFE mission, proposed by a Swiss team at ETH Zürich, is a more recent evolution of the previously discussed missions, dating from 2017[91]. It is based on the same principle as the Emma X-Array in a formation flying configuration[42].

Ongoing research is assessing the feasibility of the mission[91],[22], evaluating its feasibility and signal sensitivity, and proposing the mission for ESA's Voyage 2050 programme[42].

Similarly to Darwin and TPF-I, LIFE aims to characterise around 30 rocky planets with an extended baseline of approximately 600 m for imaging in a Double Bracewell configuration[42]. Challenges have again arisen regarding formation flying, which will be addressed by ESA's PROBA-3 mission (launched in December 2024) and NASA's STARLING mis-

Mission	**Bandwidth** [µm]	**Mission duration** [yr]	**Baseline** [m]	**Diameter** [m]
Darwin[70]	6-20	5	500	2
TPF-I[62]	6-18	5	100	4
LIFE[42]	6-16	5	600	4

Table 1.2: Comparison of the bandwidth, mission duration, maximum baseline, and aperture diameter of the three presented space interferometers.

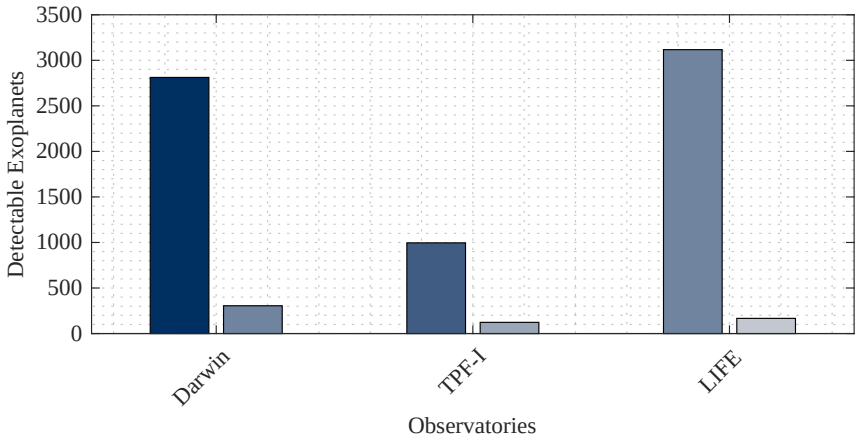

Figure 1.11: Comparison of the ideal (maximum) yield of exoplanets based (left series) and the yield of exoplanets with a cut-off around 10^{-7} contrast ratio (right series), based on the data from Table 1.2 and the exoplanet catalogue generated by P-Pop[52].

sion (launched in 2023), as well as interferometric fringe tracking and nulling performance at cryogenic temperatures[42].

1.7.4 Comparison

Table 1.2 presents an overview of key parameters for the considered missions (at least in one of their iterations). The similarities in the presented values illustrate how all of them converge towards an optimised design.

Similarly, Figure 1.11 displays the ideal number of detectable exoplanets based on the simplified computation of the inner and outer working angles for the three presented interferometers. Although the numbers are only indicative due to the simplified analysis, this graph clearly shows that the dominant parameter in the analysis, as expected and as declared, is the baseline: the outer working angle, which in turn is affected by the diameter, has little consequence on the design (provided that it is large enough), and even if the TPF-I had double the diameter of Darwin (at least during one of the iterations), its yield is far smaller than the other two proposed missions.

It is clear, then, what the appeal of a formation flying interferometer is: even with the use of deployable surfaces, results like those reported in Table 1.2 will not be achievable, significantly reducing the number of detectable exoplanets.

On the same figure, however, if the sensitivity cut-off is applied (that being the fact that some contrast ratios are too faint for their detections), the situation significantly changes and as it can be seen, the three observatories becomes effectively comparable. That being said, quality is usually preferred over quantity, and given the fact that prolonged observation times are needed to fully characterise the exoplanets[70],[88], during the baseline mission duration, only a limited number of targets will be studied.

1.8 Conclusions

Nulling interferometry represents one of the most promising techniques for the direct detection and characterization of exoplanets. This work has provided a comprehensive overview of its principles, advantages, and applications, examining both ground-based and space-based implementations. While ground-based interferometers such as LBTI and VLTI have demonstrated the capabilities of this technique, their effectiveness, especially in desired mid-infrared region, is constrained by atmospheric interference and limited wavelength coverage.

Space-based interferometry can therefore be the definitive solution: originally introduced by Bracewell, it has evolved in multiple configurations, like the Angel Cross and Kernel-nulling interferometers, which mitigate phase and alignment challenges. Despite proposals from both ESA and NASA, technological and budgetary constraints have so far prevented their realization. However, ongoing developments suggest that the feasibility of a dedicated space-based nulling interferometer is steadily increasing.

Through our analysis, we have highlighted the challenges that must be addressed: achieving sufficient null depth, improving formation-flying precision, and developing high-sensitivity detectors that can operate in extreme space environments. The maturation of these technologies, supported by precursor missions like PROBA-3 and STARLING, will likely enable the next generation of exoplanet studies.

Ultimately, nulling interferometry remains at the forefront of the quest to answer one of the most profound scientific questions: are we alone in the universe? As advancements continue, this technique holds the potential to revolutionise our understanding of planetary systems and the search for biosignatures beyond our solar system.

2 Theoretical aspects and optical design considerations

Before introducing a mathematical model to describe the behaviour of nulling interferometry, this chapter aims to introduce the concepts and phenomena associated with its behaviour, starting from a physical perspective and eventually moving towards a broader view of the key elements that must be considered when evaluating the validity of the instrument.

Section 2.1 provides a brief summary of the physical processes involved in nulling interferometry, while Section 2.2 explains how these principles are exploited in imaging and nulling processes within a general interferometer. On the other hand, Section 2.3 provides a general outline of the main elements that constitute the instrument, detailing the different stages that the light beams undergo before reaching the detector.

A brief discussion on the space environment is then addressed in Section 2.4, including the classification of the main disturbances that can arise during the research and detection phases. Finally, Section 2.5 briefly presents the tasks that follow detection, highlighting the subsequent steps.

2.1 The wave behaviour of light

The duality of the nature of light, being a quantised particle and a wave, has led to the development of different theories and applications. The classical concept of an electromagnetic wave, being itself a continuous entity of two fields, the electric and the magnetic ones, modulated in time and space, has clashed with the developments of quantum mechanics. Yet, the large scale regime that is generally considered allows for the use of such a simpler description[47].

In the most general case, the behaviour of a generic electromagnetic wave is fully described by Maxwell's four laws, which analyse the different interconnections between the electric and magnetic fields. These equations can be manipulated in order to obtain the wave equations associated with the two vectors[47] [1],

$$\nabla^2\mathbf{E} = \epsilon_0\mu_0\frac{\partial^2\mathbf{E}}{\partial t^2} \quad \wedge \quad \nabla^2\mathbf{B} = \epsilon_0\mu_0\frac{\partial^2\mathbf{B}}{\partial t^2}, \tag{2.1}$$

where $\mathbf{E}$ and $\mathbf{B}$ are, respectively, the electric and magnetic fields, ϵ_0 and μ_0 are, respectively, the electric permittivity and the magnetic permeability in a vacuum and t is the time variable. The representation of the waves can be further simplified by assuming linearly polarised waves, i.e., by fixing the direction of the electric field. In this case, then, it can

[1] This document adopts the general convention of showing vectorial/matrix elements in bold.

be shown that waves present a harmonic behaviour[47]:

$$E_y(x,t) = E_{0y}\cos\left[\omega\left(t - \frac{x}{c}\right) + \epsilon\right] \tag{2.2}$$

$$B_z(x,t) = \frac{E_{0y}}{c}\cos\left[\omega\left(t - \frac{x}{c}\right) + \epsilon\right]. \tag{2.3}$$

Given the fixed direction, the vectorial expression then reduces to a scalar description of the two orthogonal fields, where ω is the angular temporal frequency.

2.2 Diffraction of waves

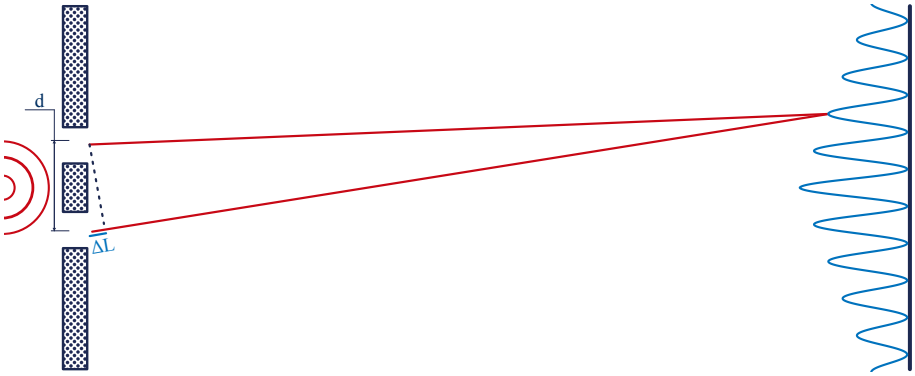

Figure 2.1: Principle of interference: the result of the interference is a function of the optical path difference (in light blue, on the left) between the two light beams, producing a sinusoidal signal that can lead to constructive or destructive interference. In this case, the diagram illustrates a central constructive interference (Young's experiment).

Interferometry is a broad field of optics that exploits the principle of interference between two light beams, which is a direct consequence of the superposition principle. In order to achieve light interference, several requirements must be met[47]:

- The two (or more) interfering beams must maintain a constant phase relationship, meaning they must be coherent. There are multiple ways to define coherence length, including methods based on visibility, but one of the most commonly used definitions is based on the considered bandwidth[3],[72],

  $$L_c = \frac{\lambda^2}{n\Delta\lambda}, \tag{2.4}$$

  where λ is the wavelength, $\Delta\lambda$ is the bandwidth, and n is the refractive index of the medium (in space, $n = 1$).
- The two beams must be separable to ensure that they experience different optical path lengths. In general, the output of the interference is directly dependent on the optical path difference, which is the length difference between the travelled paths of the light beams. In the case of an astronomical interferometer, where increasing the baseline is desirable, light entering the system is already separated by the multiple apertures used.
- Recombination is performed on a beam splitter, leading to interference of the light. Two detectors (since the beam is split in two parts), either CCDs or photodetectors, must be used to collect the output of the operation.

In addition to optical requirements, several other factors related to system stability, thermal emissivity of mirrors and cooling (to minimise electronic noise) must be considered to obtain a valid result. If these conditions are met, then mathematically, given two coherent light waves, the intensity of the resulting signal is given by[47]

$$I = I_1 + I_2 + 2\sqrt{I_1 I_2}\cos\left(\frac{2\pi\,\Delta L}{\lambda}\right), \tag{2.5}$$

where ΔL represents the optical path difference at the evaluation position. As illustrated in Figure 2.1, the resulting signal follows a cosine function that periodically enhances or cancels the signal. Constructive interference occurs when the signal is maximised, whereas destructive interference occurs when the signal is minimised (potentially reaching zero).

It is then evident, in relation to the discussion in Chapter 1, that the main design principle is to control the resulting fringes so that destructive interference occurs at the location of the star—an undesired light source—while constructive interference occurs at a desired point. Ideally, this would allow the fainter source (e.g., an exoplanet) to become visible. This is physically achievable due to the intrinsic optical path difference between the light signals from the star, typically aligned with the telescope's optical axis for simplicity, and those from the exoplanet, which has a certain angular separation from its host.

Unlike Figure 2.1, where the central signal is enhanced, a nulling interferometer relies on a different type of phase control, achieved by introducing specific delay lines. According to Equation 2.5, interference follows these principles:

- **Constructive interference** occurs when the phase difference is an even multiple of π:

$$I = \max I \qquad \forall\, n \text{ such that } \Delta\varphi = 2n\,\pi. \tag{2.6}$$

- **Destructive interference** occurs when the phase difference is an odd multiple of π:

$$I = \min I \qquad \forall\, n \text{ such that } \Delta\varphi = (2n+1)\,\pi. \tag{2.7}$$

In optical interferometry, the wavefronts from different sources—such as the apertures of an interferometer—combine according to their relative phases. The resulting intensity pattern depends on the coherence and phase difference between the waves, which, in turn, is governed by the optical path difference (OPD) between the beams.

For a two-element interferometer, the contrast of the interference pattern, known as visibility, is a measure of the coherence between the beams and is proportional to the path difference. It is expressed as

$$V(\vartheta) \propto \cos\frac{\pi B \sin\vartheta}{\lambda}, \tag{2.8}$$

where B is the baseline length, λ is the wavelength, and ϑ is the angle of incidence of the incoming wave. This function describes how the visibility varies as a function of the spatial phase differences introduced by the interferometric setup.

2.3 Key Optical Components of an Interferometer

At first glance, a nulling interferometer can be seen as a combination of multiple telescopes arranged in a specific configuration. Figure 2.2 presents a block diagram of a possible four-aperture nulling interferometer. As shown, each aperture is followed by the same sequence of optical elements, and in the final stage, all fibre-fed signals converge at the beam combiner. The beam combiner contains additional optical components that produce the desired output, as discussed in Chapter 3.

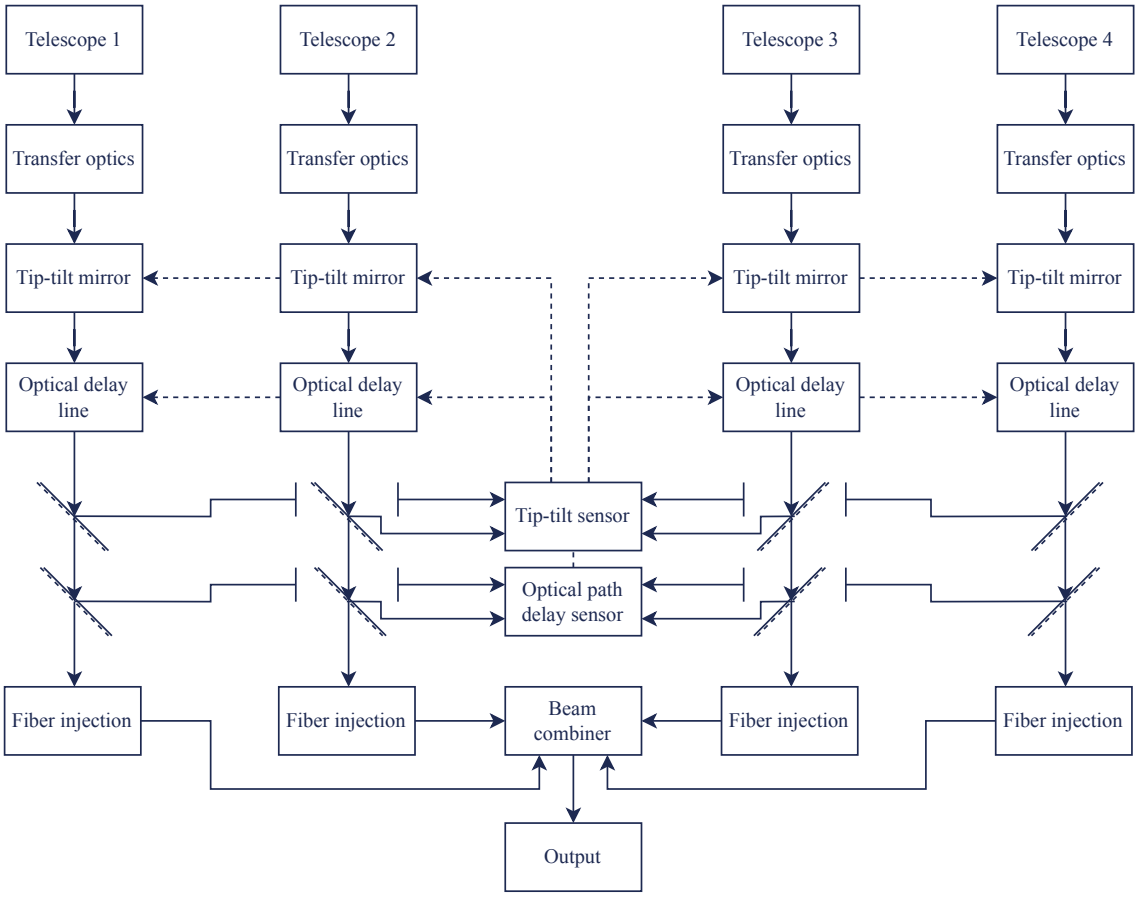

Figure 2.2: Block diagram of a four-telescope interferometer optical layout, adapted from Dandumont[20],[25].

2.3.1 Telescopes and transfer optics

Multiple telescope configurations have been designed to accomplish different tasks, with the ultimate goal of gathering light without introducing excessive aberrations within the system. Designs include refractive or reflective telescopes, as well as specific configurations like Cassegrain or specifically designed ones like the siderostat-confocal hybrid optic and direct confocal setup, both proposed by Viseur[72], in their master thesis upon which this work develops.

In general, it is difficult to find a universally valid design, since a trade-off is always necessary: compactness, simplicity, and error reductions are always opposing features that may limit the achievable possibilities. For instance, from a modelling point of view, the most important parameter correlated to the single telescope itself is relative to aperture diameter, which defines the outer working angle and the minimum detectable intensity[2]. These parameters, which will be analysed later, essentially provide a minimum aperture that is needed to ensure a wide enough search field and detection capability.

However, especially for space systems, another limitation arises from design compactness: besides the costs, the launcher fairings pose a hard limitation on the possible designs. This is a strong argument in support of formation-flying systems, where the situation significantly improves given the possibility to schedule different launches. Yet, given the considerations addressed in Chapter 1, a single-spacecraft interferometer is nowadays preferred.

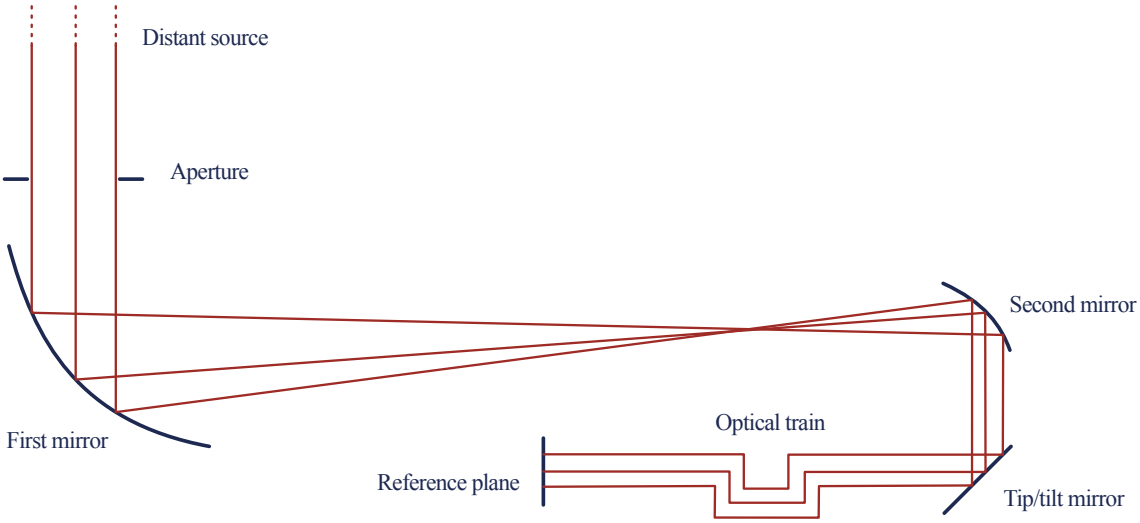

Figure 2.3: Example of possible telescope configuration: schematic representation of the elements that are found in a direct confocal setup, adapted and simplified from Viseur[72].

2.3.2 Control systems and sensors

As any other opto-mechanical system, the interferometer is subject to multiple undesired effects that must be kept under control in order to reach a satisfactory result. Several available techniques can and must be implemented, including deformable mirrors and the use of a tip-tilt mirror.

A tip-tilt mirror is a type of adjustable mirror that can be tilted around two axes (tip and tilt) to control the direction of the reflected light beam. This is primarily used to correct misalignments and stabilise the optical path by compensating for small deviations in the incoming light and is therefore a fundamental part of the system[21]. It can be thought of as part of an adaptive optics setup (although this term is usually used in reference to ground-based telescope corrections for atmospheric fluctuations)[21].

As recalled in Section 2.2, interference is mainly a matter of phase influence; therefore, strict phase control with a certain degree of stability is needed, and maintaining precise relations between the different waves is a critical aspect of the design. Thermal fluctuations and vibrations, which are natural occurrences in any mechanical element, make this component of the design necessary.

In practice, the tip-tilt mirror acts through the presence of micro-precision actuators, which are either piezoelectric (for smaller but high-precision adjustments) or servomotors (for larger adjustments) in a closed-loop system with the optical path delay sensor[94]. This setup adjusts each branch of the interferometer to grant the correct amount of deformation to the mirrors.

2.3.3 Optical delay line and fibre injection

The final part of each branch includes the optical delay line, an optical system that introduces a controlled delay to the light travelling through it, ensuring that the collected light arrives at the beam combiner in phase, that is, with the correct delay.

It can be a mechanical delay line, making use of mirrors and phase retarders to physically change the path of the light, which can provide higher precision. Alternatively, although very rare, it can be a fibre optical delay line, which uses longer or shorter fibres to introduce delay, offering higher sensitivity but being dependent on the optical properties of the used fibres[21].

Either after (in the former case of a mechanical delay line) or before (in the case of an optical fibre delay line), a fibre injection system is usually present. This system injects the collected light into the fibre, facilitating its transport. The ensemble of the optical delay line and the fibre injection system constitutes the optical train, propagating the signal to the combination location[2],[96].

2.3.4 Beam combiner and detector

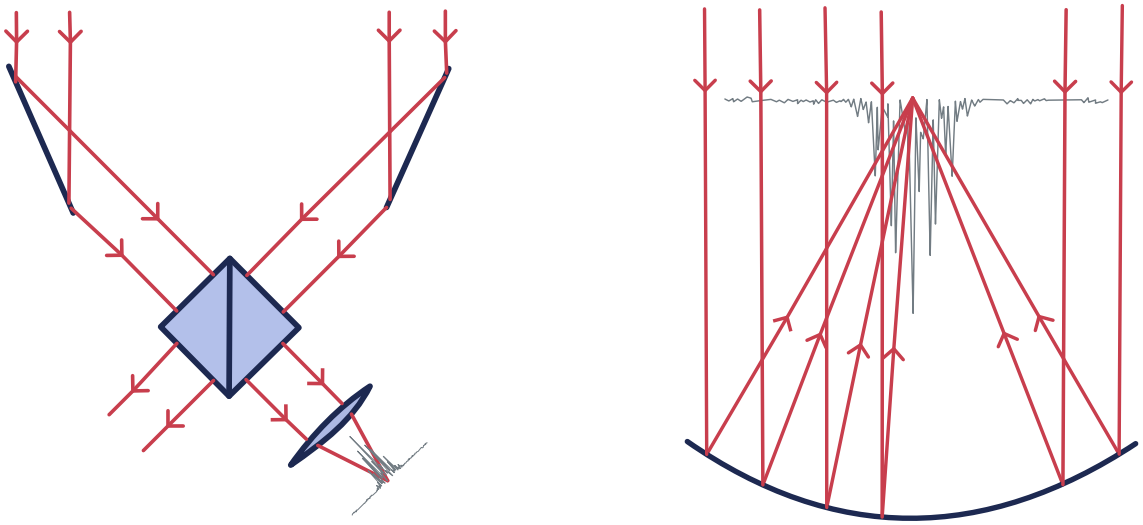

(a) Coaxial **(b)** Multiaxial

Figure 2.4: Types of beam combiners, simplified from Schöller et al., 2000[94].

To maintain coherence, two approaches to beam combination are usually employed: coaxial or multiaxial combinations[72]. Other methods, such as pupil densification, also exist[2],[6].

In a coaxial combination, light beams are combined along a single optical axis by directing light from each telescope into a common path where they can interfere, for example, by using a beam splitter at the pupil plane. This is the most commonly used technique for two-aperture interferometers. While it can be expanded to multiple apertures, maintaining alignment and coherence becomes more challenging[94],[95].

A multiaxial beam combiner allows for the combination of light beams at different axes, providing more flexibility and accommodating more apertures by using a single focus and allowing combination at the image plane[94], generating an image of the interference pattern like shown in Figure 2.1.

Regardless of where the combination occurs, a detector must be employed, depending on the application. As detailed in Chapter 1, for exoplanet detection, the most important information is extracted from the spectra of analysed bodies; therefore, a spectrometer is among the most likely employed instruments. Given the low coherence length, low-noise, high read-out detectors are needed[2].

2.3.5 Array Configurations

Apart from the design of the single branch, another fundamental feature in an interferometer that ultimately defines its resolution limits and therefore its applicability to the proposed mission goals is the array design and baseline definition.

From an optical point of view, there are no strict limitations on the possible employed arrays. On the ground, several shapes have been considered, including, for example, a

Y-shaped array. Irregular shapes can also be employed, making the interference acquisition arithmetically more challenging yet feasible. Out-of-plane arrays are also technically possible; however, they introduce undesirable thermal effects[65],[69], thereby limiting their applicability.

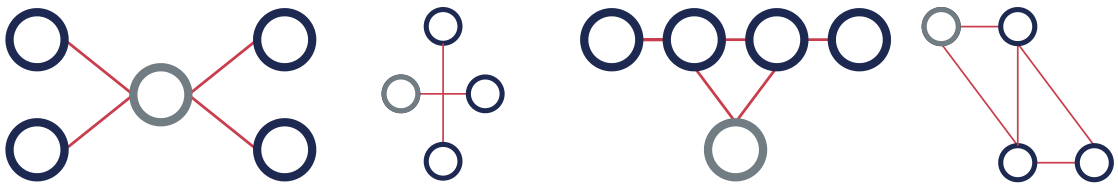

(a) X Array **(b)** Diamond **(c)** Linear **(d)** Z Array

Figure 2.5: Some examples of four-aperture arrays that have been theorised and studied by Lay, 2005[65]. The lighter circumpherence represents the beam combiner.

Besides the two-element arrays, which are usually called Bracewell's arrays after the first theoretical analysis, several designs have arisen from the employment of multiple apertures in a plane configuration, including, for example, those reported in Figure 2.5. Bracewell's design, despite its simplicity, lacks the ability to produce a non-symmetric response, leading to high ambiguity in the planet position and making it impossible to distinguish between the planet signal and other sources[68],[4].

The choice of array configuration has significant consequences on the achievable characteristics and performance of the system, as studied in Chapter 3. However, no single array design is universally optimal. For example, Lay's analysis found that while the linear array excels in modulation efficiency and inner working angle, it has the worst stellar leakage value, necessitating another trade-off[65]. The X-Array, on the other hand, is considered the ideal configuration from an optical point of view as it offers a broad null and relatively high modulation efficiency[68].

2.4 Space environmental considerations

The considerations given in Section 2.2 are based on the ideal case where the only signals that are reaching the apertures are the star—which will be subsequently nulled—and the planet emissions. However, assuming that no stray light enters the apertures, the system will be influenced by other signals. This section proposes to provide a brief description of the environmental sources that will influence the detection process.

From a historical point of view, in effect, the presence of such disturbances is what essentially led to the shelving of Bracewell's initial solution, which cannot adequately filter out most of these signals, leading to many uncertainties in the detection of the system. It is therefore important to provide good modelling of such elements in order to ensure a consistent and valid expectation of detectable and undetectable systems.

The main elements that are usually considered involve the star and the planet, with the former being a main disturbance, along with the local zodiacal and exozodiacal clouds. This list is not comprehensive of all the disturbances that can arise: extinction can play a role, especially in some defined wavelengths, strongly reducing the incoming signals.

2.4.1 Target System: Star and Planet

Stars can generally be assumed to emit following Planck's law, behaving like perfect black bodies[20]; they are in general the dominant source of light in the system, requiring strong suppression for a valid detection. Exoplanets, on the other hand, contribute to the detected

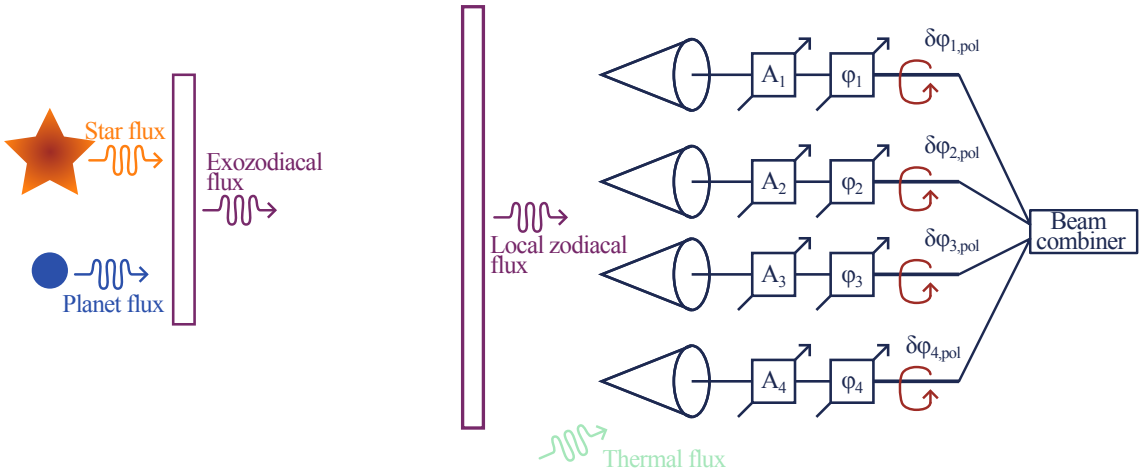

Figure 2.6: Schematic representation of systematic errors due to environmental disturbances affecting a general four aperture interferometer and the effects they produce on the amplitudes and phases received by each apertures. Adapted from Dandumont et al. 2020, and Lay, 2004[66],[20].

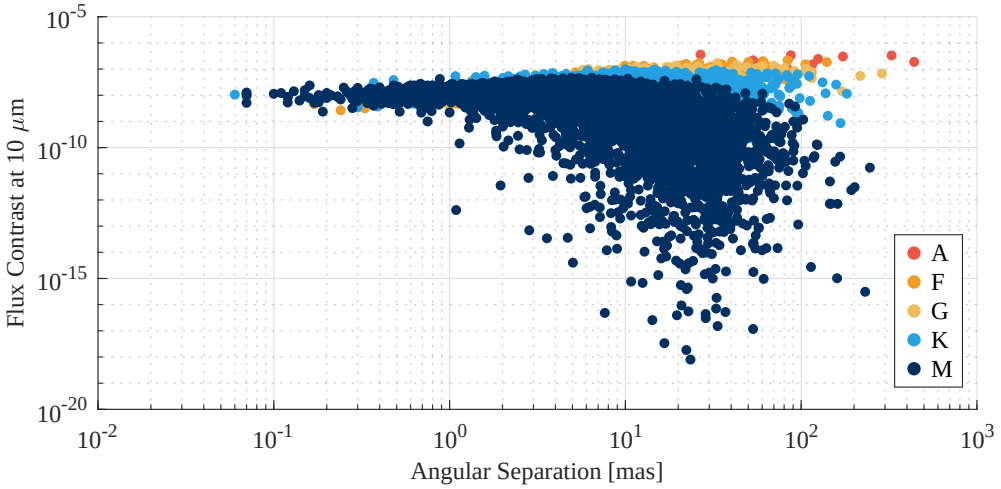

Figure 2.7: Simulated distribution of exoplanets as generated by P-Pop[52] as a function of the maximum distance from the harbouring stars and the flux contrast ratio (neglecting planetary reflection emissions) and classified based on star types. In general, the higher the baseline, the better the yield of closer-to-their-star planets will be.

flux through reflection of starlight and their own thermal emission[20]. The reflected part is clearly only a fraction of the star's emitted flux, depending on the albedo and phase in observation, while the thermal emission is a function of the effective temperature and the emissivity value (in fact, they do not generally behave like black bodies at all).

The contrast between the star and the planet determines the required null depth of the interferometer, a parameter that will characterise part of the description in the following Chapters 3 and 4, adding further value to the choice of the infrared region. Once again, it must not be forgotten that the actual detection is a function of many different parameters. For example, while lower-mass M stars (usually dwarfs) actually provide a better contrast ratio, they require longer baselines due to the proximity of the planets to the harbouring stars[21].

The situation is described by Figure 2.7, which shows the generated exoplanets by the P-Pop simulator[52] (as presented in Appendix B). Effectively, M-type stars reach much lower flux contrasts compared to other types; however, they are limited to higher angular

separations, making them harder to spot.

The exoplanet's orbital position, in fact, presents a key obstacle in detection: planets that are too close to the star may be obscured (due to the much higher stellar fluxes) and thus undetectable, leading to the necessity of multiple revisits and thus reducing the detection efficiency (this is known as the obscurational completeness[20],[9]).

2.4.2 Local zodiacal cloud

The local zodiacal cloud consists of interplanetary dust particles within the Solar System, mainly found between the orbits of Mercury and Jupiter, that scatter sunlight across all wavelengths and emit in the mid-infrared, thus dominating sky brightness in this region of great interest for exoplanet detection[20],[56].

The emissions have been modelled thanks to observations from the COBE and SPITZER missions, following the Kelsall et al. model[56], which provides the spatial distribution and spectral properties. The zodiacal emission is dependent on the ecliptic latitude and longitude, presenting a symmetry on the ecliptic plane and becoming particularly stronger when observed towards the Sun[20].

This is consistent with many past missions, like Darwin[70] and TPF-I[88], which planned positions at L_2 or, even better, at several astronomical units from the Sun, reducing the zodiacal background by observing only along specific directions in the sky along the anti-Sun direction[25],[4]. However, the residual emission can still contribute to photon noise, which must be taken into account[4],[91].

Besides, it can be shown that the planetary flux dominates over the local zodiacal background by at least one order of magnitude, making it the less concerning disturbance in the discussion, even when fluctuating[2].

2.4.3 Exozodiacal cloud

Similarly to the Solar System, it is assumed that any other star system could possibly possess its own exozodiacal cloud[21]. The presence of dust in an exoplanetary system can introduce significant background noise that can overpower the planet's signal, particularly when the dust is warm, thus emitting in the mid-infrared.

Observations using the Large Binocular Telescope Interferometer (LBTI) have established constraints on exozodiacal emission levels, indicating that most nearby stars exhibit exozodiacal dust levels below 27 times the Solar System's zodiacal emission (27 zodis, where 1 zodi is the level of emission of our Solar System) at a 95% confidence level[20]. Simulations, however, highlight that the zodi values are influenced by the star class, being limited for F and G stars in the Darwin catalogue but extending up to 100 zodis for K-type stars and up to 200 zodis for M-stars[2].

The exozodiacal dust's inclination and density profile influence its detectability, with edge-on discs creating signals that can mimic exoplanetary signatures in interferometric measurements, leading to possible misinterpretations of the results[2].

Luckily, there are efficient solutions to this problem, thanks to the fact that the signal of the exozodiacal dust is symmetric, as will be addressed in Section 3.5: techniques like phase chopping can significantly reduce the risk of false positives.

Gravitational interactions with large exoplanets can clear inner regions of the dust disc, reducing its impact on observations. However, dust drifting inward due to Poynting-Robertson drag can accumulate in resonant structures, forming clumps that may introduce additional confusion in planet detection. While these structures are not expected to be as bright as planetary signals, their presence must be carefully accounted for in data

analysis[2],[25],[56].

To optimise observation strategies, planetary population synthesis tools incorporate exozodiacal dust models based on IRAS and DIRBE data, allowing for realistic estimates of background contributions. Despite these efforts, exozodiacal emission remains a fundamental challenge for nulling interferometry, necessitating ongoing improvements in instrument sensitivity and data analysis techniques[2].

2.5 Data processing and analysis

Once the signal has been detected by the chosen sensor, the process is far from over: the analysis presented in Chapter 3 is mainly based on the reading of a photon count by the sensor. However, accurate signal extraction is fundamental for obtaining accurate results[22].

Signal reconstruction and extraction algorithms are core components of any mission, as their quality will ultimately limit the amount of data that can be extracted. These algorithms should be implemented both for the characterization phase and, most importantly, the initial research phase[22]. A ranking, based on the characteristics of the exoplanet (radius, effective temperature, and angular separation)—which will necessarily be based on a single, brief observation[22]—will allow the discernment between valid and less interesting objects, which will later be studied during the characterization phase.

Throughout the evolution of nulling interferometry, multiple algorithms have been proposed. Generally, a time series of results from multiple baselines or observations is reduced into a model. However, this approach may be particularly problematic for a space-based nulling interferometer[27], due to the small size of the system and the dominance of disturbances, potentially leading to false positives.

For TPF-I, for example, a convolution method based on a modified CLEAN algorithm has been proposed[27]. This method is based on the distinction of sources from the sidelobes of a dirty map (which will be discussed in Section 3.8).

Darwin, on the other hand, relied on a signal extraction method based on a maximum-likelihood approach that has also been proposed and enhanced for LIFE[22],[91]. This method is based on defining a parameter to quantify the validity of an exoplanet detection based on the signal-to-noise ratio[22].

3 Modelling of Interferometry

This chapter introduces the mathematical tools that will be used to create a model of nulling interferometry, starting from physical concepts and definitions of figures of merit and proceeding with mathematical developments to acquire valid expressions that can be used to evaluate the performance of an instrument within a numerical analysis, comparing the yield and the behaviour of different configurations in an optimisation pattern.

While for two-element interferometry most of the following concepts simplify to nice expressions while keeping the analysis as generic as possible, for multiple apertures the expressions generally remain complex yet generically fully applicable in the analysis.

Starting from the definition of the amplitude and intensity of the interference, analysed in Section 3.2, the response functions and the transmission maps are evaluated: these elements are key factors in the analysis as they are considered to be the main figures of merit of a nulling interferometer, as they lead to many considerations, as discussed in Section 3.3. Section 3.4 introduces a simple algorithm to define an optimal way to retrieve the best phase shifts to impose on the nulling interferometer (i.e., to reach the best nulling).

These considerations allow us to eventually retrieve some possible transmission maps for the considered arrays in the following analysis, as analysed in Section 3.5, leading to the definition of some other fundamental figures of merit like the nulling ratio and rejection factor as seen in Section 3.7.

Other figures of merits are evaluated thanks to the analysis of the Point Spread Function in Section 3.8, where the response to an off-axis planet is derived, analysing the modulation efficiency, as well as other key parameters like the inner and outer working angles. Eventually, Section 3.9 presents an overview of the main findings withing this chapter.

3.1 Example configurations

In the following sections, different aspects of nulling interferometry will be investigated by analysing both the theoretical aspects and possible numerical implementations to evaluate potential results and establish a baseline metric for the performance that future missions can achieve.

Therefore, there is a need to select general elements that realistically reflect a real-case scenario. Following the considerations also analysed in Carboni[13] regarding the fairing of currently operational launchers, as well as proposals for possible future missions, like the one proposed by the consortium by TU Delft, KU Leuven and CSL[17], a baseline of 10.5 m was chosen: in contrast with older missions which involved satellites constellation, the new proposal involves a single deployable spacecraft.

Parameter		X-Array		Linear Array	
		x	y	x	y
Apertures	1st [m]	4.70	2.35	5.25	0
	2nd [m]	4.70	-2.35	1.75	0
	3rd [m]	-4.70	-2.35	-1.75	0
	4th [m]	-4.70	2.35	5.25	0
Aperture ratio		2:1		3:1	
Baseline [m]		10.5		10.5	
Aperture surfaces [m^2]		1.25		1.25	
Aperture diameter [m]		1.27		1.27	
Intensities† [m^2]		0.25		0.25	
Beam combiner efficiency		25%		25%	
Optical line efficiency		20%		20%	

Table 3.1: Summary of considered data in the numerical analysis presented in this chapter, following the considerations from Carboni and the Consortium by TU Delft, KU Leuven, and Centre Spatial de Liège[13],[17]. The order presented in the matrix elements follows the order presented in Figure 3.1. Data for the efficiencies from Lay[65]. † Following the same convention proposed by Lay, the intensity is a scaling of the aperture area following Equation 3.1.

Regarding the choice of array, while numerous configurations have been proposed over time, as presented in Section 2.3, the analysis focuses on the most common configurations: the X-Array and the Linear Array. Given their different structures—one being mono-dimensional and the other bi-dimensional—all possible considerations for both approaches are taken into account. As explained in the same section, there is a strong preference for adopting in-plane configurations to avoid strong thermal fluxes; therefore, an out-of-plane configuration was not considered in the following analysis.

The selected reference wavelength is 10 µm, in accordance with the considerations addressed in Chapter 1. The validity of this choice will also be addressed in the sensitivity analysis presented in Chapter 4, where smaller wavelengths present excessively stringent requirements on the maximal exhibited displacements from the reference positions for optical systems, as well as from incoming disturbances.

Figure 3.1 presents an overview of the two selected configurations with the numbered apertures and in scale, while Table 3.1 summarises the selected parameters for the following analysis; particular caution must be taken in the definition of the intensity of the apertures, measured in square metres due to itself being a rescale of the aperture surface as seen in Equation 3.1 and defined by Lay[65].

3.2 Interference Amplitude and Intensity

Starting from the theoretical concepts explained in Section 2.2, it is possible to generalise the concept by adopting a mathematical description of the behaviour of the electrical fields reaching the apertures and thus compute the response of the interferometer.

Let us assume a general interferometer with N apertures. Its response amplitude W is given by the sum over every aperture of the amplitude signals (which is evidently linked to the surface of the aperture by transmission and beam combiner efficiencies[65]) with its associated phase, which will later be extended into the explicit dependence on its position[65],[72],[77]:

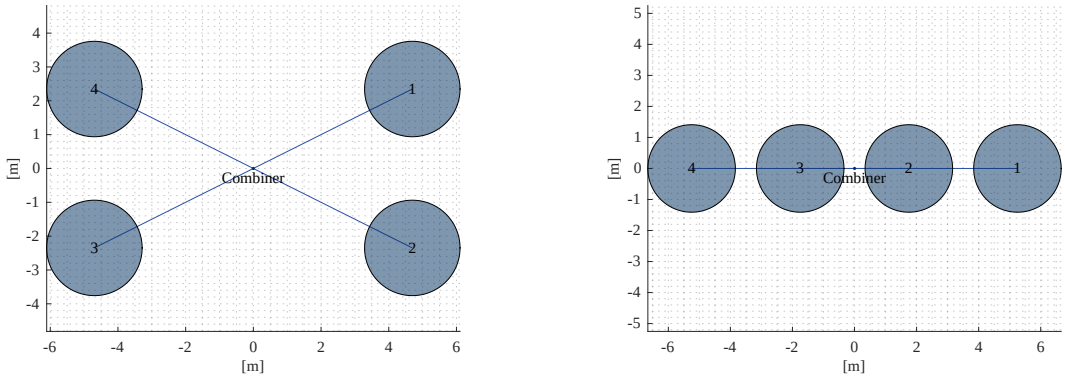

(a) X-Array **(b)** Linear Array

Figure 3.1: Comparison of the two proposed configurations (in scale). The apertures are numbered as they will be referenced within the discussion.

$$W = \left| \sum_{k=1}^{N} A_k e^{i\varphi_k} \right| \qquad \text{where } A_k^2 = \pi D_k^2 \eta_{opt,k} \eta_{bc,k} \tag{3.1}$$

and where A_k, φ_k and D_k are, respectively, the intensity, the phase and the diameter associated to the k^{th} aperture, η_{opt} is the efficiency linked to the optical lines (a function of the number of mirrors and splitters along the path of the light and is usually very low; for small baselines like those possibly achievable in space, a value of 0.2 can be assumed), while $\eta_{bc,k}$ is the efficiency associated with the beam combiner, which is more efficient, around 0.25, in general, as presented in Section 3.1 and assumed from Lay, 2005[65].

Exploiting Euler's formula from the exponential to Cartesian form, it is possible to derive a simplified, real expression of Equation 3.1:

$$\begin{aligned} W &= \left| e^{i\varphi_1} + e^{i\varphi_2} + e^{i\varphi_3} + e^{i\varphi_4} + \cdots \right| = \left| \sum_{k=1}^{N} A_k \left(\cos(\varphi_k) + i \sin(\varphi_k) \right) \right| = \\ &= \left| \sum_{k=1}^{N} A_k \cos(\varphi_k) + i A_k \sum_{k=1}^{N} \sin(\varphi_k) \right| = \sqrt{\left(\sum_{k=1}^{N} A_k \cos(\varphi_k) \right)^2 + \left(\sum_{k=1}^{N} A_k \sin(\varphi_k) \right)^2} = \\ &= \sqrt{A_1^2 + A_2^2 + \cdots + 2A_1 A_2 \cos\varphi_1 \cos\varphi_2 + 2A_1 A_3 \cos\varphi_1 \cos\varphi_3 + \cdots} = \\ &= \sqrt{\sum_{j=1}^{N} \sum_{k=1}^{N} A_j A_k \cos\left(\varphi_j - \varphi_k\right)}. \end{aligned} \tag{3.2}$$

As it follows that the intensity is half the square of the amplitude, then one can find

$$I = \frac{1}{2} \sum_{j=1}^{N} \sum_{k=1}^{N} A_j A_k \cos\left(\varphi_j - \varphi_k\right). \tag{3.3}$$

This equation shows that, for a specific angular position, its intensity is a combination of the phase differences from all the branches of the interferometer. It follows that the goal

of nulling interferometry, as addressed, is to combine the phases of the different apertures in order to enhance specific positions while negating others. However, in addition to the desirable phase shifts, caution must be taken for the presence of wavefront errors induced by the optical elements of the system as well as the presence of other disturbing factors, which will be addressed in Chapter 4.

3.3 Response Function

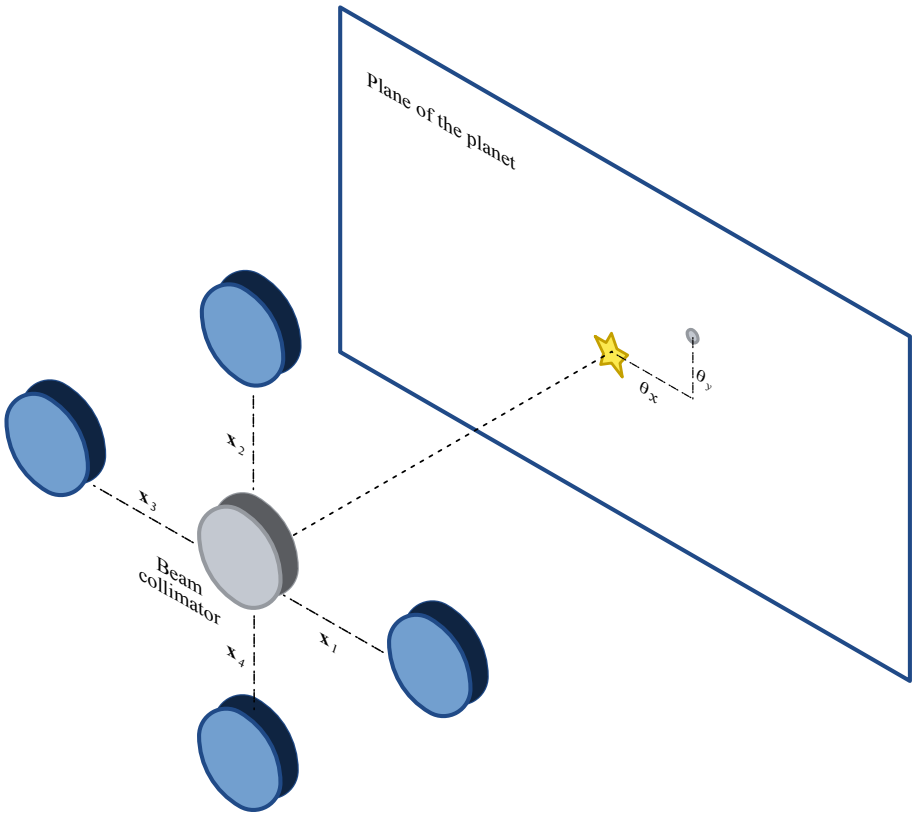

Figure 3.2: Diagram of the considered system: taking as reference the direction of the combiner and the star, assuming the interferometer to be in a plane configuration, normal to this direction, it is possible to identify the positions of the different apertures with bidimensional vectors $\mathbf{x}_i$, as well as every position on the image plane (which is a projection of the three-dimensional space) with the angular positions $\boldsymbol{\vartheta}$.

By developing the phase terms from Equation 3.3, in order to make explicit the dependency on the baseline and spatial position, in the ideal case the intensity corresponds to the response function of the system[65],[2]:

$$R(\boldsymbol{\vartheta}) = \frac{1}{2}\left|\sum_{k=1}^{N} U_k A_k \exp\left(i\frac{2\pi\ \mathbf{x}_k \cdot \boldsymbol{\vartheta}}{\lambda} + i\Delta\Phi_{jk}\right)\right| = \\ = \frac{1}{2}\sum_{j=1}^{N} U_j \sum_{k=1}^{N} A_j A_k \cos\left(\frac{2\pi\ \boldsymbol{\vartheta}}{\lambda}(\mathbf{x}_j - \mathbf{x}_k) + \Delta\Phi_{jk}\right), \quad (3.4)$$

where $\boldsymbol{\vartheta}$ indicates the vectorial position of the source on the normal to the apertures direction plane, $\mathbf{x}_j$ the position of the j^{th} aperture, always in the same plane, taking as a reference position the beam combiner and Φ_k is the possible added delay along a line

and U_k is the amplitude scaling value, in order to obtain the desired nulling result. A representation of the considered situation is presented in Figure 3.2.

Generally speaking, while $\mathbf{x}_j$ is a function of the position and thus the result of mechanical constraints and considerations on the fringe spacing (from the diffraction theory), both U_k and Φ_k are free variables that can be optimised (as addressed in Section 3.4) but can also be chosen freely (with the restraint on the $\mathbf{U}$ matrix, which needs to be orthonormal, i.e. having a unitary determinant in order to avoid unphysical results where the incoming energy is lower than the outgoing one).

In general, once the transmission map of the system is known, it is possible to retrieve the photon rate incident (without undesired effects like stray light or thermal photons) on the detector through an integration of the response function:

$$N = \iint B_{\text{sky}} R P \, \mathrm{d}\Omega. \tag{3.5}$$

In this equation, B_{sky} is the brightness distribution of the sky and P is the taper function, which essentially is a function of the field of view of the instrument; as R, P is the only other instrument-related design element[25].

3.4 Optimised Signal Splitting Strategies

A more complete evolution of the expression in Equation 3.4 exploits a matrix representation[44]. Given the vector $\mathbf{V}$ of the aperture amplitudes at their entrances, a system can, in theory, have an infinite number of outputs given by the linear combinations of the inputs,

$$\mathbf{W} = \mathbf{U}\mathbf{V} = \begin{bmatrix} U_{11} & \cdots & U_{1a} \\ \vdots & \ddots & \vdots \\ U_{a1} & \cdots & U_{aa} \end{bmatrix} \begin{bmatrix} A_1 \exp\left(i \frac{2\pi \, \mathbf{x}_1 \cdot \boldsymbol{\vartheta}}{\lambda}\right) \\ \vdots \\ A_a \exp\left(i \frac{2\pi \, \mathbf{x}_a \cdot \boldsymbol{\vartheta}}{\lambda}\right) \end{bmatrix} \quad \text{where } a \in \mathbb{N}. \tag{3.6}$$

Again, the intensity is given by half the square of the output vector $\mathbf{W}$. Clearly, due to conservation laws, the matrix $\mathbf{U}$ must be orthonormal. For simplicity, let us assume that the combination matrix $\mathbf{U}$ is square (having, then, N rows and columns, like the number of apertures).

3.4.1 Singular Value Decomposition

Guyon et al., 2013 proposed a methodology[44] to optimise the choice of $\mathbf{U}$ (and, consequently, the imposed phases Φ) in order to obtain the best possible signal-to-noise ratio—that is, the best nulling depth for the given configuration.

In the most general case, by considering a partially resolved star of dimension $0.001\lambda/B$[1], performing a singular value decomposition of the $\mathbf{V}$ vector evaluated over N_{pt} points across the assumed star dimensions, the left singular vector matrix $\mathbf{U}$ is such that

$$\mathbf{V}_{N_{pt} \times N} = \tilde{\mathbf{U}} \mathbf{S} \tilde{\mathbf{V}} \tag{3.7}$$

identifies a "modal" matrix $\tilde{\mathbf{U}}$, while the singular values along the diagonal of $\mathbf{S}$ express the amount of stellar energy present in each "mode"[44]. In practice, the optimal combination corresponds to the last "mode," i.e. the last column of the $\tilde{\mathbf{U}}$ matrix.

[1] This value is significantly smaller than common stars that would be studied by an interferometer; however, it is chosen solely for optimisation purposes in order to obtain size-independent results[44].

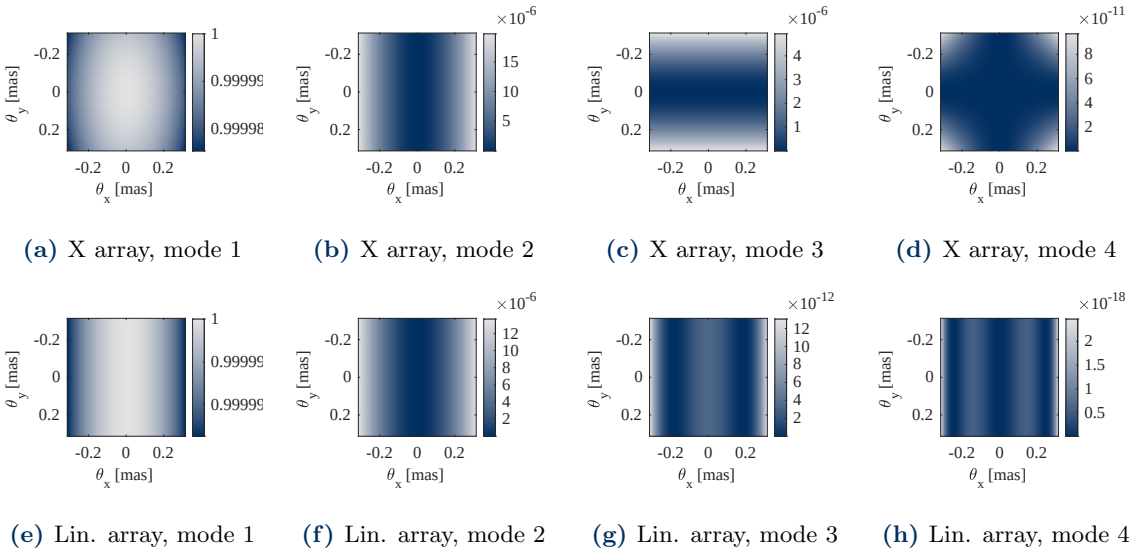

(a) X array, mode 1 **(b)** X array, mode 2 **(c)** X array, mode 3 **(d)** X array, mode 4

(e) Lin. array, mode 1 **(f)** Lin. array, mode 2 **(g)** Lin. array, mode 3 **(h)** Lin. array, mode 4

Figure 3.3: Results of the SVD operation for the output **W** squared and normalised over the assumed angular dimension of the star, for both a proposed X-array and a linear array. In this case, it is clear that "mode" 1 includes most of the stellar intensity, while "mode" 4 offers the best reduction.

Figure 3.3 shows the resulting "modes" for two theoretical configurations (a 2:1 ratio X-array and a linear array with single baselines and intensities). It is evident that, while Figures 3.3a and 3.3e display almost no displacement in the map, with values always close to 1, the last mode, which is the optimised one, as expected, presents values very close to zero.

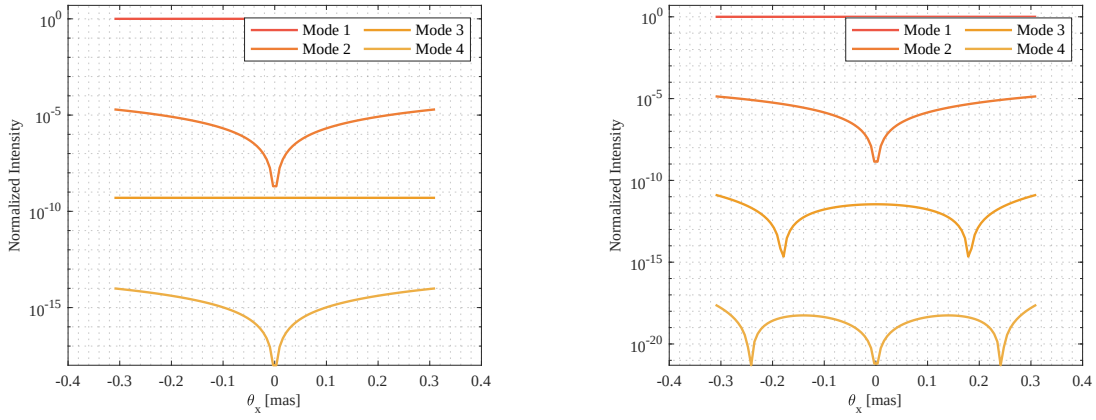

(a) X array **(b)** Linear array

Figure 3.4: Comparison of all modes, in terms of normalised intensity, along the direction $\vartheta_y = 0$ using a logarithmic scale.

This is further emphasised in Figure 3.4, where the normalised intensity is plotted for points along the horizontal centred direction. It is evident that, while modes 1 and 3 exhibit an almost constant behaviour, which is a highly undesirable feature for nulling interferometry, both modes 2 and 4 demonstrate a predefined nulling depth, with the latter being the most effective in reducing the partially resolved star. The same results are also reported in Table 3.2 for quick comparison.

From a practical perspective, elements of **U** have both a phase and a magnitude that can

be realised in the combiner:

- Phases can be obtained using a chromatic phase-shifting plate. In most cases, these simply introduce a π shift (a negative sign).
- Amplitudes can be achieved by solving a beam splitter system composed of different reflection and transmission glasses.

In this regard, Guyon et al., 2013[44] also proposes an optimised beam combiner, which combines a specific configuration of beam splitters with chromatic phase-shifting plates. However, this lies outside the scope of this thesis.

	X-Array		Linear Array	
Aperture	**Phases**	**Amplitudes**	**Phases**	**Amplitudes**
1	π	0.5	0	0.22
2	0	0.5	$-\pi$	0.67
3	$-\pi$	0.5	0	0.67
4	0	0.5	$-\pi$	0.22

Table 3.2: Results of the singular value decomposition analysis for the two considered arrays.

3.4.2 Taylor expansion

Another approach that can be evaluated follows an analytical development proposed by Mennesson and Mariotti, 1997[77], which is developed by expanding the complex amplitude response (Equation 3.4) around the central point in polar coordinates (where δ_k is the telescope phase position and φ is the azimuth angle of the point source):

$$\sum_{j=1}^{N} A_j \, e^{i\frac{2\pi x_j \vartheta_x}{\lambda}\cos(\delta_j-\varphi)} \cdot e^{i\varphi_j} = \\ = \sum_{j=1}^{N} A_j \left(1 + i\, x_j \cos(\delta_j - \varphi) - i\frac{x_j^2}{2}\cos^2(\delta_j - \varphi) + o(x_j^2)\right) \cdot e^{i\varphi_j}. \quad (3.8)$$

This leads to a series of conditions that should be enforced to achieve a certain degree of suppression. By considering only the first order, effectively, the condition to have ϑ^2 dependency on the off-axis source is given by[77]

$$\sum_{j=1}^{N} (1 + o(1)) \cdot e^{i\varphi_j} = \sum_{j=1}^{N} e^{i\varphi_j}. \quad (3.9)$$

This condition is satisfied by the optimal decomposition using the SVD analysis, as follows by using data in Table 3.2. A fourth-order extinction is found by using the second-order condition[77],

$$\sum_{j=1}^{N} x_j \cos(\delta_j - \varphi) \cdot e^{i\varphi_j} = 0. \quad (3.10)$$

Again, given the symmetry of the considered arrays, the condition is satisfied by the SVD analysis. The system can be expanded to any order, but in general, it can be exploited to find some solutions for the positions of the arrays[77] by solving Equation 3.8 to the desired order.

3.5 Transmission Maps and Phase Chopping

Let us assume the two generic configurations defined in Table 3.1, an X array and a linear array (where apertures 1, 3 and 2, 4 respectively are combined together in a Double Bracewell's combination). A transmission map is the evaluation of the response function (Equation 3.4) over different angular positions in order to evaluate the fringes around the star.

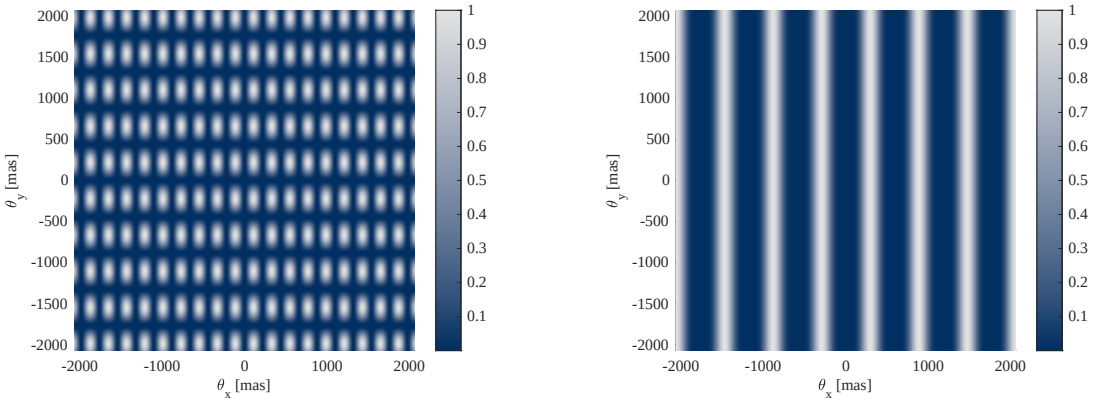

(a) X array **(b)** Linear array

Figure 3.5: Normalised transmission maps for two generic arrays, computed by evaluating the response function over a mesh of angular positions around the central position, which is the star.

Figure 3.5 displays two possible transmission maps for two symmetric arrays, which have been obtained using the optimal splitting theory seen in Section 3.4. As expected, the Linear Array map displays a mono-dimensional fringe pattern, while the X-Array shows a bi-dimensional pattern, as expected from Equation 3.4 (where, in the dot product, y being zero cancels out any contribution from ϑ_y).

Phase chopping is a technique that has been developed to reduce the systematic problems of nulling interferometry, which include the zodiacal and exozodiacal dust discs along with instrumental background[65],[2]. Phase chopping is an internal modulation of the signal where there is a rapid switch of the input beams, with the observation of mirrored states or the subtraction of the two[87].

In its simplest approach, phase chopping considers two different states of the response, with the latter $\mathbf{W}^-$ having a negative phase with respect to the former $\mathbf{W}^+$ (which is computed as illustrated in Equation 3.6). The chopped system response is then[65]:

$$T_{\text{chopped}}(\boldsymbol{\vartheta}) = \frac{1}{2}\left|\mathbf{W}_+^2(\boldsymbol{\vartheta}) - \mathbf{W}_-^2(\boldsymbol{\vartheta})\right|. \tag{3.11}$$

For a more quantitative result, Figure 3.6 shows the transmission maps and the phase-chopped transmission maps along the horizontal direction for the two general arrays, along with different nulling ratios[77]. Along the curves of the standard and chopped signal, trend curves for specific rejection ratios p following the law ϑ^p are shown: linear arrays are able to reach higher rejection rates with respect to bi-dimensional arrays[2].

The superiority, at least for this particular aspect, of the linear array is confirmed also by the analytical development proposed in Section 3.4.2, where an analytical solution for ϑ^6 is found by using a linear configuration as evaluated by Mennesson and Mariotti, 1997[77].

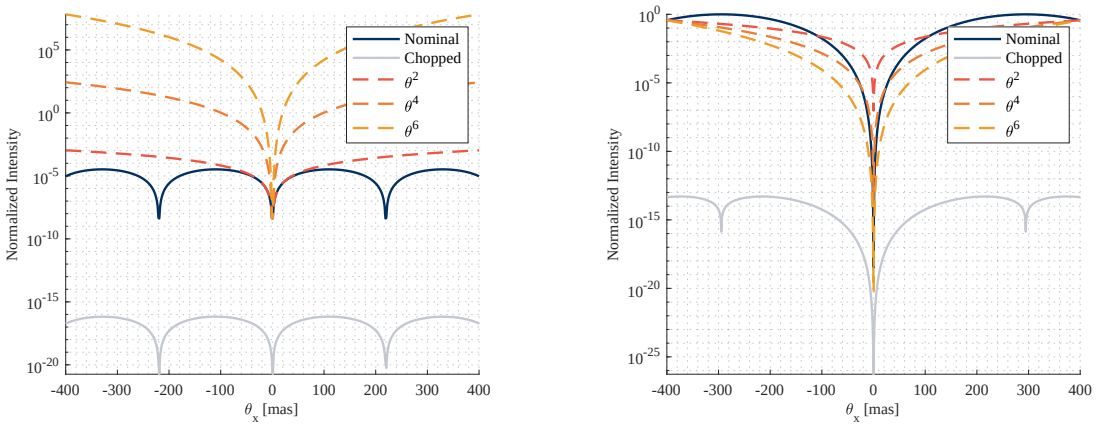

(a) X array **(b)** Linear array

Figure 3.6: Comparison of the transmission map and the phase-chopped transmission map evaluated along the horizontal direction with respect to different angular trends for nulling performance.

3.6 Baseline Typologies and Configurations

Section 3.4 has introduced a simple way to obtain the optimal phase shift for each aperture in order to maximise the nulling ratio of the system. While the analysis proposed up to now considered each aperture on its own, it is important to highlight that their contribution is often to be seen as coupled, creating a baseline. In this context, a baseline is any distance between two apertures and has a slightly different meaning from the interferometric baseline that is elsewhere referred to (which is, in general, the maximum baseline). In general, the number of possible permutations where the order matters, without repetition, is given by

$$P(n,r) = \frac{n!}{(n-r)!}, \tag{3.12}$$

where n is the number of different apertures and r is the number of apertures to permute (in the case of a baseline, just 2 elements), leading to, having 4 apertures, 12 possible baselines. However, some of these baselines are repeated, therefore a need to extract the unique baselines arises. A baseline is distinct if it has both a unique baseline distance (the Euclidean norm of the coordinate differences of its points) and a unique phase difference[65].

Once the unique baselines have been extracted, it is possible to define the baseline amplitude factors, which will be useful in the subsequent analysis concerning the efficiencies and the point spread function[65]:

$$C_i = 2\sum_{j}^{k}\sum_{k}^{N} A_j A_k \sin\Delta\varphi_{jk} \times \delta(|\Delta x_{jk}| - \Delta x_i)\delta(|\Delta y_{jk}| - \Delta y_i). \tag{3.13}$$

After the introduction of the concept of phase chopping, it is possible to distinguish the baselines based on their effect on the chopped photon rate[65]: in fact, following from Equation 3.11, not all the baselines contribute to the imaging processes. Therefore, a possible classification of the contributions is given by the following[65]:

- **Imaging baselines.** A baseline is said to be an imaging baseline if

$$\sin(\varphi_j - \varphi_j) \neq 0. \tag{3.14}$$

- **Nulling baselines.** A baseline is said to be a nulling baseline, therefore being important for reducing the stellar leakage, if

$$\cos\left(\varphi_j - \varphi_j\right) \neq 0. \tag{3.15}$$

- **Mixed baselines.** If the phases involved in a baseline are not multiples of $\pi/2$, then in this case the baselines are said to be mixed, offering a contribution in both nulling and imaging.

Dist. bas.	**Type**	**Length** [m]	**Phase diff.** [deg]	**Factor**	**Contributions**
X-Array					
1	Nulling	4.696	180	0.00	1-2, 2-1, 3-4, 4-3
2	Nulling	10.500	360	-0.00	1-3, 3-1
3	Nulling	9.391	180	0.00	1-4, 2-3, 3-2, 4-1
4	Nulling	10.500	-0	-0.00	2-4, 4-2
Linear Array					
1	Nulling	3.500	180	0.00	1-2, 2-1, 2-3, 3-2, 3-4, 4-3
2	Nulling	7.000	-0	-0.00	1-3, 2-4, 3-1, 4-2
3	Nulling	10.500	180	0.00	1-4, 4-1

Table 3.3: Classification of distinct baselines for the two proposed arrays in terms of type, length, and contributing repeating baselines for the considered arrays. The numbering associated to the contributing apertures is referenced from the presented configurations in Figure 3.1.

For the two arrays considered here, it is possible to visualise the results in terms of the two proposed arrays as seen in Table 3.3. The first important distinction is that the X-Array presents four distinct unique baselines, while the Linear Array presents only three, at least with the considered data given in Section 3.1 (depending on the specified phases and baselines, the number can increase or decrease up to 6, half of the permutation result, in the case of a random scatter of points). One particular aspect arises in the X-Array for the second and fourth baselines, where the sign of the phase difference is determinant in their distinction.

For the particular case of the optimal splitting following the SVD analysis, all the baselines appear to extensively contribute to a nulling process, displaying a null factor. This is not the case when other types of phase differences are selected in the analysis, as they will be considered later on.

3.7 Nulling Ratio and Rejection Factor

Results achieved with the shown description allow us to reach a complete nulling at the origin of the transmission map (in the absence of noise sources, which will be addressed later) as seen in the transmission maps. This works for unresolved stars, but nearby stars actually display a finite dimension, following the law

$$\vartheta_* \approx \frac{d_*}{D_*}, \tag{3.16}$$

where d_* is the dimension (diameter) and D_* is the distance to the object. The relation is valid for $d_* \ll D_*$ but, in general, means that some of the star leakage will enter the interferometer. In general, this is known as geometric leakage and is a consequence of nulling properties. However, disturbances, which will be introduced in Chapter 4, will create further discrepancies between the ideal case and the real situation.

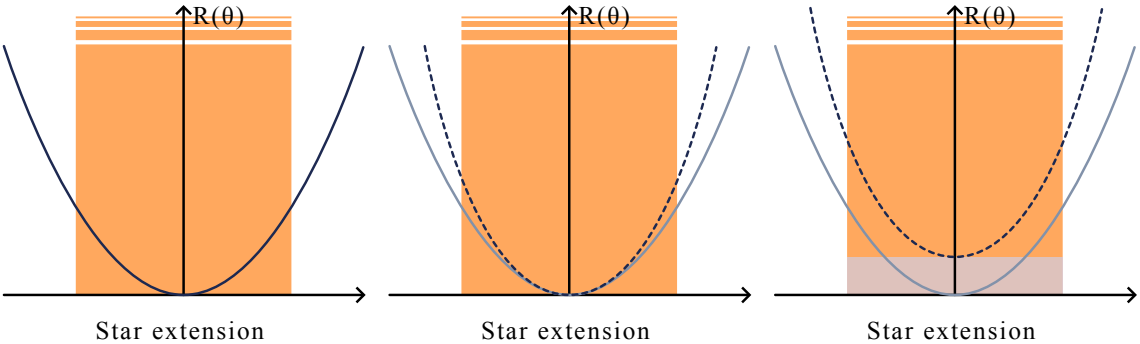

(a) Geometric leakage **(b)** Perturbed geometric leakage **(c)** Null floor perturbations

Figure 3.7: Representation of different contributions to the transmission map outputs in terms of geometric leakage, perturbed geometric leakage, and null floor perturbations: from the ideal case where transmitted stellar light is minimal, there is an increment of disturbances on the effective result[25],[66].

The situation is illustrated in Figure 3.7, where essentially the idealised signal, as found in Section 3.5, is perturbed, therefore leading to an unoptimised response by the interferometer.

Considering now only the ideal situation, as reported in Figure 3.7a, in general, the nulling ratio G is the ratio between the transmitted flux and the initial flux at the input of the beam combiner (assuming an efficiency $\eta_{bc} = 1$)[25],[2]:

$$G = \frac{N_g}{\sum_j^N N_{*,j}}, \tag{3.17}$$

where N_g is the geometric leakage. By considering only the main perturbation (which is the stellar leakage, as it will be addressed in Chapter 4), it reduces to

$$N_g = \sum_j^N \sum_k^N A_j A_k \cos(\varphi_j - \varphi_k) \bar{B}_{*jk}, \qquad \text{where} \quad \bar{B}_{*jk} = 2F_* \frac{J_1\left(\frac{2\pi b_{jk}\vartheta_*}{\lambda}\right)}{\frac{2\pi b_{jk}\vartheta_*}{\lambda}}. \tag{3.18}$$

In this equation, the stellar brightness $\bar{B}_{*jk}$ depends on the stellar flux F_* at the desired wavelength λ and the first kind first order Bessel function $J_1(x)$, which itself depends on the considered baseline b_{jk} and the stellar angular diameter ϑ_*, computed, for example, using Equation 3.16.

$N_{*,j}$ instead, is the j^{th} input to the beam combiner; in this case, assuming equal amplitudes as inputs,

$$\sum_j^N N_{*,j} = NA^2F_*. \tag{3.19}$$

With two apertures, the equation reduces to a simplified expression which avoids any summation, but this is not the case for a general N apertures interferometer. In fact, in this case, the nulling ratio, as derived in Appendix A.1, becomes, under the assumption of equal amplitudes,

$$G = \frac{1}{N}\left[N + \sum_{j\neq k} \cos(\phi_j - \phi_k) \frac{2J_1\left(\frac{2\pi\, b_{jk}\, \theta_\star}{\lambda}\right)}{2\pi\, b_{jk}\, \theta_\star/\lambda}\right]. \tag{3.20}$$

The inverse of the nulling ratio is known as the rejection factor ρ_g

$$\rho_g = \frac{1}{G}.$$

Table 3.4 includes a comparison for the considered arrays. As expected, good nulling ratios are found for both arrays without additional disturbances. However, the X-Array, thanks to its bi-dimensional contributions and additional baseline effects, appears to achieve a higher nulling ratio, significantly higher than its linear counterpart. Clearly, it must be underlined that this is only the result of an ideal analysis without any sensitivity to external factors that will, nonetheless, strongly diminish the quality of the result, as will be analysed in Chapter 4.

Additionally, as remarked in Section 3.5, the Linear Array presents a better off-axis trend, following a higher-order ϑ^p rejection rate, which is significantly different from the single nulling ratio approach considered here.

Configuration	Nulling ratio	Rejection factor
Linear array	1.0966×10^{-6}	9.1189×10^{5}
X array	2.5978×10^{-12}	3.8494×10^{11}

Table 3.4: Comparison of nulling ratio and rejection factor for the two considered configurations. As also addressed in Section 3.5, linear arrays are able to reach lower nulling ratios[2].

As a final notice, it must be stressed out that the nulling ratio is not necessarily a static metric, but presents an attached stability that must be ensured and verified throughout the whole sensing process[20]. In practice, a strong minimum nulling ratio that is however highly fluctuating between low and high times is significantly worse than a medium ratio that is granted at all times.

3.8 Analysis of the Point Spread Function

The Point Spread Function (PSF) represents the response of the interferometer to a point source of light, i.e. how the light from a point source is distributed in the image plane after passing through the interferometer, providing much information about its behaviour.

Following a mathematical development proposed by Lay[65], the PSF is conceptually found by performing a series of convolutions of Bessel functions with a rotated image of the baselines and summing all the self- and cross-contributions that ultimately generate the image. In practice, assuming the vectorial position of the point source under study is known, $\boldsymbol{\Theta}$, the equation reduces to

$$M(\boldsymbol{\theta}, \boldsymbol{\Theta}) = \frac{1}{2\,\mathrm{rms}(N_C)} \sum_m \sum_n C_m C_n \cdot \\ \cdot \left[J_0\left(\frac{2\pi B_n}{\lambda} \|\boldsymbol{\theta} - \boldsymbol{\beta}_{mn}(\boldsymbol{\Theta})\| \right) - J_0\left(\frac{2\pi B_n}{\lambda} \|\boldsymbol{\theta} + \boldsymbol{\beta}_{mn}(\boldsymbol{\Theta})\| \right) \right], \quad (3.21)$$

where the chopped difference output N_C, the baseline amplitude factor C_i, and the convolution factors β_{mn} are, respectively (assuming no rotation is imposed on the system):

$$N_C = \sum_j^N \sum_k^N A_j A_k \sin \Delta\varphi_{jk} \sin\left(\boldsymbol{\Delta x} \cdot \boldsymbol{\Theta}\right) \tag{3.22}$$

$$\boldsymbol{\beta}_{mn}(\boldsymbol{\Theta}) = \frac{1}{2B_n}(\boldsymbol{\Delta x}_m \otimes \boldsymbol{\Delta y}_n)\boldsymbol{\Theta}. \tag{3.23}$$

In these equations, $\delta(x)$ is the Kronecker delta, B_n is the n^{th} distinct baseline, and $\otimes$ is the outer product, making $\boldsymbol{\beta}_{mn}$ a vectorial definition.

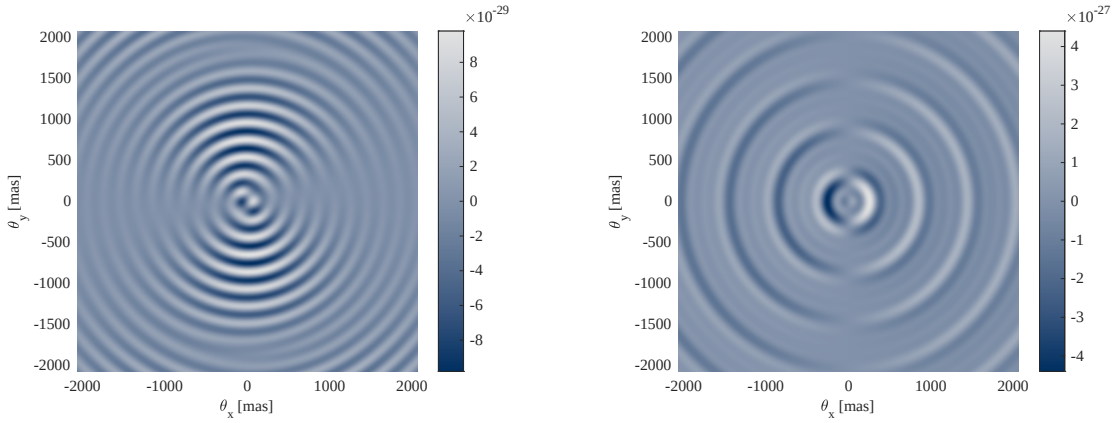

(a) X-Array **(b)** Linear

Figure 3.8: Point Spread Function of a generic array assuming an exoplanet found at (48, 0) mas for the two considered arrays.

Figure 3.8 presents the two dirty maps (i.e. sky brightness distributions, here represented by the single exoplanet position, convolved with the position-dependent PSF) associated to the studied configurations: the X-Array configuration exhibits a PSF with a more structured interference pattern, showing distinct, sharp fringes extending outward and more complex side lobe structures, while the linear configuration produces a more circularly symmetric PSF with concentric rings, which are less clear in aiding the distinction between planets and other sources.

Therefore, the X-array configuration provides better suppression of stellar leakage; the linear configuration, while producing a symmetric response, shows a simpler structure, being therefore less promising from the dirty map alone.

3.8.1 Signal Analysis

The maximum value of the obtained Point Spread Function can be interpreted as a measure of the efficiency of the selected array, i.e. its ability to convert photons incoming from the exoplanet into a signal. Higher values are therefore highly preferred, as they lead to shorter integration times required to reach a certain signal-to-noise ratio[65]. The importance of the SNR is one of the key aspects in the analysis of exoplanet yields, as the considered levels of light are very faint, as anticipated in Chapter 1.

From the expression of the dirty map in Equation 3.21, setting $m = n$, it is possible to obtain the value[65]

$$M_{\max,\infty} = \frac{1}{2} \sum_i^{\text{uniq. basel.}} C_i^2, \tag{3.24}$$

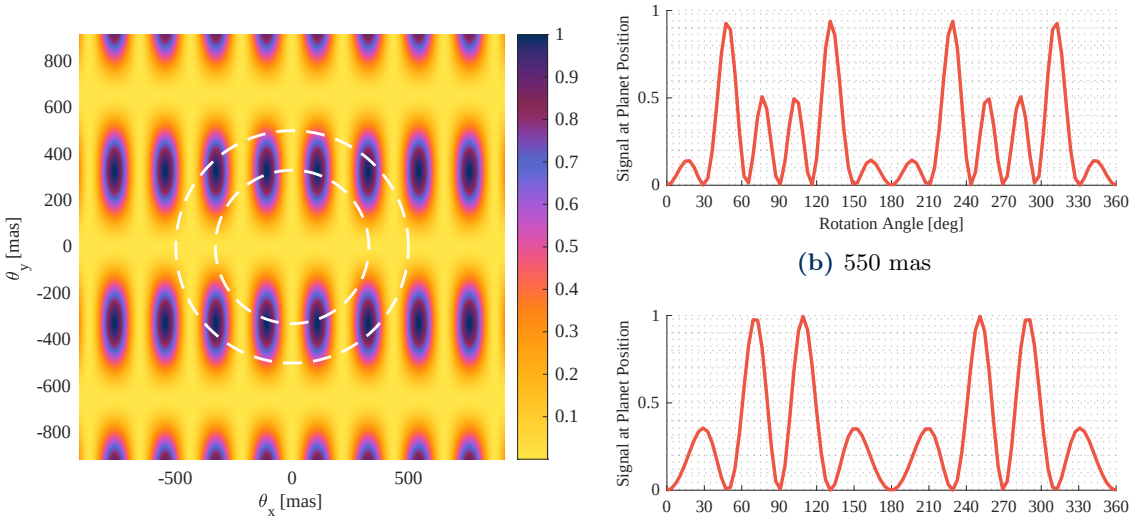

(a) Transmission map with fictitious exoplanets.

(b) 550 mas

(c) 330 mas

Figure 3.9: Comparison of the modulated signal of two different fictitious exoplanets located at 330 and 550 mas for the X-Array along a full rotation.

where, once again, the unique baseline amplification factors introduced in Section 3.6 are used.

3.8.2 Planet Modulation and Efficiency

Figure 3.9 shows how the signal of two arbitrary exoplanets would be detected along a full rotation of an X-Array while crossing the dark and bright fringes of the system, producing very different responses.

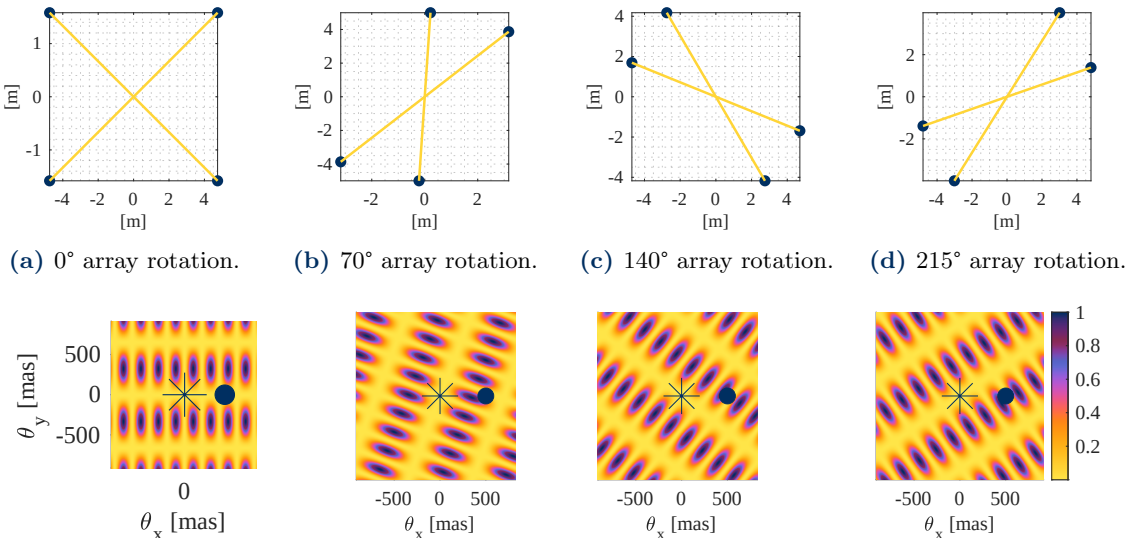

(a) 0° array rotation. **(b)** 70° array rotation. **(c)** 140° array rotation. **(d)** 215° array rotation.

(e) Map for array at 0°. **(f)** Map for array at 70°. **(g)** Map for array at 140°. **(h)** Map for array at 215°.

Figure 3.10: Example of modulation of a planet in a generic position, (550, 0) mas, represented by the blue dot, using a rotating X-Array, assuming the absence of any perturbation. All the figures share the same y-axis and colorbar.

As explained in Section 2.4, one of the biggest obstacles in detection is the presence of

the exozodiacal cloud, which, under some observation conditions, may be mistaken for an exoplanet. While phase chopping may help to mitigate symmetry problems, it is not sufficient to rule out all possible issues[3]. Modulation, therefore, is an additional technique that can be performed physically, by rotating the array, or using internal modulation, as proposed by Absil and Mennesson[3],[76].

There are multiple practical reasons to prefer internal modulation, mostly to save time during observation and to reach higher frequencies[3]. However, the process requires multiple observations. An example of the process and its potential yield is given in Figure 3.10, but a figure of merit is found by considering the modulation efficiency, which is a property of the selected array and therefore independent of the position of the exoplanet[65].

As presented by Lay[65], it is possible to extract a global expression of the root-mean-square asymptotic modulation efficiency of the array, using a parameter that is independent of baseline lengths and collecting areas. In fact, it is defined as

$$\eta_{\mathrm{rms},\,\infty} = \frac{M_{\mathrm{max},\,\infty}}{\sum_j^N \eta_{\mathrm{opt,\,j}} a_j} = \frac{\sqrt{\frac{1}{2}\sum_i^{\text{uniq. basel.}} C_i^2}}{\sum_j^N \eta_{\mathrm{opt,\,j}} a_j},$$

where a_j is the surface associated with the j^{th} aperture, and C_i is the baseline factor introduced in Section 3.6. It can then be noticed that knowledge of the dirty map allows for the derivation of specific metrics associated with the arrays.

It is important to notice that the asymptotic modulation efficiency is highly dependent on the selected phases assigned to each aperture, more so than the array shape itself; example results will be shown in Table 3.5.

3.8.3 Inner and Outer Working Angles and Angular Resolution

The inner and outer working angles are two key parameters that can be used to characterise the array in terms of absolute capabilities, defining the actual field that will be used to search for exoplanets[72].

While multiple definitions exist, following the one proposed by Lay[65], the inner working angle is the smallest angle at which the line associated with the value of the root-mean-square asymptotic modulation efficiency (as computed in Section 3.8.2) crosses the modulation curve.

The main dependency of this value is associated with the length of the nulling baselines[65], making this an extensive dimensioning parameter of the array. As anticipated in Chapter 1, the inner working angle represents the applicable minimum angular offset that can actually be studied for exoplanet presence.

An approximate formula for the inner working angle is given by[65]

$$\vartheta_{\mathrm{IWA}} \approx \frac{\lambda}{2B_{\mathrm{null}}}, \tag{3.25}$$

where B_{null} is the length of the nulling baseline.

The outer working angle is similarly important in the analysis—although it is not usually as limiting as the other parameters—defining, as the name suggests, the external limitation in the field of view of the observations. It is clear, then, that in the field of exoplanet search, the short angular separations between the exoplanets and their harbouring stars are not particularly concerned by this value. However, it is important if the mission is to be used for other observations (as was the case, during development, for Darwin[70])[21].

Again, only simplified relations exist, but the main difference from what has been explained for the IWA is that the outer working angle depends only on the aperture diameter[21]:

$$\vartheta_{\mathrm{OWA}} \approx 0.514\,\frac{\lambda}{D}. \tag{3.26}$$

As discussed in Chapter 1, another key factor for any optical system is the angular resolution, necessary to distinguish close sources like the ones here considered. Again, there is no single specific definition and one possibility involves the use of the full width at half-maximum of the central level of the main peak of the point spread function[65]. The proposed empirical definition uses

$$\vartheta_{\mathrm{FWHM}} \approx 0.48\frac{\bar{\lambda}}{\bar{B}}, \qquad \text{where} \qquad \bar{B} = \frac{\sum_i^{\text{uniq. basel.}} C_i^2 B_i}{\sum_i^{\text{uniq. basel.}} C_i^2} \tag{3.27}$$

and $\bar{B}$, $\bar{\lambda}$ are the weighted averages of wavelengths and imaging baselines lengths (effectively, since the factor C_i associated to nulling interferometers is null, then they don't contribute to the average).

It can be noticed that the angular resolution and the inner working angle are two very distinct elements: while the former is associated with the imaging capability of the array (based on the value of $\bar{B}$), the latter is associated to the nulling baselines and thus more related to the nulling ratio.

An arbitrary criterion to distinguish the two, provided by Lay[65], prescribes that the full width at half-maximum be less than half of the minimum offset angle.

3.9 Comparison of different arrays and final remarks

This chapter has introduced several mathematical tools to evaluate the response of an ideal nulling interferometer, starting from the response function—optimised under the SVD model—and moving to a possible PSF response for specific planet positions, extracting metrics for the nulling ratio, the inner working angle, and other similar elements.

Table 3.5 provides a summary of five arbitrary configurations (as also presented in Lay[65]) to provide a general summary of the metrics found for both mono-dimensional and bi-dimensional arrays. The results have been normalised with respect to the wavelength and maximum baseline (corresponding to those reported in Table 3.1), and the phases have been manually defined (and are not, therefore, a result of the SVD or the Taylor expansion solutions).

As is clear from the table, there is no clear best configuration: concerning the modulation efficiency, the second proposed configuration of the linear Double Combination Bracewell model presents a 6% higher value. However, its angular resolution, represented by the full width at half maximum peak, is more than double that of the 2:1 X-Array. The Diamond configuration presents the smallest IWA and mixed results in the other fields, but its nulling ratio is the worst in the table, and similar considerations can be made for the rest.

These results show once again, therefore, that the considered task does not present a unique best solution. Instead, the selection of the desired behaviour depends on the preferred aspects and needs to be targeted on a mission-by-mission basis. Furthermore, the results shown in this table are subject to significant change once the sensitivity analysis is taken into consideration, as will be addressed in Chapter 4.

Conf.	Ap.	Position $\mathbf{X}_j$ [L]	Position $\mathbf{Y}_j$ [L]	φ [deg]	$\eta_{\mathbf{mod},\infty}$	$\vartheta_{\mathbf{IWA}}$ [λ/L]	$\vartheta_{\mathbf{FWHM}}$ [λ/L]	G
X-Array 2:1	1	0.447	0.224	90	0.217	1.118	0.516	$10^{-5.96}$
	2	0.447	-0.224	270				
	3	-0.447	-0.224	180				
	4	-0.447	0.224	0				
X-Array 3.1	1	0.474	0.158	90	0.217	1.581	0.497	$10^{-6.26}$
	2	0.474	-0.158	270				
	3	-0.474	-0.158	180				
	4	-0.474	0.158	0				
Linear DCB A	1	0.500	0.000	270	0.217	1.500	0.720	$10^{-6.22}$
	2	0.167	0.000	90				
	3	-0.167	0.000	180				
	4	-0.500	0.000	0				
Linear DCB B	1	0.500	0.000	270	0.280	0.750	1.200	$10^{-5.62}$
	2	0.167	0.000	180				
	3	-0.167	0.000	90				
	4	-0.500	0.000	0				
Diamond DCB	1	0.500	0.000	270	0.217	0.865	0.739	$10^{-5.74}$
	2	0.000	0.291	180				
	3	0.000	-0.291	90				
	4	-0.500	0.000	0				

Table 3.5: Comparison table for five example configurations as presented in Lay[65] with normalised results for positions, modulation efficiency (higher is better), inner working angles (lower is better) and resolution angles (lower is better). Ap. is the aperture, φ is the assigned phase and G is the nulling ratio (higher exponent is better).

4 Sensitivity Analysis

Chapter 3 has introduced a mathematical description of the ideal processes occurring within an interferometer, like the transmission map and the nulling ratio. In reality, as any other instrument, the interferometer is subjected to many interferences that can disturb its functioning and its performances. This chapter will therefore analyse and evaluate the different sources of errors and their possible representation within the mathematical development of the model.

From an initial description of systematic errors, provided in Section 4.1, which gives an overview of the main sources of errors from a consideration of the literature, Section 4.2 instead develops the mathematical model to represent the nature of signal disturbances over the full analysis, offering a preview of future developments in the model.

On a different path, Section 4.3 focuses on the main source of disturbances, namely the phase: after a small introduction on how the phase affects some important metrics of interferometry, Section 4.4 links the phase to an optically measurable dimension, namely the optical path difference.

On the foundations brought by the sensitivity analysis, Section 4.5 eventually introduces the post-processing of the optical model outputs, thereby introducing another layer of development of the model that will later be considered in the next chapter.

4.1 Classification of systematic errors

Any system is characterised by both random noises–due to photon shot noises and electronic noises during the detection process, which are however controllable and can be limited to smaller amounts–, and systematic noises, which are instead driving most of the design process[66],[25] due to their larger magnitude and continuous presence.

As described by Lay[66], systematic noise, which will be the focus of this section, includes the following sources (also represented in Figure 2.6):

- Amplitude imperfections due to non-perfect reflectivity values of the involved optics and higher-order wavefront errors, as well as beam shear besides background unbalanced transmission;
- Phase imperfections due to path-length errors, causing a shift in the transmission maps and positions of the fringes, therefore leading to a non-null on-axis transmission;
- Nominal position errors for the collectors;
- Polarisation angle errors between the beams, which are essentially again affecting the phase or the intensity of the system as also modelled by Serabyn[97];
- Stray light fluctuations in the amount of stray light affecting the apertures;

- Thermal errors affecting the detector;
- Gain fluctuations in the detectors.

In summary, then, fluctuations can either affect the phase or the amplitude, the former being particularly undesired due to the loss of perfect nulling; therefore, different models use a different degree of representation of the errors, depending on the required degree of precision. In the following analysis, in parallel to the discussion addressed in Section 2.4, the external disturbances are addressed in the way they modify the ideal beahviour.

4.2 Instrumental stellar leakage

Following the classification proposed by Defrère[25],[72], the errors introduced in Section 4.1 can be grouped into errors that, in general, are affecting the optics of the system and thus are extractable or imposable during the design phase.

Recalling Figure 3.7, in fact, beyond the physical presence of geometric leakage, when perturbing the signal, both first-order effects (shown in Figure 3.7b) and second-order perturbations, which lead to a null floor perturbation (as in Figure 3.7c), arise. It is clear that second-order effects are particularly nefarious, since they can lead to highly undesired losses in the null depth level, creating a higher instrumental leakage.

An approximate description can be provided in this sense: by considering a general expression of the signal (as seen in Equation 3.6) and introducing perturbations on the phase and on the amplitude, one finds

$$V_k = A_k(1 + \delta A_k)e^{i(\varphi_k + \delta\varphi_k)}. \tag{4.1}$$

This formulation is consistent with the simplifications needed to reach the approximate expressions provided by Defrère[25] as proved in Appendix A.2. In particular, this expression summarises the second-order error terms which affect the central nulling term $R(0,0)$ as a function of the amplitude and phase fluctuations. In fact the central nulling is obtained by a combination of specific phases and combination terms (which essentially modify the amplitudes by scaling them through the use of optical transmission lines) which physically reduce the residual terms (the mathematical small-o term in the Taylor's expansion): the larger the entity of the error, the smaller the nulling will be.

4.2.1 Complete response to systematic errors

The approach represented in Equation 4.1 suffers from the lack of information in the definition of the sensitivity terms δA_k and $\delta\varphi_k$. A more refined approach involves the use of partial derivatives in the consideration of the different sources of errors.

In general, the complete instrument response is given by the photon rate on the sensor. It has been proved by Lay[66] that, in general, the integral can be split into the sum of its contributions:

$$N = N_{\text{planet}} + N_* + N_{\text{EZ}} + N_{\text{LZ}} + N_{\text{stray}} + N_{\text{thermal}}. \tag{4.2}$$

4.2.2 Planet and star signal

The signal incoming from the planet can be represented as a point source which emits a flux corresponding to that of the planet, which can be modelled as a blackbody emitter with a specified albedo[66], following Planck's law. The planet, in addition to its own emission, also reflects part of the stellar contribution; the mathematical emission model

depends, in general, on the radius of the exoplanet that needs to be known in advance, usually inferred from other indirect methods such as the transit method[20],[84].

For the star, a similar discussion can be produced, with the significant difference that its angular size cannot be neglected to a point source, so that the stellar contribution can be expressed as[66]

$$N_* = \sum_j^N \sum_k^N A_j A_k \cos\left(\varphi_j - \varphi_k\right) \bar{B}_{*,jk}, \tag{4.3}$$

which is the same relation shown in Equation 3.18. The stellar photon rate is affected by perturbations, both from first- and second-order contributions[68]:

$$\begin{aligned}\delta N_* = \sum_j^N \left[\frac{\partial N_*}{\partial A_j}\delta A_j + \frac{\partial N_*}{\partial \phi_j}\delta \phi_j + \frac{\partial N_*}{\partial x_j}\delta x_j + \frac{\partial N_*}{\partial y_j}\delta y_j\right] + \\ + \sum_k^N \sum_j^N \left[\frac{1}{2}\frac{\partial^2 N_*}{\partial A_j \partial A_k}\delta A_j \delta A_k + \frac{\partial^2 N_*}{\partial A_j \partial \phi_k}\delta A_j \delta \phi_k + \frac{1}{2}\frac{\partial^2 N_*}{\partial \phi_j \partial \phi_k}\delta \phi_j \delta \phi_k\right].\end{aligned} \tag{4.4}$$

In this equation, as well as the following ones, δA_j, $\delta \phi_j$ and similar variables are the perturbations that originate from opto-mechanical imperfections applied to the system. The sensitivity coefficients are thus obtained by partial differentiation[68]:

$$C_{A_j} = A_j \frac{\partial N_*}{\partial A_j} = 2A_j \sum_k A_k \cos(\phi_j - \phi_k) B_{*,jk} \tag{4.5}$$

$$C_{\phi_j} = \frac{\partial N_*}{\partial \phi_j} = -2A_j \sum_k A_k \sin(\phi_j - \phi_k) B_{*,jk} \tag{4.6}$$

$$C_{x_j} = \frac{\partial N_*}{\partial x_j} = 2\sum_k A_j A_k \cos(\phi_j - \phi_k) \frac{\partial B_{*,jk}}{\partial x_j} \tag{4.7}$$

$$C_{y_j} = \frac{\partial N_*}{\partial y_j} = 2\sum_k A_j A_k \cos(\phi_j - \phi_k) \frac{\partial B_{*,jk}}{\partial y_j} \tag{4.8}$$

$$C_{A_j A_k} = \frac{1}{2} A_j A_k \frac{\partial^2 N_*}{\partial A_j \partial A_k} = A_j A_k \cos(\phi_j - \phi_k) B_{*,jk} \tag{4.9}$$

$$C_{A_j A_k} = A_j \frac{\partial^2 N_*}{\partial A_j \partial \phi_k} = \begin{cases} 2A_j A_k \sin(\phi_j - \phi_k) B_{*,jk} & j \neq k \\ -2A_j \sum_l^N A_l \sin(\phi_j - \phi_l) B_{*,kl} & j = k \end{cases} \tag{4.10}$$

$$C_{\phi_j \phi_k} = \frac{\partial^2 N_*}{\partial \phi_j \partial \phi_k} = \begin{cases} -A_j A_k \cos(\phi_j - \phi_k) B_{*,jk} & j \neq k \\ A_j \sum_{l \neq j}^N A_l \cos(\phi_j - \phi_l) B_{*,jl} & j = k \end{cases}, \tag{4.11}$$

where the derivatives of the stellar brightness make use of Bessel's function algebra[23], as illustrated in Appendix A.3.1, so that, for example, for the abscissa coordinate, it results

$$\frac{\partial B_{*,jk}}{\partial x_j} = -2x_j F_* \frac{J_2\left(\frac{2\pi b_{jk} \vartheta_*}{\lambda}\right)}{b_{jk}^2}. \tag{4.12}$$

4.2.3 Exozodiacal dust

There have been many studies on the emission levels of debris discs in other stellar systems, including the analysis from VLTI from ground-based interferometry and simulation tools like the GENIE simulator[2], based on the results from multiple studied systems.

The detected photon rate is much fainter than the star one, but due to its extension, it cannot be easily nulled[25]; in this case, it is modelled by[66]

$$N_{\mathrm{EZ}} = \sum_{j}^{N} \sum_{k}^{N} A_j A_k \cos\left(\varphi_j - \varphi_k\right) \bar{B}_{\mathrm{EZ,jk}}. \tag{4.13}$$

The partial derivatives take the same forms as those shown in Equation 4.5 and following, with the distinction of the brightness coefficient being replaced by the exozodiacal coefficient, which can be modelled following the COBE model proposed by Kelsall et al.[56], which makes use of the local zodiacal extension to estimate the exozodiacal one: the main difference with the extended star models is that it cannot be assumed as a homogeneous disc[87].

4.2.4 Local zodiacal dust

The local zodiacal emission has been studied by the COBE mission and implemented into a known model that follows symmetrical behaviour along the ecliptic plane[21]. As also anticipated in Section 2.4, its emissions become stronger the closer the field of view is to the Sun-facing direction; therefore, observations in the anti-Sun direction are highly preferred[20],[25].

In this case, the photon rate, due to the fact that this is an incoherent source (due to its extended size, therefore not producing interference and perceived as uniform noise[87]), simplifies to an expression that depends on the effective solid angle of the collector[66]

$$N_{\mathrm{LZ}} = B_{\mathrm{LZ}} \sum_{j}^{N} A_j^2 \Delta\Omega_j, \tag{4.14}$$

so that a partial derivation can be performed as before:

$$\delta N_{\mathrm{LZ}} = \sum_{j}^{N} C_{Aj}^{\mathrm{LZ}} \delta A_j, \qquad \text{where} \qquad C_{Aj}^{\mathrm{LZ}} = 2 A_j^2 \delta A_j \Delta\Omega_j. \tag{4.15}$$

4.2.5 Summary of Sensitivity Coefficients

The models to compute the partial derivatives coefficients, which themselves depend on the system under analysis, can be easily implemented[68], allowing for some considerations on their values. Table 4.1 provides a summary of the parameters that have been considered for the computation of the coefficients, using the relations and implemented models in the respective sections under the implementation provided by Lay[66].

Table 4.2 provides an example of coefficients as found from data reported in Table 4.1, showing a high consistency with the results presented by Lay[66]. What is clearly shown here is that the results demonstrate—as expected—a strong sensitivity to the stellar signal, which is larger by many orders of magnitude compared to the second most significant value, the local zodiacal dust.

As anticipated, the results show little impact from the exozodiacal dust, probably due to its low emission levels, while both the amplitudes and the phases play an important

Parameter	Value
Distance to the system	15 pc
Star radius	$R_\odot$
Star temperature	$T_\odot$
Planet radius	$R_\oplus$
Planet temperature	$T_\oplus$
Planet angular separation	50 mas
Array	10.5 m linear with manually defined phases
Phases	$\begin{bmatrix} 3\pi/2 & \pi & \pi/2 & 0 \end{bmatrix}$

Table 4.1: Summary of the parameters considered under the analysis of the coefficients, selected from a combination of example computations by Lay[66] and here considered arrays from Table 3.1. The values given are taken from an example target and are given only for general description of the analysis procedure.

role, especially in the second order, where the sensitivity coefficients are particularly large, proving that even small displacements can induce large errors in the system.

As a further example of the variation of the elements, Table 4.3 includes the same results (except for the local zodiacal contribution, which does not depend on the phase as per the shown relations) with an optimisation performed using the SVD, as described in Section 3.4. The optimisation of the phase renders the first-order variation in the phase completely null (and the same occurs for the second-order aperture and phase perturbation), while leaving the second-order contribution for the apertures and phases slightly increased with larger magnitudes.

4.3 Phase Sensitivity of the Interferometer

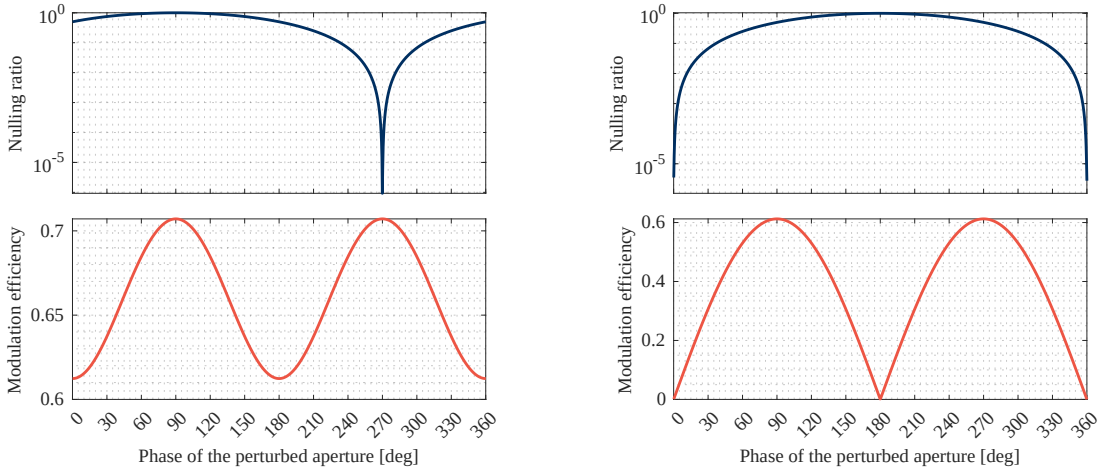

(a) Lay's Linear Array A (optimised). **(b)** Linear Array with SVD (unoptimised).

Figure 4.1: Value of the nulling ratio and the modulation efficiency by changing the imposed phase value of a single aperture, both for Lay's First Linear Array[65] and the generic Linear Array with SVD optimised phases. In Lay's array, the best nulling ratio and modulation efficiency are coincident, while in the SVD array the two metrics are opposed.

The role of the phase in acquiring the best nulling capabilities from the interferometer has been discussed in Chapter 3; however, it is interesting to see how the phase actually significantly modifies the behaviour of the interferometer in relation to other parameters.

	1st order				2nd order											
N	**Ap.**	φ	**x**	**y**	**Apertures**				**Aperture and phase**				**Phases**			
Star				Ap.	1	2	3	4	1	2	3	4	1	2	3	4
1	5.79	-12	1.65	0	235200	0	-235197	0	-12	470399	0	-470387	235197	0	-235197	0
2	5.79	0	1.65	0	0	235200	0	-235197	-470399	0	470399	0	0	235197	0	-235197
3	5.79	0	-1.65	0	-235197	0	235200	0	0	-470399	0	470399	-235197	0	235197	0
4	5.79	12	-1.65	0	0	-235197	0	235200	470387	0	-470399	12	0	-235197	0	235197
Exozodiacal disc				Ap.	1	2	3	4	1	2	3	4	1	2	3	4
1	12	0.24	0	0	6.18	0	-0.13	0	0.24	0.12	0	-0.35	0.13	0	-0.13	0
2	12	0	0	0	0	6.18	0	-0.13	-0.12	0	0.12	0	0	0.13	0	-0.13
3	12	0	0	0	-0.13	0	6.18	0	0	-0.12	0	0.12	-0.13	0	0.13	0
4	12	-0.24	0	0	0	-0.13	0	6.18	0.35	0	-0.12	-0.24	0	-0.13	0	0.13
Local zodiacal disc																
1	39															
2	39															
3	39															
4	39															

Table 4.2: Example of adimensional sensitivity coefficients resulting from data in Table 4.1.

	1st order				2nd order											
Ap.	**Ap.**	**φ**	**Pos. x**	**Pos. y**	**Apertures**				**Ap. & ph.**				**Phases**			
Star				Ap.	1	2	3	4	1	2	3	4	1	2	3	4
1	8.69	0	1.65	0	235200	-235199	235197	-235193	0	0	0	0	235196	-235199	235197	-235193
2	-2.9	0	-1.65	0	-235199	235200	-235199	235197	0	0	0	0	-235199	235201	-235199	235197
3	-2.9	0	1.65	0	235197	-235199	235200	-235199	0	0	0	0	235197	-235199	235201	-235199
4	8.69	0	-1.65	0	-235193	235197	-235199	235200	0	0	0	0	-235193	235197	-235199	235196
Exozodiacal disc				Ap.	1	2	3	4	1	2	3	4	1	2	3	4
1	12	0	0	0	6.18	-0.06	0.13	-0.18	0	0	0	0	0.11	-0.06	0.13	-0.18
2	12	0	0	0	-0.06	6.18	-0.06	0.13	0	0	0	0	-0.06	-0.01	-0.06	0.13
3	12	0	0	0	0.13	-0.06	6.18	-0.06	0	0	0	0	0.13	-0.06	-0.01	-0.06
4	12	0	0	0	-0.18	0.13	-0.06	6.18	0	0	0	0	-0.18	0.13	-0.06	0.11

Table 4.3: Extract of sensitivity coefficients resulting from data in Table 4.1, except the phases that have been optimised with the SVD analysis. The local zodiacal contribution has been omitted since its computation does not depend on the phase values and it is therefore the same as in Table 4.2.

In order to visualise the impact of a mismatched phase on the system, two performance indexes, the nulling ratio and modulation efficiency, have been computed for different imposed phase values on the first aperture (in order to keep the problem one-dimensional). As will be discussed below, in Section 4.4 and following, the role of perturbed phases is significant in the analysis; therefore, acquiring knowledge of its impact is fundamental. Therefore, by keeping the same values of imposed phases for every aperture except the first, that has been made variable, the two metrics have been collected in a plot.

Figure 4.1 visualises two different situations. Let us initially focus on the case in Figure 4.1a, which represents the changing behaviour of Lay's Linear Array seen in the comparison Table 3.5. In the nominal position (270°), the optimal situation is represented, as the nulling ratio is at its minimum and the modulation efficiency is at its maximum, thereby confirming the ideality of the situation.

By leaving the nominal configuration, the situation gets progressively worse up to the point where, around 90°, the interferometer becomes constructive; the modulation efficiency instead oscillates in a smaller range, having, at 90°, another peak.

A totally different situation is instead reported in Figure 4.1b, which has been computed using the data of the generic Linear Array from Table 3.1 and Table 3.2. The nominal configuration, being 0°, corresponds effectively to the best nulling ratio (as the nominal value is the result of the SVD analysis), yet the modulation efficiency is also minimum (and effectively zero). Whilst in this case the possible worst condition is unique (at 180°), there is no point at which both nulling ratio and modulation efficiency are at their best.

This implies, therefore, a strong ambivalence in terms of the optimisation of the phase but also of the array itself. The two figures display two completely different situations, and it is clear that focusing on obtaining the best possible nulling ratio is not sufficient, as both metrics contribute to the detection strategy of interferometry.

4.4 Role of optical path distance in sensitivity

In Section 3.7, a general relation for the nulling ratio has been derived in Equation 3.20, where the main factors that play a role in the definition of the value are the phases associated with the apertures. Indeed, as the discussion within this chapter has shown, there are many sources that can, in multiple ways, induce perturbations on these values, departing significantly from the ideal results that have been extrapolated in Chapter 3.

Therefore, it is of particular interest to evaluate the significance associated with the perturbations of the phases, or, in the same way, the optical path differences between the different branches. Indeed, by definition, it is possible to link the phase to the optical path Λ[2],

$$\varphi = 2\pi \frac{\Lambda}{\lambda}, \tag{4.16}$$

where the optical path difference (OPD) is the difference between the optical paths of the different branches and the nominal one. Given its close relation to the phase, it is clear that, at least for what concerns the nulling ratio computations, its behaviour is periodic, and it can be easily seen that the period associated with the nulling ratio is the wavelength, as proved in Appendix A.3.

Furthermore, when considering more than two apertures, different possible combinations can be performed between different branches: in effect, depending on the nominal phases that have been assigned, different behaviours may arise. To simplify the discussion, the most common case of the Double Bracewell Combination design will be considered, and in

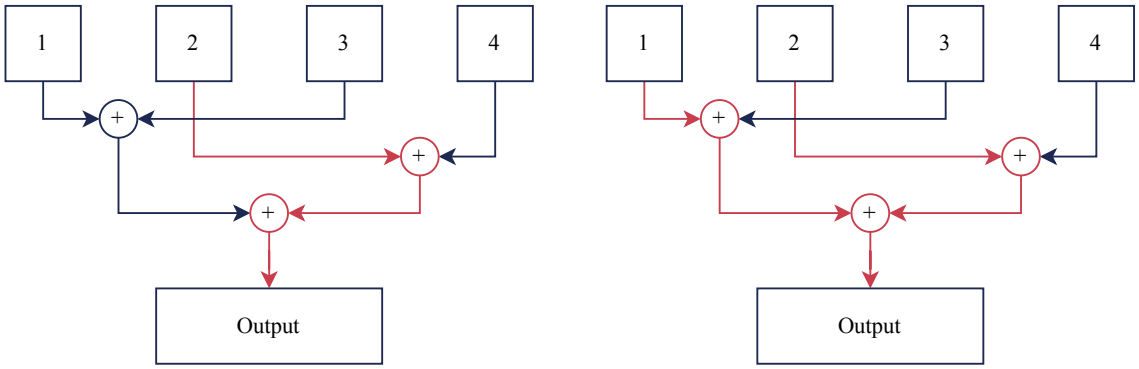

(a) Single branch perturbation. **(b)** Double branch perturbation.

Figure 4.2: Schematic representation of the considered cases within a DCB setup following the presented analysis for the X-Array seen in Section 3.1 using the reported phases from Table 3.2. The red lines represent the perturbed elements in the analysis.

particular, the two situations reported in Figure 4.2: this combination design involves a two steps process where, in the former, separate branches are summed in pair and, in the latter, the two resulting signals are merged; to consider all the possible situations, then, in a first case (Figure 4.2a) only a single aperture is perturbed, while in the second case (Figure 4.2b) two different apertures, on two different branches, have been perturbed.

As highlighted, particular importance is given to the quantification of the error, represented with the metric of the nulling ratio, due to the reported OPD on the single branch (as in Figure 4.2a) or on the double branch (as in Figure 4.2b). These two combinations actually cover all the possible situations, given the symmetric phase assignment from Table 3.2; in other hypothetical situations where the phases are not multiples of π and are all different (like in the case of the multiple Lay's arrays comparison in Table 3.5), other cases arise but may be of minor importance with respect to the considerations here addressed.

Due to the similarity of the results among the two considered arrays, in the following sections only the case of the X-Array will be presented for the analysis, yet the considerations produced for the former are valid also for the case of the Linear Array.

4.4.1 Single branch perturbation

In this analysis, to the designated phase, required to obtain the nulling behaviour, a single aperture is perturbed with the addition of a disturbance phase due to the presence of a non-zero OPD.

Let us consider a single period, that is injecting specific values for the OPD from nanometric values up to the maximum value that corresponds to the wavelength itself (which is the period, as proved in Appendix A.3). For a specific wavelength, if one were to plot the obtained nulling ratio (using Equation 3.20), the results shown in Figure 4.3a would be obtained.

The graph shows what was to be expected, that is that there is a minimum nulling ratio, corresponding to the ideal geometric leakage shown in Table 3.4, below which it is not possible to go, and the added OPD, being so small, does not produce any variation that can be established from the drawing alone, producing a straight line up to values around 10 pm. Around that value, the nulling ratio starts to increase, indicating a deteriorating situation, which reaches the maximum value (1, that is essentially that the nulling interferometer has become a constructive interferometer) and later, due to the periodic behaviour, starts decreasing again up to again the value of the ideal geometric leakage in correspondence

with the wavelength value.

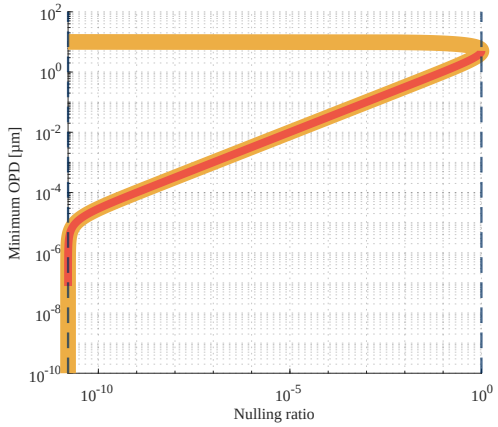

(a) Obtainable OPD for every nulling ratio at a single wavelength of 10 µm.

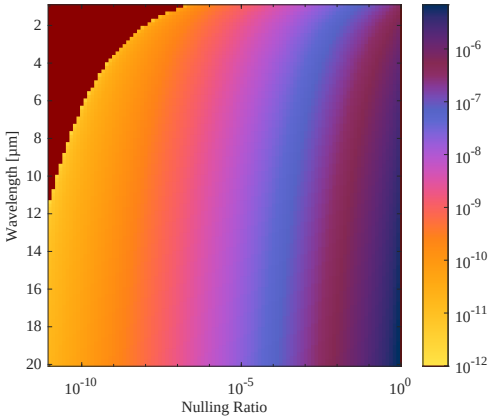

(b) Obtainable OPD for every nulling ratio on a range of wavelengths.

Figure 4.3: On the left: at the fixed wavelength of 10 µm, the curve representing the corresponding OPD to produce in order to have a specified nulling ratio is limited to half-period (red-thin curve) and inverted, in order to produce the plot on the right, where the same result is produced for multiple wavelengths. In the colour-map, the dark red tone represents an impossible situation (no OPD, not even null values, is able to grant these values).

It is therefore important to keep the misplacements of optical elements as small as possible, as they will significantly reduce the nulling power of the interferometer, in addition to the external factors that will be analysed below.

It is also interesting to observe how the curve shown in Figure 4.3a changes in relation to the wavelength: this situation is represented in Figure 4.3b. A strong dark-red region is increasing by reducing the wavelength: this region indicates that such values of nulling ratios are not achievable even under the ideal geometric leakage considerations. This becomes particularly evident as 1 µm. Not only that, but the minimum scale-value colour region extends more towards the right, indicating that even to grant such small relatively high nulling ratios, such as 10^{-5}, the OPD should be limited to nanometric values, as opposed to the case of 20 µm where 10^{-5} is reached with OPDs around 0.1 µm: the larger the wavelength, the better its resilience to large OPDs becomes (as clearly shown in Equation 4.16).

4.4.2 Double branch perturbation

If now the situation for the perturbation of two different branches is evaluated (so the situation reported in Figure 4.2b), one would find the situation reported in Figure 4.4. Effectively, the situation is coherent with the one reported in Figure 4.3b, displaying a symmetry around the bisector of the I quadrant. Even more importantly, it can be noticed that along the values of the bisector itself, the nulling ratio is always optimised since, in the last combination, what occurs is that the same OPDs actually cause a simple constant shift that is cancelled out. Apart from these considerations, the results are in line with the expectations, that is the smaller the wavelength, the more problematic it becomes to keep the system under acceptable tolerances, beyond the fact that smaller wavelengths cannot reach smaller values of nulling ratios.

To see the behaviour for different wavelengths, it is sufficient to select a specific point on the maps from Figure 4.4, such that, clearly, it is below the interval of considered wavelengths in order not to see any repeating periods: for this scope, the arbitrary point at 0.2 µm along

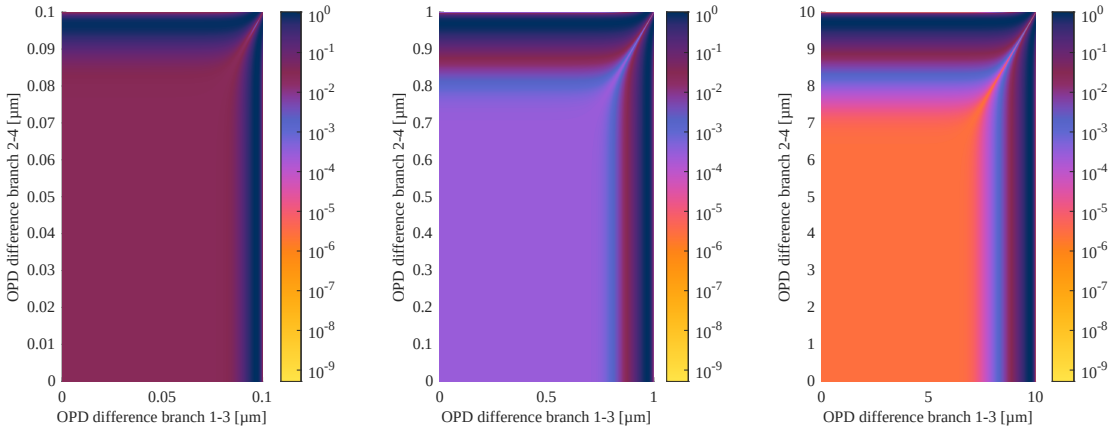

(a) $\lambda = 0.1\,\mu m$ **(b)** $\lambda = 1\,\mu m$ **(c)** $\lambda = 10\,\mu m$

Figure 4.4: Achievable nulling ratios for imposed OPDs along the two branches as referenced in Figure 4.2b for three different wavelengths. The three figures share the same colour-map for references, but the axes have different limits to avoid incurring in the periodic repetition.

branches 1-3 and 0.1 µm along branches 2-4 has been selected. The results are presented in Figure 4.5, with the nulling ratio exhibiting a logarithmic trend with respect to the wavelength. Effectively, the result is coherent with Equation 3.20, where essentially, when everything but the wavelength is fixed, the factor $1/\lambda$ appears both in the Bessel function's argument and the cosine (under the OPD replacement from Equation 4.16), making this behaviour coherent with expectations.

4.5 Sensitivity to optical perturbations

The analysis that have been presented up to this point was focused on the definition and the possible consequences of perturbations on the system. The remaining part of this chapter, instead, revolves around the presentation of possible expected values derived from an optical modelling software, CODE V,[100] and which consequent considerations can be made for the model considered in this work.

The process hereinafter described, then, considers the setting up of the simulations and the extraction of outputs from the software, followed by the consequent considerations that can be made on the results concerning the development process. The process illustrated in this section is a summary of the simulations proposed in accordance with Carboni[13], which are, in turn, an evolution of the process developed by Viseur[72].

4.5.1 Optical modelling system

While the manipulations of the outputs of the simulations have been implemented on a specific system, they ought to be as general as possible and therefore, given the main focus of this work, the analysis on the optical modelling will be strongly summarised.

The process, illustrated in details by Carboni in their master thesis[13], has involved the modelling of an optical system, initially under ideal and perfect conditions. Initial points for the design were the mono-chromaticity of the system and the magnification, as well as other mechanical considerations that lead to the fixing of one focal length. The initial values were chosen based on common figures found in other similar concepts[25],[17],[72] and in order for the resulting system to be hypothetically launched by the Ariane 6 launcher[5].

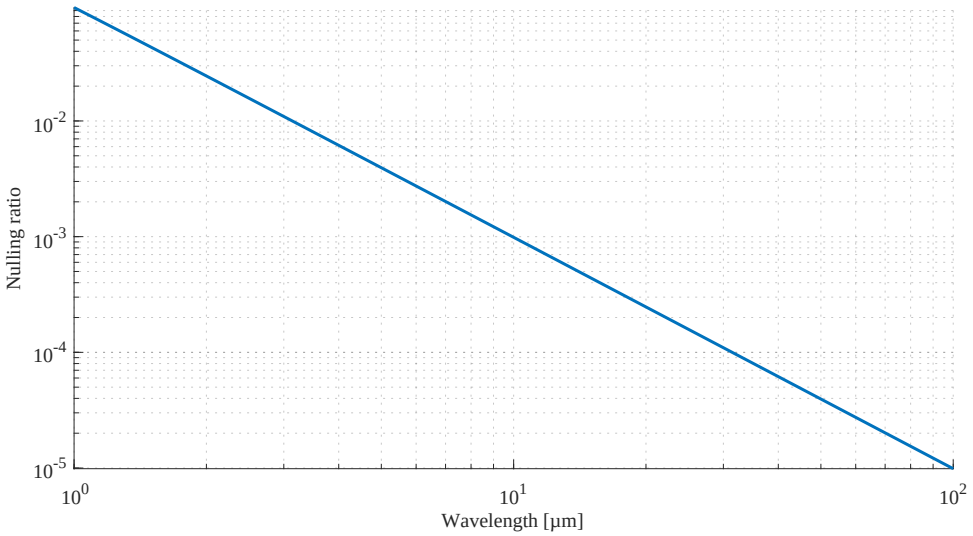

Figure 4.5: Variation of the achievable nulling ratio for a specific OPD point (0.2 µm along branches 1-3 and 0.1 µm along branches 2-4) for different wavelengths.

In summary, the nominal system for a single branch is shown in Figure 4.6 and involves a confocal system with two parabolic mirrors and a tip/tilt mirror. Even if it is not part of the sensitivity analysis, the delay line is part of every branch as illustrated in the general elements of an interferometer. It can be noticed that the system, as is, is afocal, meaning that the image plane is only virtual and is not located at the convergence of rays.

Once the system has been implemented in the optical modelling software CODE V[100], a macro instruction script has been developed (upon a codebase derived from the work of Viseur[72]), to randomly perturb the system and subsequentially register the outputs in terms of optical paths of displaced incoming rays. The macro, implemented using the MACRO-PLUS scripting capabilities[101] within CODE V[100] performed a predetermined and user defined N_S number of simulations where:

1. Each optical element of the system (first, second and tip/tilt mirrors) is modified, in terms of position, rotation and wavefront deformations by a random amount, which is taken from a normal Gaussian distribution and found within a maximum tolerance limit that has been user defined.
2. The ray propagation is computed: a single ray, incoming perfectly straight, is displaced around N_P equally-spaced positions that simulate the full aperture of the system and the propagated up to the image plane. In practice, this means that, starting from an aperture of 2.5 m^2, N_P points are defined to cover equally the entire surface.
3. For each of the N_P displaced rays and for each of the N_S simulations, the optical path and the x, y coordinates on the afocused image plane are registered in an output file that can later be manipulated within other programming languages.

4.5.2 Nominal system results

At this point, then, a distinction must be taken between the ideal system (the one that has been considered in Chapter 3) and the nominal system: the former, originated by a perfect optical system, is such that every one of the N_P displaced points undergoes the same optical path (displaced accordingly), so that, in summary, the OPD for each point is exactly null. The same, however, cannot be said for every nominal system. While

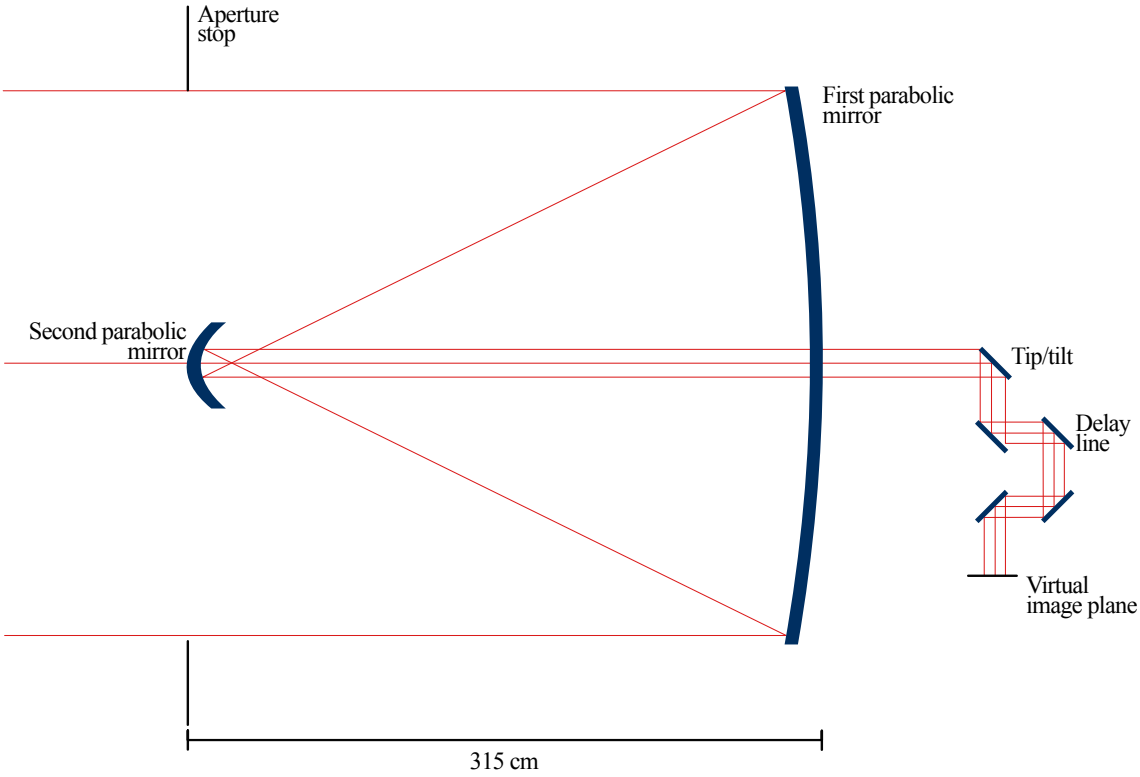

Figure 4.6: Simplified representation of the optical system modelled by Carboni in the analysis described in Section 4.5.1[13].

some design choices might reduce or make such differences negligible, given the desire to make the analysis valid for any system, those included results must be taken into account. They are not the results of optical displacements but just to the way the optical system is designed and, as a consequence, are always present.

Figure 4.7 shows both the resulting optical path difference and converted phase (always using the already discussed Equation 4.16) for one nominal system, computed considering 49077 points (the result of having each ray spaced by 1 cm on the aperture stop plane).

As expected, given the absence of any perturbations, the resulting OPDs are relatively small, around two order of magnitude below the wavelength. It is clear, however, that, if the wavelength had been within the visible range, then such values of OPDs would have been completely dominant over the entire processes, as recalled in the OPD sensitivity section.

Even with such small values of OPD, the resulting phase is oscillating between 2 and -12°. Furthermore, it can be noticed that the null region (i.e. the region closer to null OPD, computed with respect to the central point of the initially defined distribution) is perfectly centred, as expected for a symmetric distribution of random errors.

4.5.3 Perturbed system results

In order to verify the model and the sensitivity of the considered systems to the optical displacements, 100 simulations over 49077 points have been performed using the data reported in Table 4.4. To show the extents of such simulations, the results for the first two of them, both in terms of OPDs and phases, have been reported in Figure 4.8.

As expected, the perturbations are way larger than the one seen in Figure 4.7, reaching

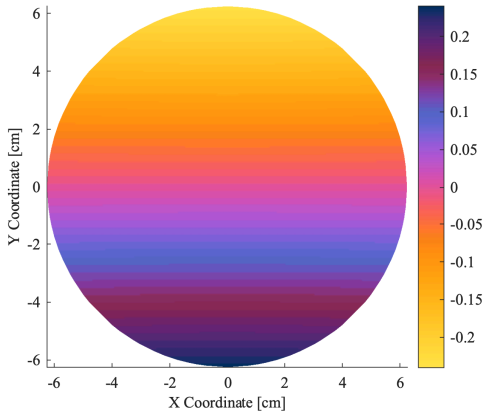

(a) OPD [µm].

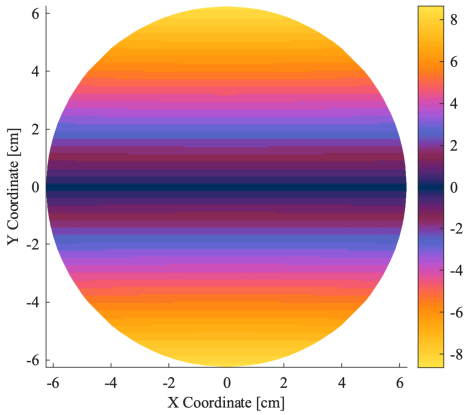

(b) Phase [deg].

Figure 4.7: Optical path difference and phase over the pupil plane for the nominal system considered in Section 4.5.1, generated considering a single simulation of 49077 points.

Parameter	Value
Number of simulations N_S	100
Number of displaced rays N_P	49077
Standard deviation for linear displacements [µm]	0.15
Standard deviation for thicknesses [µm]	0.3
Standard deviation for angular displacements [mas]	1.8

Table 4.4: Parameters used in the generation of the simulations considered in the following analysis.

values as large as around 1 µm (as opposed to nominal max value of 0.2 µm), being around one order of magnitude below the wavelength itself. Beside that, the "horizontal" trend that could be observed in the nominal response has been overwritten by a "randomly" oriented trend which however keeps showing a symmetry line, which could, for example, indicate that the perturbations along the constant axis (i.e. the one that is not the symmetry axis) may be less significant with respect to the ones on the other one.

Similar considerations can be made for the phases, that, being within the limit of half the wavelength, is the result of a bijective non linear map for every point. The same results apply as well for the remaining, non shown simulations.

Eventually, for a global comprehension of the results of the simulations carried out within the optical design software, Figure 4.9 provides statistical representations for all the N_S simulations.

In particular, Figure 4.9a represents the probability density of the resulting OPD: the peak of the histogram is around zero, which, as expected, confirms that, if the errors applied to the system are symmetric and centred, the same occurs to the resulting OPDs. However, it can be observed that:

- The histogram exceeds the height of the Gaussian fit in the centre (it is a leptokurtic distribution), which indicates, in general, a good resistance to the errors;
- In the same way, the tails decay faster than the fitted Gaussian, meaning that extreme values are less frequent than in a normal distribution, meaning that the system rejects larger OPDs.

The same conclusions can be found in Figure 4.9b, which displays the comparison between

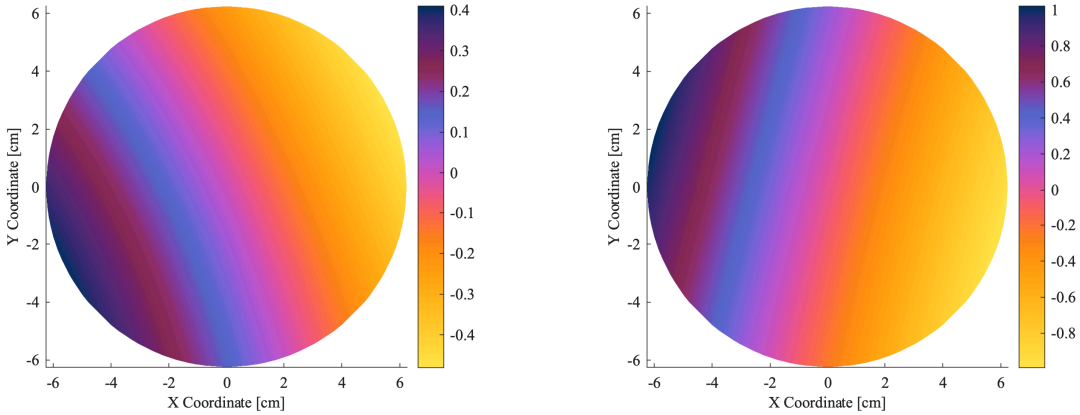

(a) OPD [µm] for simulation 1.

(b) OPD [µm] for simulation 2.

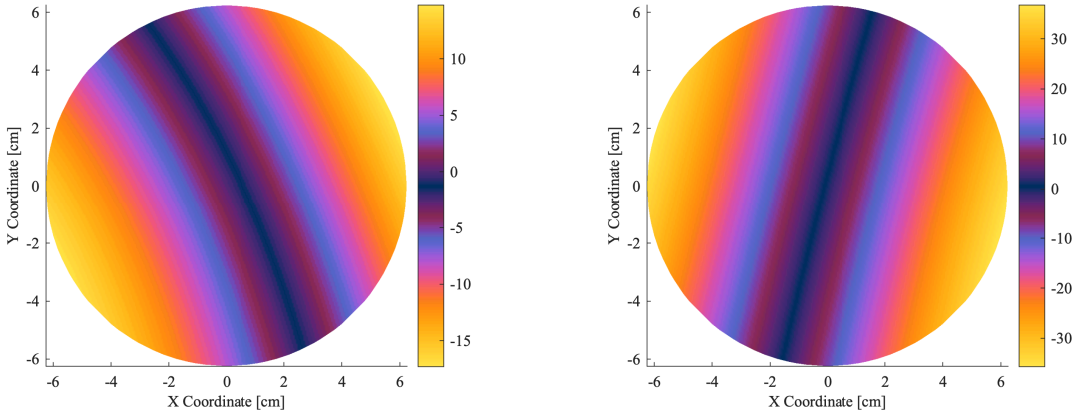

(c) Phase [deg] for simulation 1.

(d) Phase [deg] for simulation 2.

Figure 4.8: Optical path difference and phase over the pupil plane for two (arbitrary chosen) simulations of a perturbed system considered in Section 4.5.1, generated considering a 100 simulations of 49077 points.

the root-mean-square values of each simulations and the standard deviation of the fitted distribution: the graph shows that all points lie close to the identity line, meaning that the RMS and the STD are in agreement.

As a conclusion, it is possible to say that the system is mostly linear, especially close to small error region, however, there are outliers and mismatches that indicates the presence of non-linear error propagations and limitations in the spread of OPD variations, meaning that, due to its complexity, the optical system does not behave completely linearly.

4.6 Conclusions

This chapter presented an overview of the main sources of perturbations that can modify the ideal results presented in Chapter 3. As for any system, those errors are systematically present and must be considered in the analysis for a correct estimation of the results provided by the interferometer, therefore they must be acknowledged before any other derivation.

An introduction to the mechanical errors that causes mismatches from the ideal case situation has been given with practical results from the simulations implemented in an optical system. As the results have shown, these errors alone (that is, limited to a single arm analysis, without considering the mismatches in the positioning of the apertures or

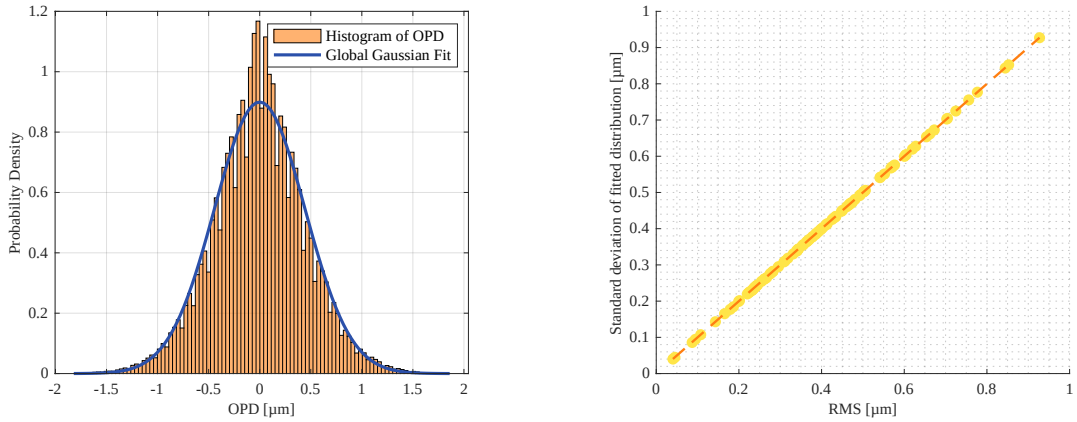

(a) Statistical distribution of OPDs.

(b) Comparison between RMS and fitted STD.

Figure 4.9: Statistical analysis of the resulting ensemble of simulations from CODE V[100],[13], both in terms of probability density and comparison between the RMS of the ensemble and the STD of the fitted curves.

the combinations) already introduce an error that exceed 30° on the phase, which can ultimately be already highly detrimental on the nulling results.

For this reason, the following chapter will analyse the results that such perturbations introduce within the system and possible strategies to overcome them in the proceeding of the analysis.

5 Compensator impact on performances

Note:

This chapter has been co-authored with Claudia Carboni with the goal of combining the optical design analysis results with the numerical model in order to evaluate the validity of the proposed design and the improvements that the compensator provides to the system using simpler evaluation metrics.

The aim of this chapter is to show the compensator impact on the performances of the analysed four apertures nulling interferometer. The first section focuses on the logic and design of the compensator, implemented in CODE V software. In particular, the practical implementation of the compensator is presented, describing two possible tools, one based on the bisection method and one on CODE V optimisation commands. Subsequently, a comparison between the two compensators and their effect on the results are outlined.

Furthermore, a detailed interferogram analysis in presented, showing the results for a single and then multiple branch perturbation. It follows an overview of statistical analysis including the transmission maps, the point spread function and the potential exoplanet yields using the statistical tool P-POP[52].

Finally, a perturbed comparison for multiple arrays is presented. The difference with the nominal analysis is highlighted, in particular regarding the non-significant resistance to the errors by the considered arrays, making the choice of the array driven by external parameters.

5.1 Compensator logic and design

The aim of a compensator is to optimise the perturbed system in order to be as close as possible in terms of performances to the nominal configuration, guaranteeing the correct functioning of the system. In certain cases, the degradation resulting from the perturbations is minimal, however, for large telescope optics, some type of active compensation or adjustment, even if applied intermittently, is essential[98].

In reality, the compensator is represented by actuators, which compensate the perturbations by translating or rotating a target mirror and by wavefront sensors, which measure the shape or distortion of a light wavefront as it passes through or reflects from an optical system. Therefore, the final goal is to obtain an OPD as low as possible by adjusting the position of the target mirror, which in most cases is the secondary mirror[106], considering that its size is significantly smaller than the primary mirror, therefore more easily adjusted.

To complete system compensation, it is first necessary to determine the correction (or adjusting) values. Several alignment algorithms have been explored for this purpose, including the Sensitivity Table Method (STM), Merit Function Regression (MFR), and Nodal Aberration Theory (NAT). Among these, STM is the most commonly used. It relies on the sensitivity of wavefront aberrations to perturbation parameters and includes approaches such as Zernike coefficient sensitivity, RMS wavefront error sensitivity, and MTF sensitivity[106].

5.1.1 Practical implementation of the compensator

Considering the optical design presented in the previous Chapters, two possible different compensator have been developed and implemented. The first one uses the bisection method, while the second one is based on CODE V optimisation commands.

Bisection method

The block diagram presented in Figure 5.1 shows the iterative optimization process used to implement a bisecting algorithm to minimize OPD by adjusting four actuators: XDE, YDE, BDE, and ADE, respectively decentres with the respect to X, Y and tilt angles with respect to X, Y.

Firstly, the OPD is measured through a sensor in order to obtain a baseline. The process iteratively tunes a set of actuators and each actuator is perturbed independently. The actuator is displaced by a predetermined step in the current direction and the new OPD is measured after the perturbation. If the OPD measured is smaller than the initial OPD, the direction of the movement is retained, otherwise the step is halved and the movement direction is flipped.

After one complete iteration over all actuators, the algorithm checks if the step size for all actuators is less than a predefined resolution threshold and if so, the optimisation converges, otherwise the process restarts from the top. The measurement of the OPD is performed using specific sensors which provide real-time measurements of system performance.

CODE V optimisation

Figure 5.2 represents an iterative optimisation procedure for aligning an optical system, in particular taking into account mechanical tolerancing of the secondary mirror.

The process begins with initialising the system where all the optical surfaces without associated actuators are mechanically fixed, meaning their position and orientation remain constant during the optimisation. The secondary mirror is granted of 6 degrees of freedom (DOFs) which are active variables in the optimisation cycle. The internal merit function optimisation loop in CODE V is executed. This adjusts the (DOFs) of M_2 to minimise the OPD. An afocal constraint is also applied, indicating that the system should maintain a collimated beam.

Then, constraints are applied to the optimisation variables, in order to obtain real values for existing actuators[78]. In particular nanometric limits on translations, which ensures extremely fine control over mirror positioning, and arcminute limits on rotations, which restricts angular misalignment within a few arcminutes. These constraints are essential for ensuring that the solution remains physically realisable and within the capabilities of actual mechanical actuators.

After the optimisation, the final adjustments are checked against actuator resolution, ensuring the proposed movements are within the control precision of available actuat-

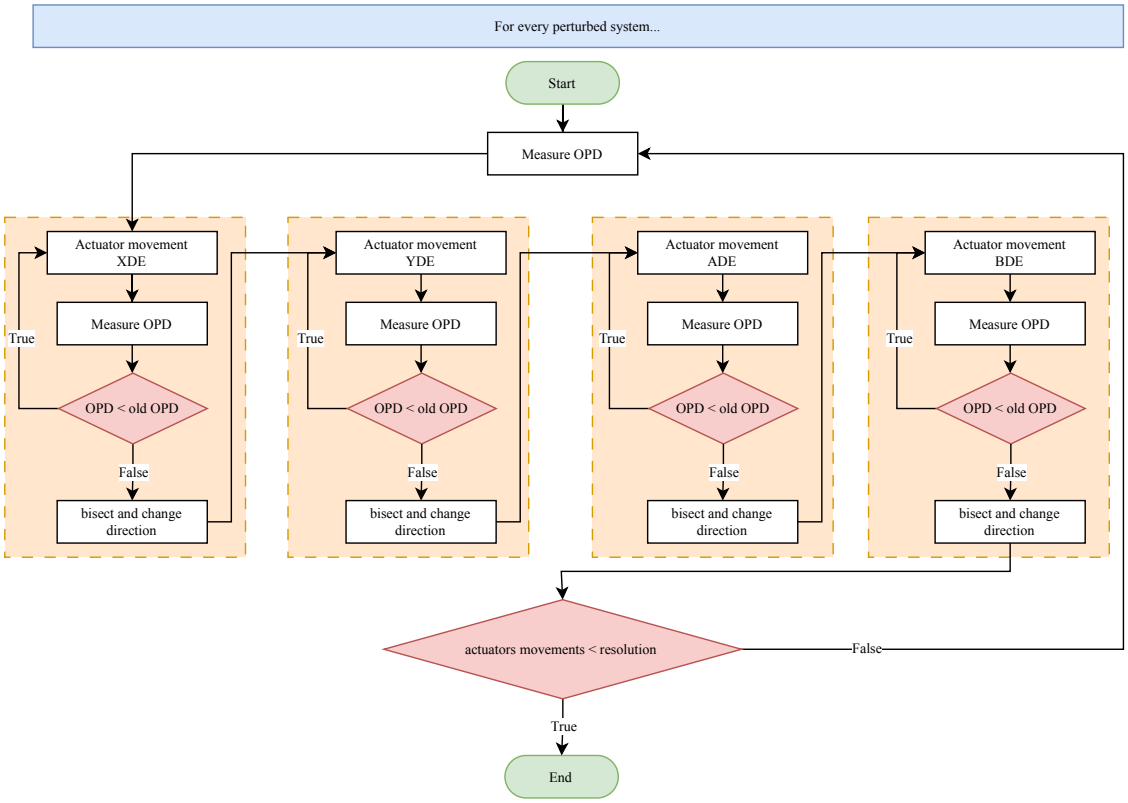

Figure 5.1: Block diagram of the closed loop feedback used to implement the compensator with the bisection method.

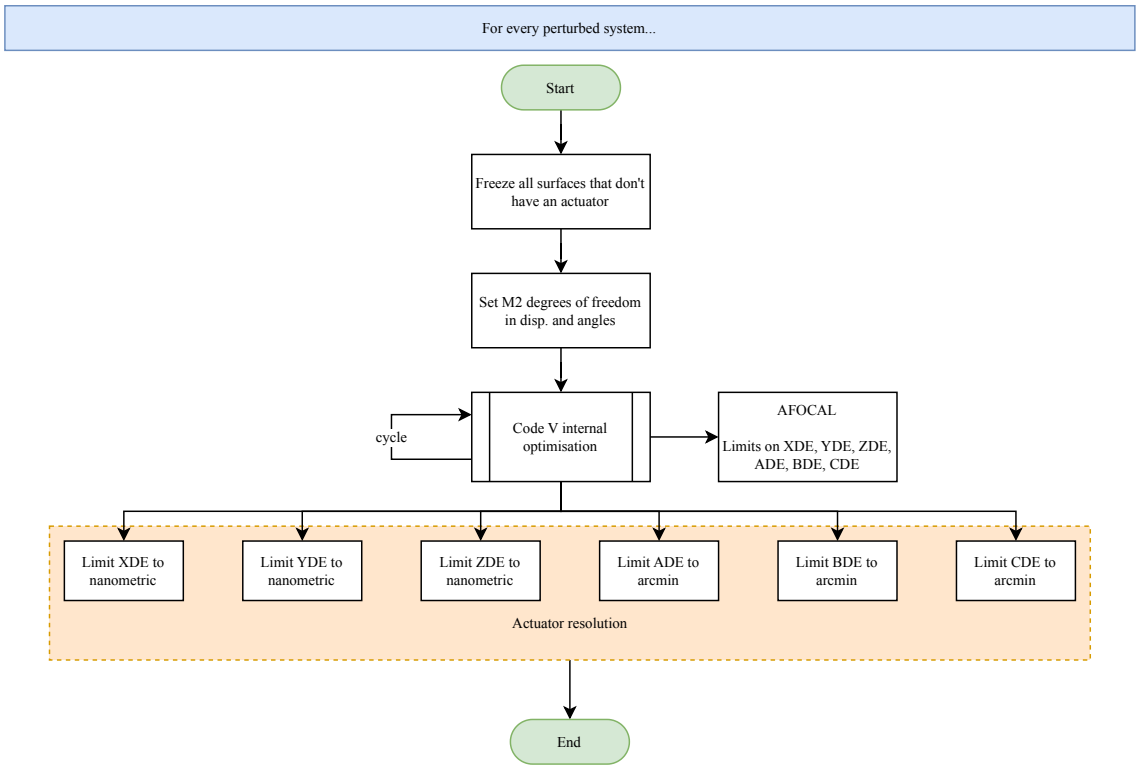

Figure 5.2: Block diagram used to implement the compensator with CODE V optimisation.

ors.

The optimisation terminates once all constraints are met and the system achieves desired performance.

5.2 Comparison of improved results with compensator

The actual potential of the two compensators has been tested on the system using two macro-PLUS programs implemented in CODE V software.

A surface deformation of $\lambda/10$, an offset of 1 µm in the X, Y and Z direction and a tilt of 9.28×10^{-4} arcmin with respect to X, Y and Z direction, for the primary mirror and 22×10^{-4} arcmin for the secondary mirror have been applied. In particular, a Monte Carlo simulations around these values has been carried out. Then the compensators are used as defined in the previous section in order to optimise the system performances.

Figure 5.3 shows the effect of the compensator implemented with the bisection method on the perturbed system, showing an improvement in the performance, since the values of the OPD are smaller, as expected.

While Figure 5.4 shows the effect of the second compensator on the perturbed system. It can be observed that the results are not in line with the expectation, since the performances get slightly worse. Therefore, only the the bisection method is valid and its positive impact on the system will be further addressed in the discussion.

Table 5.1 shows a comparison between the two compensators, where the CPU time is basically the same, while their effect on the OPD is significantly different.

		Maximum OPD [µm]	
	Elapsed time	**Perturbed**	**Corrected**
Bisection method	00:42:26	1.4039	0.7493
CODE V optimisation	00:42:52	1.2224	1.6481

Table 5.1: Comparison between the compensator with the bisection method and the the compensator with CODE V optimisation over 50 iterations and 49077 displaced rays. In particular the computational time is represented in the format HH:MM:SS and the maximum values of the optical path difference before and after the compensator effect in micrometres.

Figure 5.5 gives an overview of statistical elements of the two populations of corrected (using the bisection compensator) and uncorrected values. As it can be seen, the correction actually strongly reduce the entity of disturbances acting on the screen, hence showing once again the quality of the implemented compensator.

The same improvements are visible for different metrics in Figure 5.6: in the first graph, the nulling ratio has been computed for each N_S simulation before and after the correction. Points that lay below the unit line are then an improvement and that what happens on the vast majority of the times. There are few points that lay close to the line or immediately above: in that case, globally, the compensator is not able to significantly improve the situation.

Figure 5.6b shows instead the improvement value (normalised) for each point on the pupil screen. A fictitious value of the nulling ratio has been computed for each point and later the corrected value has been subtracted to the uncorrected one in logarithmic scale: positive points show an improvement, while negative points show a global decreasing in quality. This value is deemed to be fictitious since the pupil plane cannot actually be perceived and ultimately the general value of the nulling ratio is rather resulting from a combination

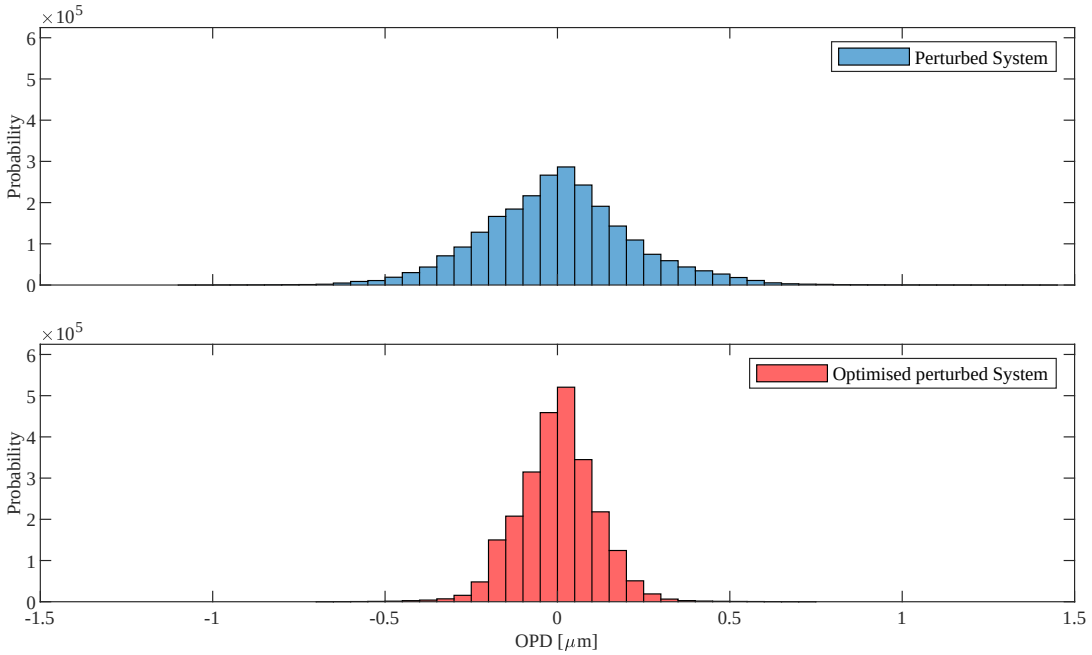

Figure 5.3: Histogram of the optical path difference of the perturbed system before and after the compensator implemented using the bisection method over 50 simulations.

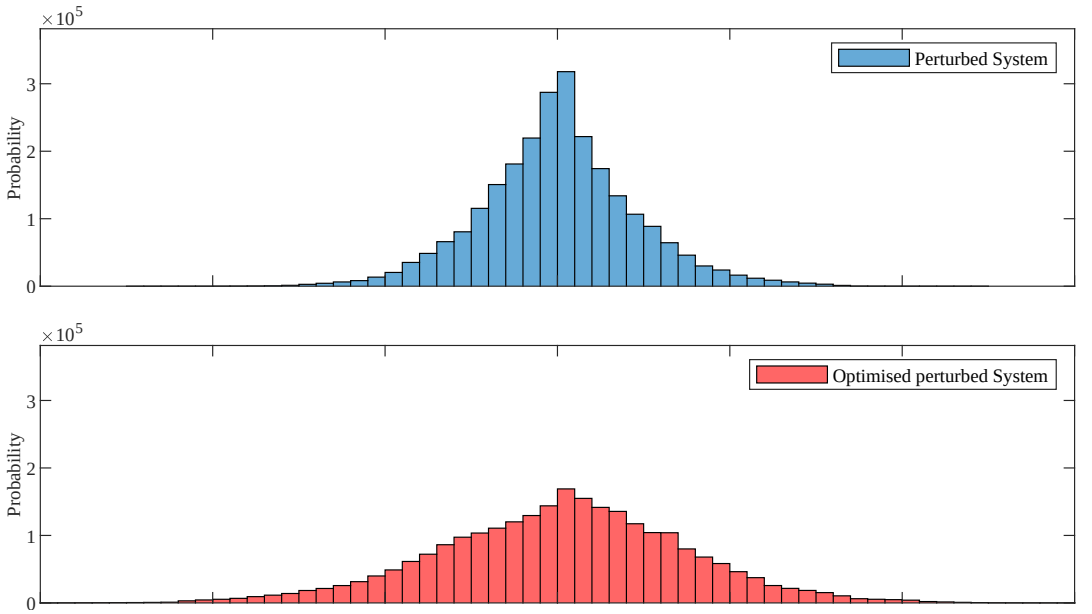

Figure 5.4: Histogram of the optical path difference of the perturbed system before and after the compensator implemented using CODE V optimisation over 50 simulations.

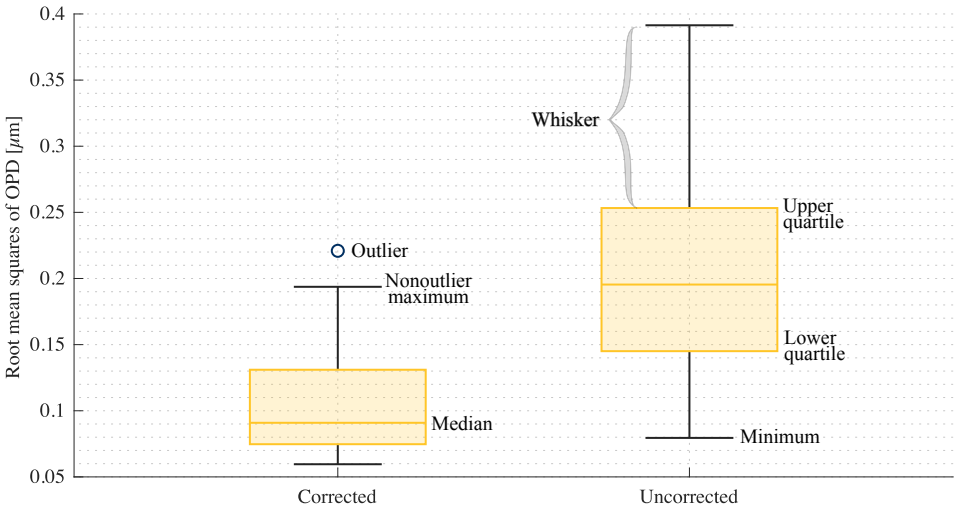

Figure 5.5: Statistical summary of the perturbed and corrected analysis (of the bisection compensator).

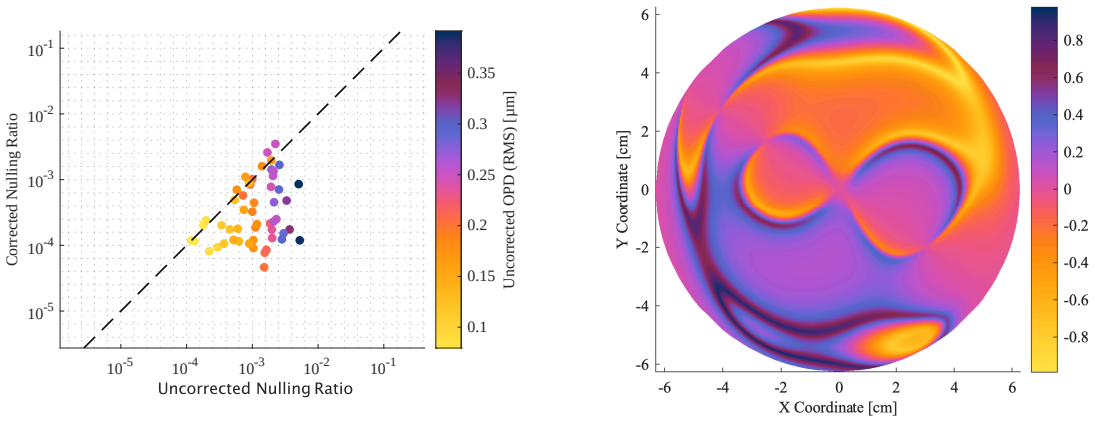

(a) Correlation of the correction

(b) Improvement scale

Figure 5.6: Improvements brought by the bisection compensator on the analysis. On the left: the resulting global nulling ratio for each simulation is plotted for the two cases. Each point that lies below the bisection line is an improvement over the unperturbed result. On the right: index of improvement of each point at the pupil screen: negative points are improved, while positive points got worse.

of all the considered values, therefore, from this point onward, the value will be referred as nulling ratio distribution.

As it can be seen, the pupil screen is mostly populated by positive values, therefore indicating a global improvement over the pupil plane, once more validating the working principle of the implemented compensator.

5.3 Interferogram analysis

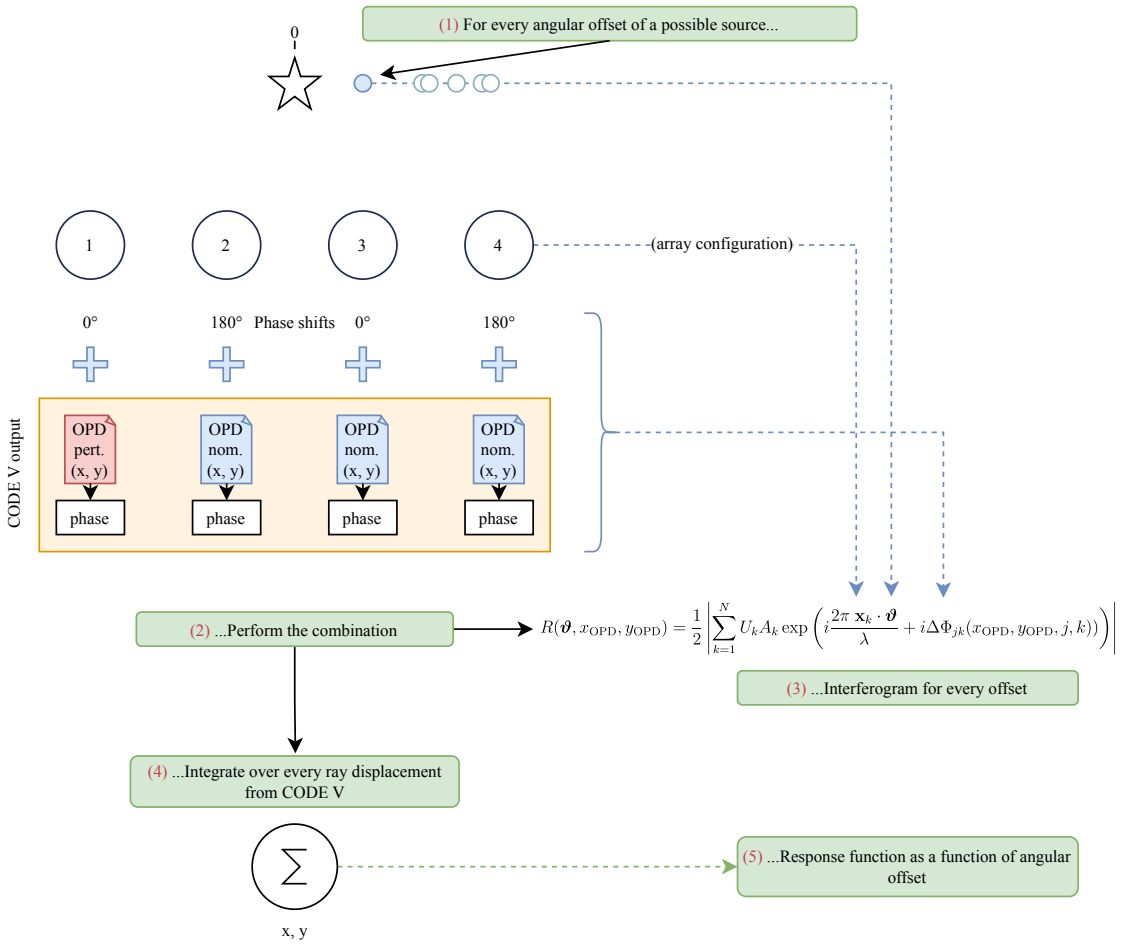

Figure 5.7: Block diagram of the algorithm used to compute the interferogram response and its integration: the response function is not computed anymore as a function of the angular position on the image screen $\boldsymbol{\vartheta}$ but as a function of the x, y coordinates on the pupil screen.

To better visualise the results of the analysis in terms of valid metrics for interferometry, a new procedure is here implemented and presented: while up to this point, most of the metrics were analysed at the image screen, that is based on angular grid position, in the sense that the response function was computed as a function of the angular position on the sky $\boldsymbol{\vartheta}$, other considerations can be made to compute the response as a function of the pupil plane coordinates $\mathbf{x}$.

Figure 5.7 illustrates the process here considered: by considering (at least initially) that all the apertures except the first display a nominal response and that the first one is subjected to one of the different simulations computed with the use of CODE V, then, while considering Equation 3.4, instead of spacing over the different angular offsets, a map is obtained by each time fixing a single value of this parameter; in this case, then, the response function R is a function of the coordinates within the pupil planes that appear

indirectly within the expression via the phase term $\Delta\Phi$:

$$R_{\boldsymbol{\vartheta}}(\mathbf{x}_{\text{pupil}}) = \frac{1}{2}\sum_{j=1}^{N} U_j \sum_{k=1}^{N} A_j A_k \cos\left(\frac{2\pi\,\boldsymbol{\vartheta}}{\lambda}(\mathbf{x}_j - \mathbf{x}_k) + \Delta\Phi_{jk}\right). \tag{5.1}$$

As a reminder, in Equation 5.1, the phase term $\Delta\Phi$ is a function of both the "nominal" phase (assigned to the designated arm j through phase retarders and optical delay lines in order to obtain the desired nulling target) and the undesired perturbance introduced by the optical system. In addition, disturbances introduced by external factors will also influence the results but are neglected in this analysis. In summary

$$\Delta\Phi_{jk} = (\Phi_j + \tilde{\varphi}_j(\mathbf{x}_{\text{pupil}}) + \tilde{\varphi}_{j,\text{external}}) - (\Phi_k + \tilde{\varphi}_k(\mathbf{x}_{\text{pupil}}) + \tilde{\varphi}_{k,\text{external}}), \tag{5.2}$$

Where, in Equation 5.2, when $j = 1$, $\tilde{\varphi}_j(\mathbf{x}_{\text{pupil}})$ comes from the perturbed simulations of CODE V; in all the other cases, it comes from the nominal results.

It is therefore possible, for every angular offset in the sky, to obtain the interferogram result for every point of the pupil screen, making use of the already developed analysis. While, in practice, a 2D array of points (since $\boldsymbol{\vartheta}$ is essentially a vector) could be used, given the symmetry of the problem, in order to simplify the analysis, in the remaining part of the section it will be assumed to swathe over linear positions of angular offsets.

Eventually, the response function for the entire sky is obtained by double integrating the maps obtained above over all the pupil coordinates:

$$RF(\boldsymbol{\vartheta}) = \iint_{\mathbf{x}_{\text{pupil}}} R_{\boldsymbol{\vartheta}}(\mathbf{x}_{\text{pupil}})\, d\mathbf{x}. \tag{5.3}$$

This method, with respect to the computation of the transmission map making use of the independent coordinate $\boldsymbol{\vartheta}$, ensures that the found result is not the result of a simple use of a single perturbed value, but every computed result from CODE V concurs to the computation of the final result.

5.3.1 Single branch perturbation

In the rest of the current section, the considerations shown above will be applied to a linear array. Very similar considerations can clearly be obtained for any other configurations; therefore, for brevity, they will not be taken into account.

As anticipated in Figure 5.7, initially, the tool is validated by perturbing a single branch, by converting the OPD resulting from the ray tracing software into a phase by the means of Equation 4.16. It is possible to investigate, over N_S simulations, N_ϑ angular offsets in the sky, leading to the necessity to compute $N_S \times N_\vartheta$ interferogram diagrams as a result.

Figure 5.8 presents, for a random simulation applied on the first branch, the resulting virtual interferogram at specific angular offsets. At first glance, the three images seem almost identical, displaying small variations on one side of the pupil plane and deformations induced by the surface deformations, with small variations in the scale from one to another.

Even if small, these variations are indeed enough to cause significant variations in the integrated function, as will be shown below. As can be noticed as well, the central point is the point having the smallest error—a consequence of the central point having no optical path difference by definition.

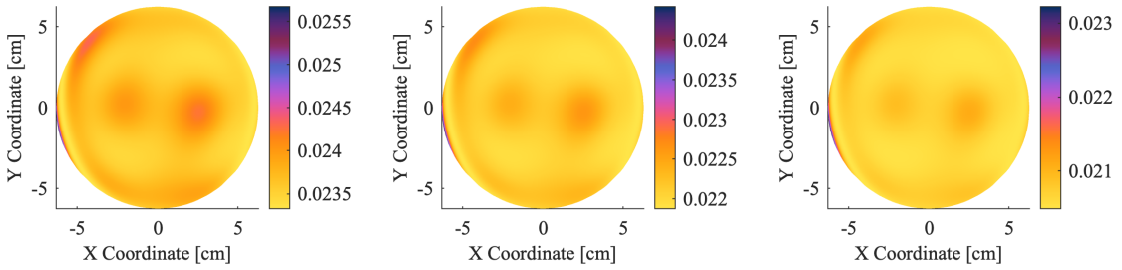

(a) -300 mas **(b)** 0 mas **(c)** 300 mas

Figure 5.8: Intensity response (in m^4) for every displaced ray of a Linear Array interferometer at pupil plane for different angular positions (where 0 mas represents the target point, i.e. the target star) on the screen. All these angular positions belong to the same simulation.

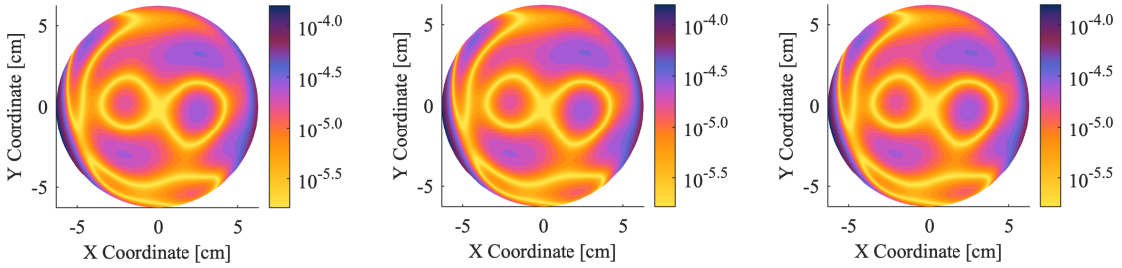

(a) 1st simulation **(b)** 2nd simulation **(c)** 3rd simulation

Figure 5.9: Nulling ratio distribution for every displaced ray of a Linear Array interferometer at pupil plane for three different random simulations from CODE V.

Very similar considerations can be found in Figure 5.9, which instead depicts the nulling ratio for each point at the pupil plane. As a theoretical reminder, the nulling ratio does not depend on the angular position used to compute the intensity response, but only on the phase combinations and therefore the different simulations, providing, as a result, N_S different pupil diagram screens. In addition to that, the value should only be taken as a reference of the "quality" of the specific point as, ultimately, only a single value of the nulling ratio will result from the integration of the pupil screen response or the analysis of the image screen (which is only a theoretical concept).

That being considered, as can clearly be seen, the results display very small changes from one simulation to another. All of them display a region which is almost perfect, with nominal behaviour, and side regions with worse results.

Once statistical results are computed for each point, the results shown in Figure 5.10 are found; it is clearly shown that, over the N_S simulations, only the central point displays an almost-perfect nulling ratio, this last result confirmed by the median and worst nulling ratios for each point. In the same way, the most displaced rays, instead, can only produce low validity nulling ratios.

As a summary of the reported information above, Figure 5.10d displays the probability of finding a "good" nulling ratio (that is, above 10^{-4}) for each specified point. Indeed, the result confirms once more that only the central point and the limited surrounding area provide such possible results. A smaller aperture would, effectively, increase, at least in relative size, the well-performing region, but it would ultimately reduce the observing power of the interferometry, as the aperture size rules the amount of light that reaches the combiner.

It is worth noticing that the compensator was able to avoid regions with non-working

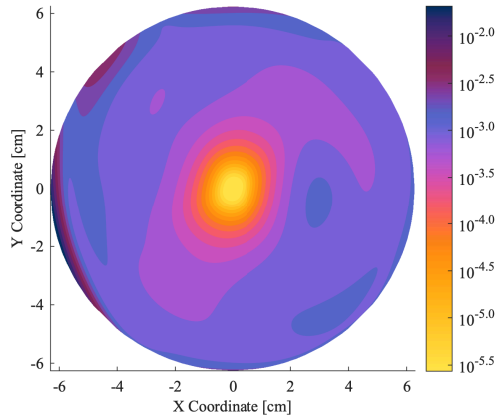

(a) Mean nulling ratio distribution

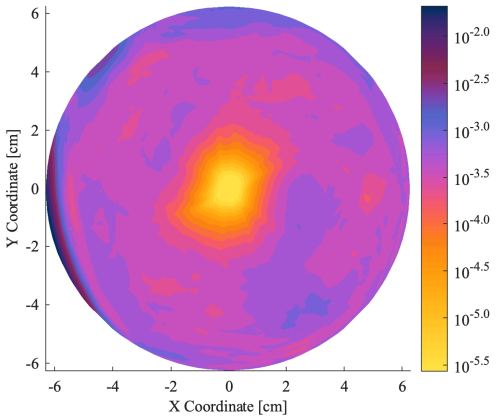

(b) Median nulling ratio distribution

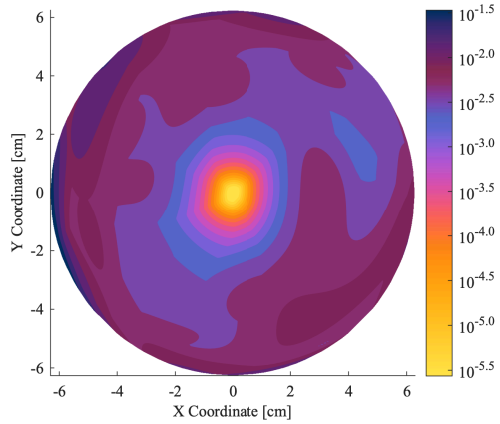

(c) Worst case nulling ratio distribution

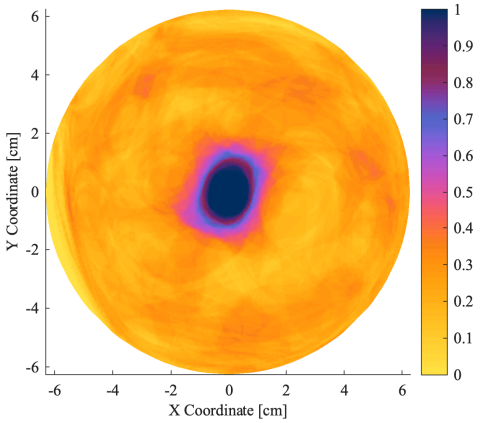

(d) Probability of high nulling ratio distribution

Figure 5.10: Statistical distributions of different performance indices for the nulling ratio distribution over every displaced ray of a Linear Array interferometer at pupil plane for all cumulative angular positions on the screen.

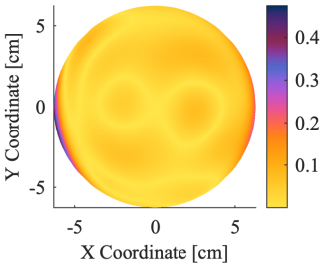

(a) 1st simulation

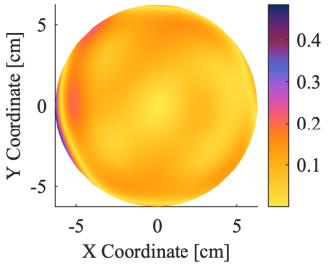

(b) 2nd simulation

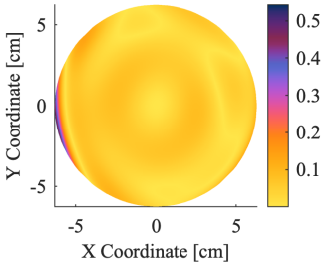

(c) 3rd simulation

Figure 5.11: Modulation efficiency for every displaced ray of a Linear Array interferometer at pupil plane for three different random simulations from CODE V.

nulling ratio; therefore, while 10^{-2} is not by any means a desirable result, its introduction allowed for a globally improved result.

The complementary metric to the nulling ratio is the modulation efficiency, shown in Figure 5.11. Once again, it does not depend on the angular position on the image screen, but only on the array size and as it can be seen it behaves like the "negative" of the nulling ratio, since it is maximum at the sides of the pupil screen. This does not allow to draw consequences on the possible position of the exoplanets, as the pupil screen cannot be measured, yet it shows once again how the deformations work.

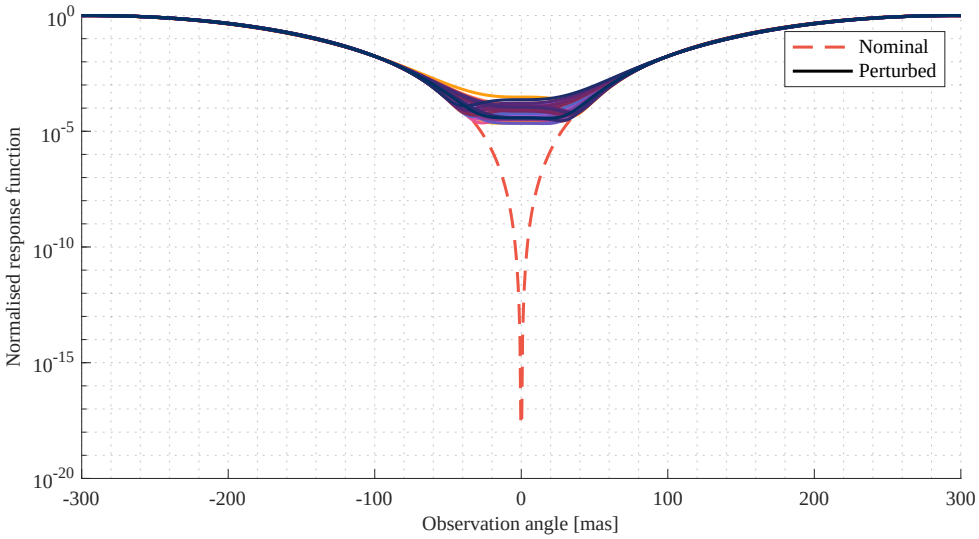

Figure 5.12: Comparison of the normalised integrated response function for the nominal and the perturbed system.

If the integration is performed, eventually the result shown in Figure 5.12 is shown, both for the nominal case (in dashed lines) and the perturbed systems, showing N_S overlapping lines. While for regions with bright fringes the lines tend to behave close to the ideal target, dark fringes significantly lose nulling power: in the best case scenario, the minimal perturbed line is found around 10^{-5} but can get as high as 10^{-3} (10^{-3} without compensator), which is clearly a strong loss in contrast, therefore showing how significant this loss can be for a real implementation.

5.3.2 Multiple branches perturbation

Results tend to become even less predictable once all the apertures are perturbed: starting from the pool of N_S simulations computed by the ray tracing software, for a specified number of N_{ms} perturbed simulations, each aperture is assigned one of the random simulations from the pool and the exact same procedure reported in Figure 5.7 is performed once more.

The virtual interferometric response, before integration, is shown in Figure 5.13: compared to what was shown previously for a single branch, the variations are covering a higher part of the diagram, given the higher amount of perturbations taken into account. The central point is not any more the point displaying the best behaviour.

Concerning the nulling power, while in Figure 5.9 all the diagrams looked almost the same, when considering multiple apertures, diagrams show different results as shown in Figure 5.14.

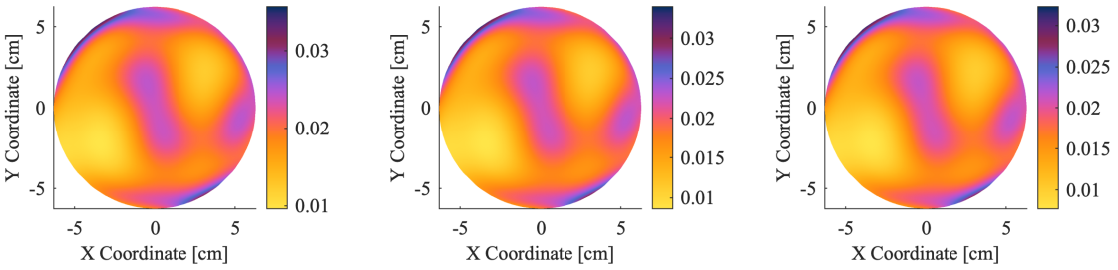

(a) -300 mas **(b)** 0 mas **(c)** 300 mas

Figure 5.13: Intensity response for every displaced ray of a Linear Array interferometer at pupil plane for different angular positions on the screen for the multiple-branches-perturbation simulation.

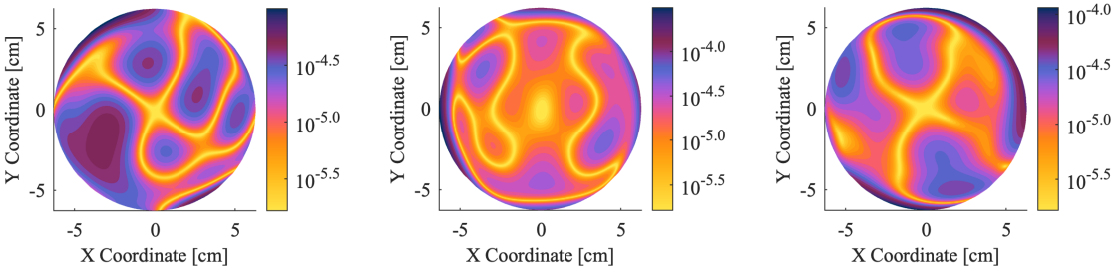

(a) 1st simulation **(b)** 2nd simulation **(c)** 3rd simulation

Figure 5.14: Nulling ratio distribution for every displaced ray of a Linear Array interferometer at pupil plane for three different random simulations from CODE V in the case of a multiple-perturbed-branches simulation.

Each of the N_{ms} simulations now yields a different result, mostly a consequence of how simulations are taken into account: for once, Figure 5.14b is significantly more perturbed than Figure 5.14a. The latter, in fact, shows a larger and spreader bright region (i.e. better nulling ratio), while the former has a wide dark region which is significant in indicating worse results.

The larger entity of multiple-branches perturbations is shown also in Figure 5.15, especially from Figure 5.15d: the size of the target nulling ratio region is significantly smaller than what was seen for a single branch perturbation, therefore pointing targets may become even more stringent than what was anticipated before.

The integrated response function (from Figure 5.16) summarises what has been shown by individual plots, displaying again the loss of the perturbed N_{ms} simulations over the nominal behaviour. While, with respect to the single branch perturbations, the result seems similar, it can be ultimately seen that now the worst case scenario is above the 10^{-3} limit previously mentioned.

As a conclusion, then, the changes in the interferometric response can visualise part of the performances of the system: while for the single perturbed arm there seems to be a certain tolerance to the error, with a larger region that present almost-nominal results, the same cannot be said about multiple-perturbed arms, which instead produce undesired results. Based on these results, then, it is also possible to design corrective elements to reduce the impacts of perturbations on the system through the fine-tuning of the compensators.

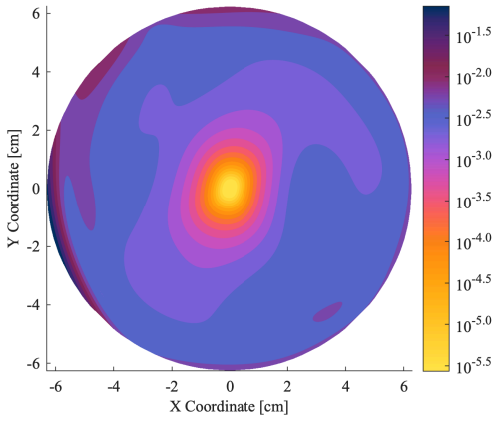

(a) Mean nulling ratio distribution

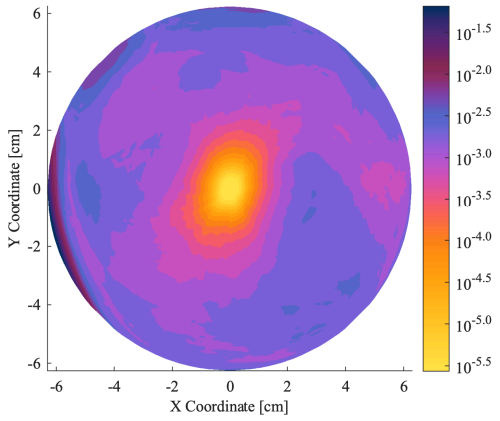

(b) Median nulling ratio distribution

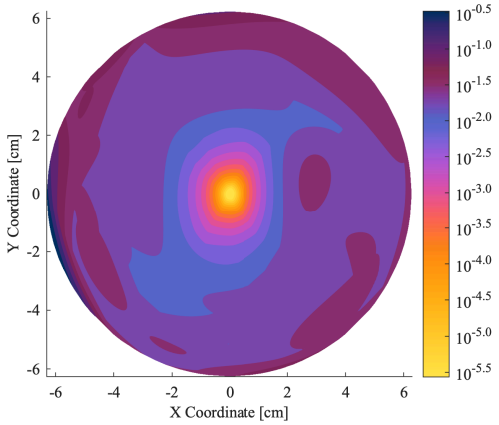

(c) Worst case nulling ratio distribution

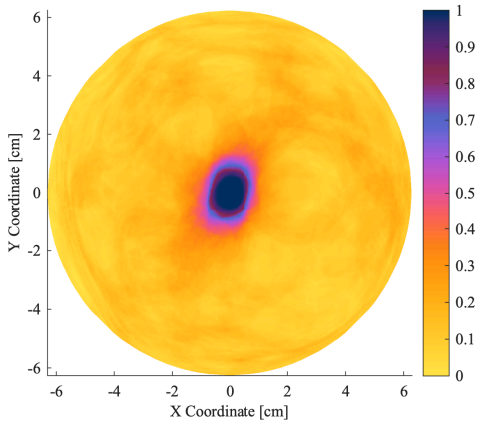

(d) Probability of high nulling ratio distribution

Figure 5.15: Statistical distributions of different performance indices for the nulling ratio distribution over every displaced ray of a Linear Array interferometer at pupil plane for all cumulative angular positions on the screen in the case where all the interferometry branches were perturbed.

5.4 Overview of statistical analysis

Up to this point, considerations on the combination of different branches have led to the visualisation of how the nulling behaviour and the response function are changed by such perturbations. This section aims to visualise how the remaining performance parameters that can be associated to a nulling interferometer change.

In order to analyse such changes in the system, for each simulation, each of which has N_P points, the root-mean-square value of the property under analysis (transmission maps, PSFs and exoplanet yields) will be taken as a measure of the perturbation of the phase, thus leading to N_S cumulative curves or surfaces that can be studied through statistical analysis.

5.4.1 Transmission maps

The transmission map is a key element of the interferometer, since it shows which regions of the sky are mapped to a nulling region and which ones are instead mapped to a constructive behaviour. This is fundamental to displaying the response of the interferometer to differently placed exoplanets.

Once again, the transmission map is computed by evaluating Equation 5.1 as a function

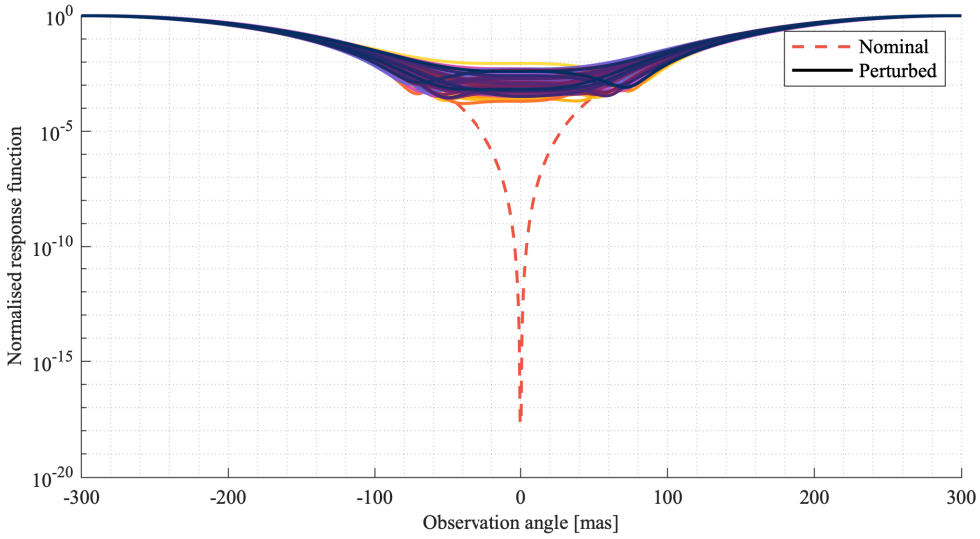

Figure 5.16: Comparison of the normalised integrated response function for the nominal and the perturbed system in the case of multiple-branches-perturbation simulation.

of the vectorial variable $\boldsymbol{\vartheta}$ (since computed at the virtual image plane), producing the familiar fringe pattern expected by the considered configuration. Nominal results were presented in Section 3.5.

What happens, however, if the configuration is no longer ideal and how significant are the changes in the response? A quick answer can be provided by Figure 5.17a which computes the standard deviation for each point of the transmission map: the regions that display the highest variation are those close to the change of concavity of the curve. The regions where normally the highest nulling or the highest constructive points are found are instead significantly less affected by perturbations (by at least one order of magnitude).

Another way to see specifically how the central point, being the target position of the harbouring star, is affected by perturbations is shown by Figure 5.17b, which shows the cumulative distribution probability of a difference value at the origin point smaller than a specific value. Indeed, this graph shows that, for differences up to 0.01% (since the plot was normalised), the probability is around 70%. This is a significant result that, in accordance with Figure 5.17a, states that the centre region is less affected by big perturbations, with only small values differences found here.

The same conclusion can be drawn by looking at the principal component analysis, reported in Figure 5.17c. Given a matrix made by N_ϑ points (which is a reshaped vector of the transmission map points from Equation 5.1) due to N_S simulations and by subtracting the mean value to it,

$$\tilde{\mathbf{X}} = \mathbf{X} - \bar{\mathbf{X}}, \tag{5.4}$$

and by computing the eigenvectors of the covariance matrix associated to these values,

$$\mathbf{C} = \frac{1}{N_S - 1}\tilde{\mathbf{X}}^T\tilde{\mathbf{X}} \qquad \Rightarrow \qquad \mathbf{C}\mathbf{v}_i = \lambda \mathbf{v}_i, \tag{5.5}$$

the resulting eigenvector matrix contains the principal components, shown in Figure 5.17c. Similarly to the standard deviation, again it is shown that regions mostly affected by the perturbations are the transition regions, leaving the nulling and constructive regions mostly unaffected.

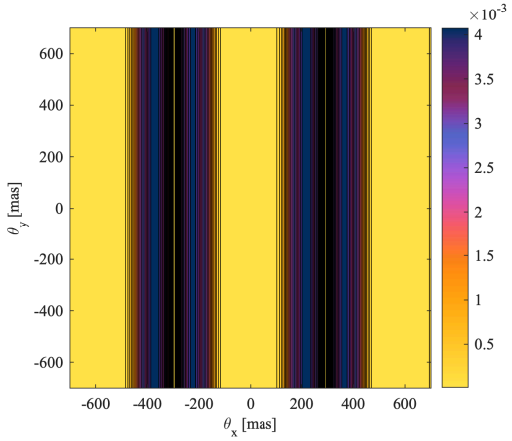

(a) Standard deviation

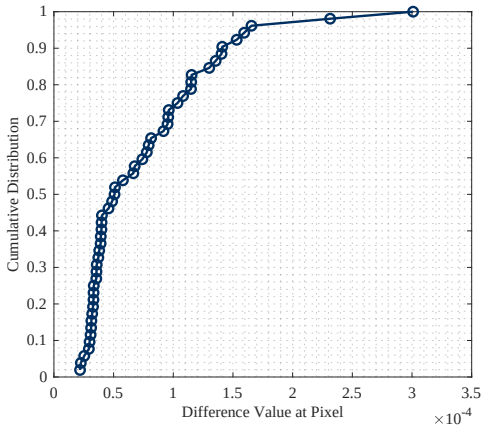

(b) Cumulative distribution function

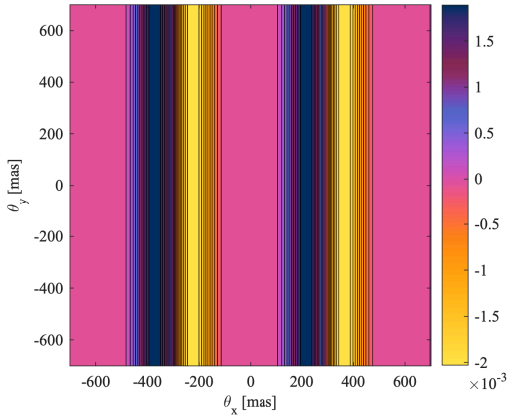

(c) Principal component analysis

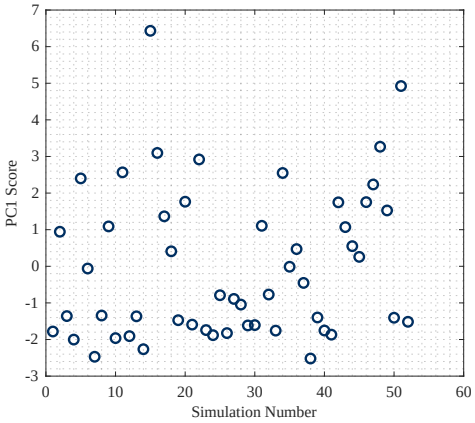

(d) First principal component scores

Figure 5.17: Analysis on the N_s simulations in terms of performances of the interferometer, based on the root-mean-square values, on the transmission map.

The validity of the principal component analysis is given by the score associated to the first eigenvector,

$$\mathrm{PC1}_{\mathrm{score}} = \tilde{\mathbf{X}}\mathbf{v}_i, \tag{5.6}$$

and is reported in Figure 5.17d. Depending on the statistical ensemble, there could be interest in the sign, but most importantly having a non null score indicates a good participation in the considered aspect: in this case, it is abundantly clear that most of the simulations display a significant departure from the null indication; while such departure can be positive (e.g. in accordance with PC1) or negative (in the opposite direction of PC1), for this specific case of random perturbations, it does not hold any particular consideration.

5.4.2 Point spread function

Another key element that has been analysed is the point spread function, reported as the dirty map obtained from the convolution of the unique apertures of the array. Much like the transmission map, the PSF is not significant *per se*, but is associated with many important breakthroughs like the modulation efficiency associated to the planet and the inner working angle. The nominal appearance of the point spread function was presented in Section 3.8.

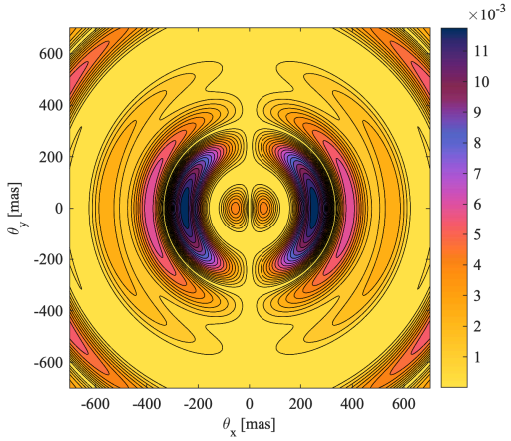

(a) Standard deviation

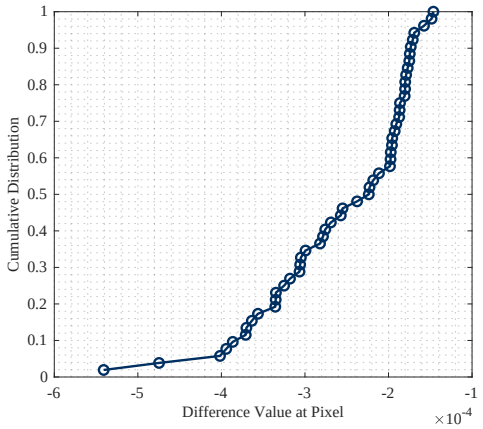

(b) Cumulative distribution function

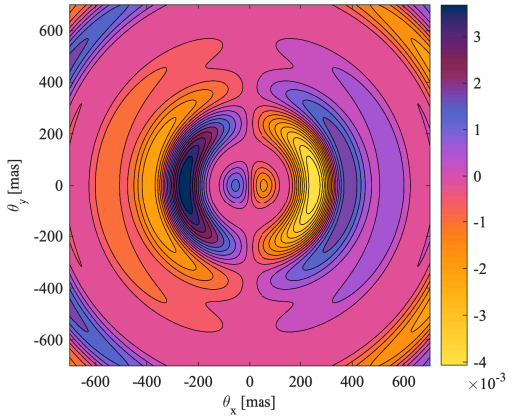

(c) Principal component analysis

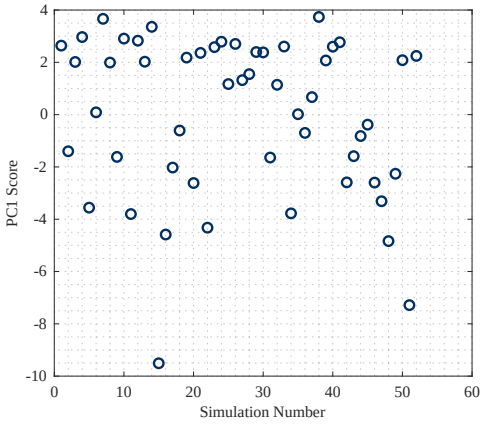

(d) First principal component scores

Figure 5.18: Analysis on the N_s simulations in terms of performances of the interferometer, based on the root-mean-square values, on the point spread function.

Similarly to what it has been shown before, Figure 5.18a presents the standard deviation associated to the N_S simulations taken into account: once again, some regions–namely, those that do not present any peak or pit–are mostly constant, while the highest variation is found in the two main lobes of the figures at their strongest value, then decreasing for the secondary and tertiary lobes of the analysis.

Like the transmission map, the PSF is also more resilient to variations at the central pixel, as seen in Figure 5.18b: for a variation of less 0.02% (in absolute values), the probability is found at more than 40% (by subtracting from the negative value seen in the graph). This is a further confirmation of the resistance of the system to significant variations.

The principal component analysis is reported in Figure 5.18c, along with its scores in Figure 5.18d: contrary to the standard deviation, this graph clearly shows that the left lobe is subjected to small increases, while the right one to small decreases. This is particularly significant since it displays a "flatting" trend, since the left lobe is nominally the negative one and the right lobe is the positive one: as expected, then, perturbations cause a reduction of the visibility of features that will clearly result in a diminishing ability to obtain a valid contrast in the images.

In accordance to what is has been stated, the scores are mostly found in the positive region (and once again, most of them are non-zero): despite the randomness of the perturbing variables, then, the resulting effects do clearly show a trend.

5.4.3 Potential exoplanets yield

The previous sections have shown how the perturbations affect the performances of the interferometer based on few important metrics that have shown the tendency to reduce the contrast and therefore the nulling ability of the instrument. The key metric, however, is undeniably the exoplanets yield of the instrument.

One of the best way to provide an evaluation on the validity of the instrument is to establish how much exoplanets it will be able to see and this is measurable thanks to the availability of statistical tools like P-POP[52] that generate synthetic populations of exoplanets based on found data (mostly from NASA's Kepler).

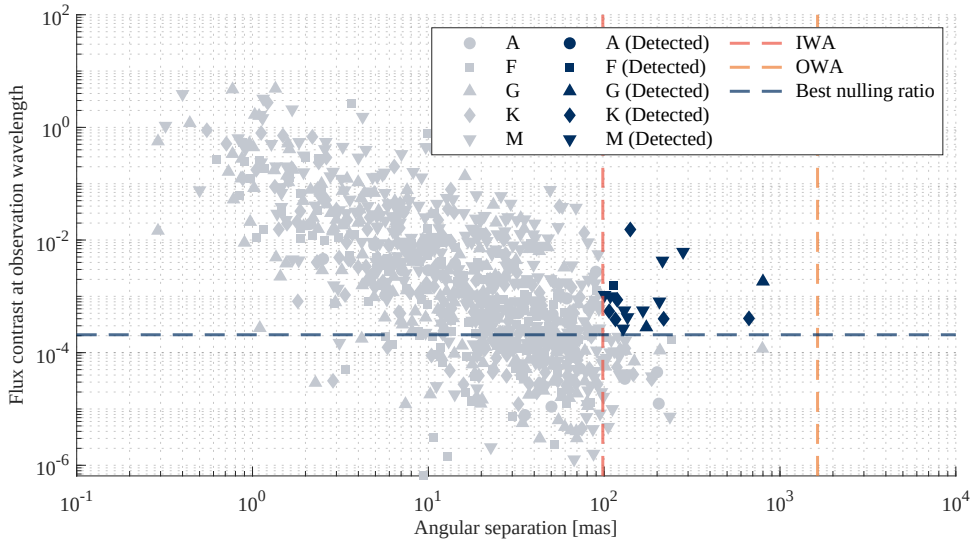

(a) Example yield of a random universe.

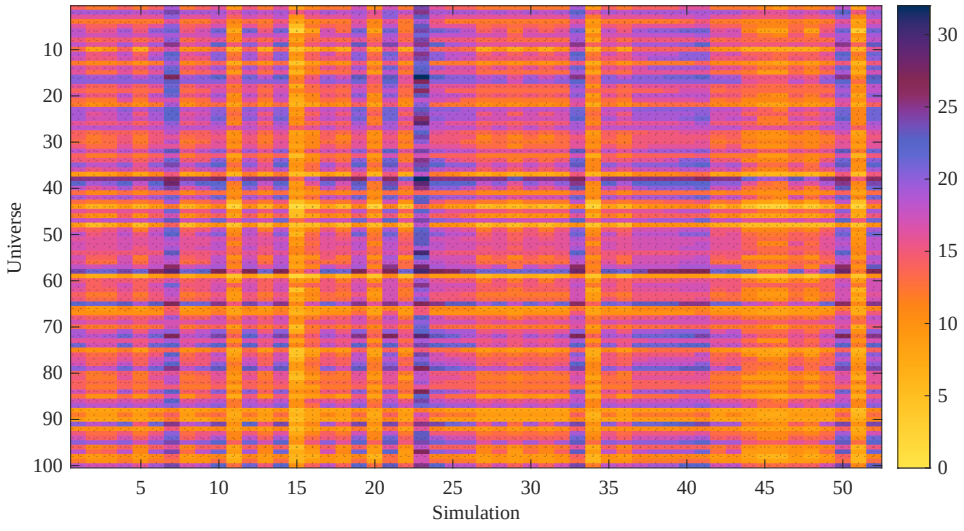

(b) Yield heatmap: number of detections for each universe and simulation.

Figure 5.19: Analysis of the possible yields of the system from the P-POP catalogue.

Out of N_u universes that have been generated by P-POP and N_S simulations due to perturbations, then, it is possible to obtain $N_u \times N_S$ different situations with different yields. In general, a planet can said to be seen if:

- Its angular distance from its harbouring star is smaller than the outer working angle,

a value that depends on the diameter of the apertures and the amount of light they can collect, as well as the wavelength. This is usually the easiest requirement to satisfy, as even small apertures are large enough to capture all possible planets.

- Its angular distance from its harbouring star is larger than the inner working angle, a value that depends on the baseline and the wavelength; while it has been shown that this value is not coincident with the resolution, it still holds a significant relation with it and is highly reducing the possible catch, especially for the order of baselines that could fit a single spacecraft.
- Its ratio with respect to the star flux at the observation wavelength is larger than the nulling ratio. In general, most planets become observable even for small integration times (like 24 hours), but longer observation times could increase the yield, but generally reduce the number of observable planets during the spacecraft lifetime.

Clearly, this is only a limited first estimation of the possible exoplanets yield that neglects many effects, including noise sources, instabilities of nulling ratio, the transmission maps and many other confusion-making elements within the sky.

One of these situations (a random universe over a random simulation) is shown in Figure 5.19a: as it can be seen, only a partial number of possible exoplanets is possibly seen by the interferometer and the harder limitation seems to be linked to the inner working angle. As for many other engineering problems, it is therefore a matter of trading off for the better aspect, knowing all the possible limitations on sizes and optimisations. The integration time has been selected by looking at similar mission concepts[20].

While Figure 5.19a returns an immediate comprehension of the problem, the general solution is found by looking at the heat map in Figure 5.19b, which provides the sum for every universe and simulation. While there are some unlucky simulations and universes, on average, the amount of detections reflects the expected one from similar concepts[20],[91].

5.5 Perturbed comparison for multiple arrays

To prove the generality of the results that have been shown for a single configuration, this section applies the same methods to five different arrays presented by Lay[65], focusing on metrics of interest like modulation efficiency and nulling ratio using the root-mean-square value of the perturbations. The results will be compared with respect to the nominal value to see the performance loss within the system. The five nominal systems have been studied in Section 3.9. As an additional consideration, only perturbations within each branch are here considered, but clearly, in a real assembly, the way elements are placed one to the other can and will still introduce other disturbances that are here neglected.

Figure 5.20a displays a violin plot for the modulation efficiency. The violin plot allows to see both the distribution and the frequency of each interval, along with the nominal point, displayed in red. It is interesting to see that, while all the arrays display a significant loss in terms of quality, the modulation efficiency, which itself depends mostly on the phase combinations, is similar for all the arrays. The results are then expected: despite the changing in the array dimensions, then, what matters are the root-mean-square values of the perturbations which are, in fact, always the same for all the different arrays, hence causing a significant, but constant shift for all the considered arrays.

Once again, the second Linear DCB displays the best result, in line with the other nominal values, yet it actually displayed the largest loss in absolute values (around 60% loss), while the other arrays only loose around 40%). It is therefore significant that similar perturbation can cause such high losses to the system.

Figure 5.20b displays instead the nulling ratio distribution with respect to the nominal

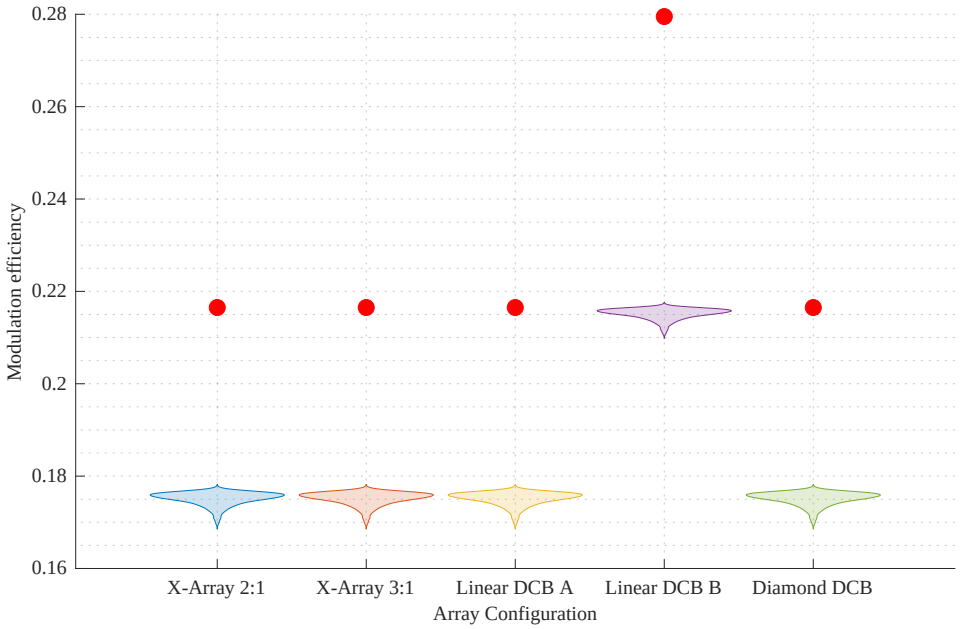

(a) Modulation efficiency.

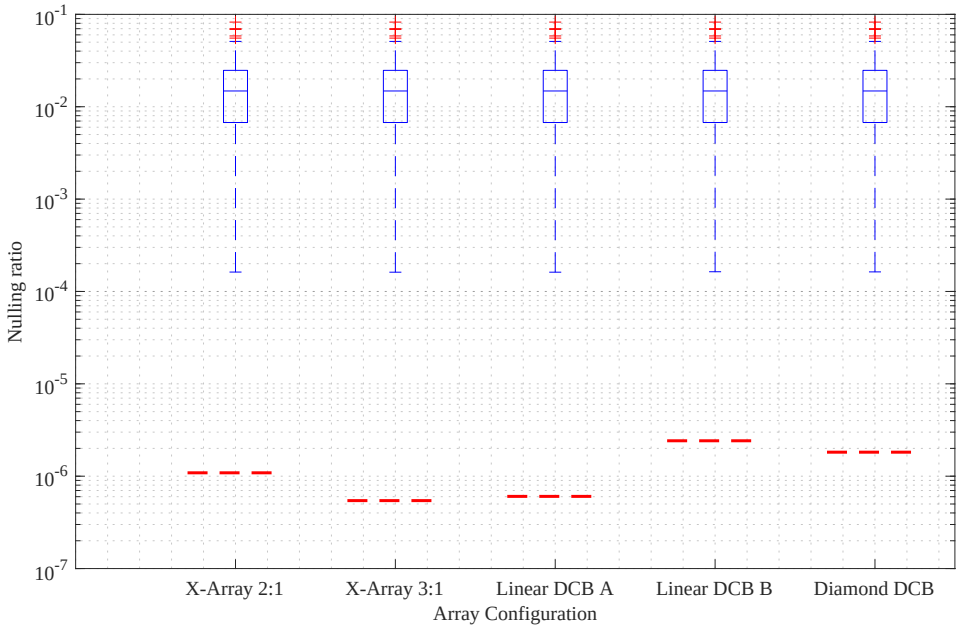

(b) Nulling ratio.

Figure 5.20: Comparison of how the perturbations act on different arrays, in terms of modulation efficiency (visualised with a violin plot) and nulling ratio (with a box plot). The red dashed line and points represent the nominal behaviour.

value, which is nominally dependent on the baselines as well, hence behaving differently depending on the different available combinations. For this reason, then, ideally, both the 3:1 X-Array and the first Linear DCB array are actually both similarly behaving ideally, with the former being the best possible choice. Once the system is perturbed, however, this is not true any more as the distribution cause an standardization of the results which condense to higher intervals, without any particular preference.

In conclusion, then, while the nominal analysis did presents the different strengths of each design, once a perturbation is performed, none of the considered arrays display a significant resistance to the errors, hence the choice of the array to produce may be shifted in favour of other parameters, like the mechanical complexity or the dry weight.

Figure 5.21 provides a summary for every different array and for every simulations, that once again show that all the very different configurations are actually behaving in the same way–despite the nominal differences. For this reason, then, it is fundamental to reduce as much as possible the effects of the perturbations that can highly reduce the quality of interferometry.

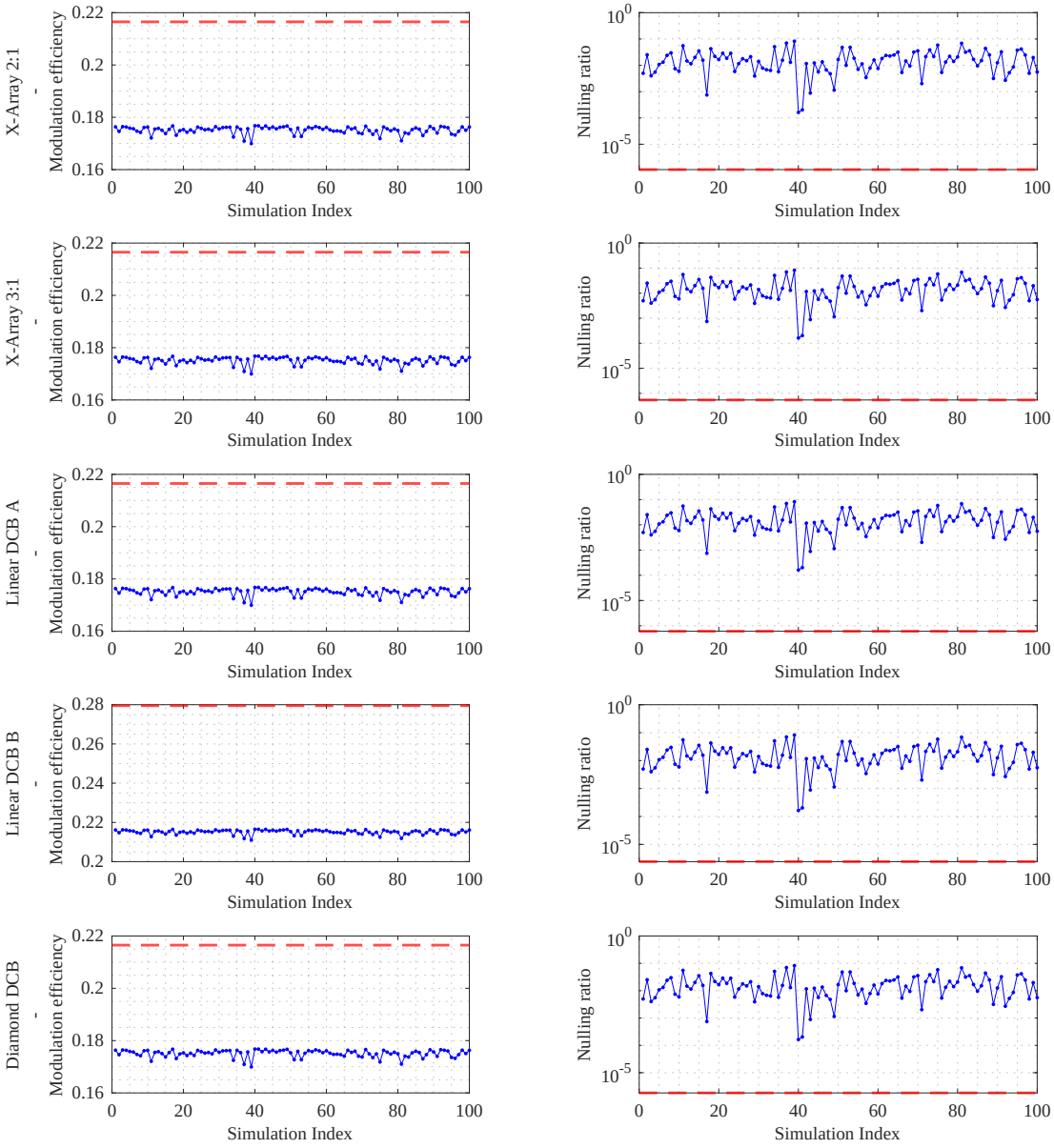

(a) Modulation efficiency. **(b)** Nulling ratio.

Figure 5.21: Comparison of how the perturbations act on different arrays, in terms of modulation efficiency and nulling ratio for all the different simulations. The red dashed line represents the nominal behaviour.

6 Model validation

From the broad theoretical concepts illustrated, a model has been developed with a strong focus on perturbation and sensitivity analyses. One additional way to support and validate the tools proposed here is to perform some benchmarks on already proven instruments, such as the two concept missions Darwin and TPF-I, and their successor, LIFE, which were introduced in Chapter 1. While new mission proposals exist[17], the broad availability of data and the extensive literature produced on these three missions allow for a more general comparison.

This chapter will therefore primarily make use of tools presented in the modelling and sensitivity chapters to visualise how real mission candidates would have performed in a real-world scenario and, ultimately, how many planets would have been detected and possibly studied by the instruments—broadening scientific horizons in the search for exoplanetary signs of life.

Finally, considerations on the validity of the detected exoplanets are addressed in terms of habitable zones, aiming to answer the question of whether nulling interferometry could potentially have a role in this discussion.

6.1 Overview of the Three Missions: Literature Review and Model Setup

Parameter	Darwin[15],[70]	TPF-I[62],[88],[63]	LIFE[91],[45],[42]
Agency	ESA	NASA	ETH/ESA
Array	Emma X-Array 3:1	X-Array 6:1	X-Array 6:1
Apertures	4×2 m	4×2 m	$4\times \geqslant 2$ m
Null. baselines	170 m	$20 - 67$ m	$100 - 600$ m
Imag. baselines	500 m	$120 - 400$ m	$60 - 600$ m
Throughput	$\approx 10\%$	N.A.	$\approx 5\%$
Nulling ratio	10^{-5} at $(6 - 20)$ µm	10^{-5} at 10 µm	10^{-5} at $(6 - 16)$ µm
Mod. efficiency	0.3	0.5	0.4-0.6
Detectable plan.	≈ 200	72	$315 - 550 - 770^{\dagger}$
OPD stability	$\leqslant 2$ nm	$\leqslant 5$ nm	$\leqslant 1 - 5$ nm

Table 6.1: Literature data available on the three proposed missions during their development cycle, the throughput refers to the overall photon-to-detector efficiency. †Depending on the used size of the aperture, more planets can be detected.

As already stated in Chapter 1, both Darwin and TPF-I went through a "troubled" life,

being carried as experimental missions in a field that was, at the time, still relatively young[2],[8] and open to many improvements. LIFE, instead, has risen from the ashes of the past missions, carrying over the most important developments.

All three mission concepts target extreme starlight suppression in the mid-infrared region as their primary goal: Darwin and TPF-I were designed to null the star to a residual depth of the order of 10^{-5} over a relatively broad region of 6–18 µm[15],[62], while LIFE inherited similar requirements. For the first, laboratory breadboards achieved 1.2×10^{-5} and even deeper nulls in monochromatic tests[15], while NASA used an achromatic nuller testbed which demonstrated a 10^{-6} suppression under strong controls on phase and amplitude[62].

Contrary to missions currently in preliminary phases[17],[13], the three designs use formation flying arrays with multiple collectors. One of the key elements of Darwin was the Emma X-Array (a non-coplanar X-Array), which employs four collector spacecraft and a central beam-combiner, with different possible baselines[15], enabling resolutions down to dozens of milliarcseconds, thereby maximising the imaging capability while decoupling the nulling strength of the array. Similarly, TPF-I ultimately adopted the Emma X-Array with comparable dimensions[62], while LIFE adopted a double Bracewell X-Array architecture[42], which is adjustable for each target. In all cases, the dimensions are consistent with achieving resolutions suitable for observing Earth–Sun habitable zones.

Darwin's studies found that a two-year search could screen about 200 stars (of spectral types F, G, K, and M)[15], and therefore expected a similar number of planets. A discrepancy is found with TPF-I, which reported a very low number of detections—only 72—despite very similar dimensions to ESA's mission[62]; given the lack of data on statistical populations of exoplanets at the time, a very rough estimation was made. Using actual exoplanet occurrence rates, LIFE is predicted to outperform Darwin, with around 550 rocky and super-Earth planets expected[91],[59], under the assumptions of high signal-to-noise ratios and no contrast cut-off[91].

As extensively analysed, nulling performance is extremely sensitive to optical path difference errors, and even nanometric errors can introduce stellar leakage. For Darwin and TPF-I, technology demonstrations have shown that the combiner must hold path-length errors down to nanometric precision to maintain the desired nulls[34]. Regarding stability, there is a whole series of analyses that could be performed, and the same principles apply to LIFE as well: to achieve the desired stability, active control (fringe tracking, OPD dithering, etc.) is required. From these principles, the 6:1 ratio was chosen for its robustness against OPD instability[67],[91].

Table 6.1 provides a comparison of the main parameters of interest for the three missions: the same data has been used to tune the model through three simulations (as seen in Section 3.9). Table 6.2 includes the results of the model.

As expected, most of the results are in line with those reported in the literature, with only Darwin and TPF-I displaying a slightly lower than expected nulling ratio (which can still be rounded to 10^{-5}), thus highlighting the validity of the model, which can be used to study even further missions.

6.2 Interferometer Array Design: Choices and Trade-offs

As Section 6.1 briefly mentioned, the choice of the apertures ratio is the result of a strong optimisation process that involves imaging, nulling and stability issues. Whilst the last aspect will be neglected in the analysis, which focuses only on the static considerations, the first two can be easily visualised by seeing the sensitivity of two key metrics, the nulling

Mission	Ap.	Position $\mathbf{X}_j$ [L]	Position $\mathbf{Y}_j$ [L]	$\boldsymbol{\varphi}$ [deg]	$\boldsymbol{\eta}_{\mathbf{mod},\infty}$	$\boldsymbol{\vartheta}_{\mathbf{IWA}}$ [λ/L]	$\boldsymbol{\vartheta}_{\mathbf{FWHM}}$ [λ/L]	G
Darwin	1	0.493	0.082	270	0.346	3.041	0.482	$10^{-3.12}$
	2	0.493	-0.082	90				
	3	-0.493	-0.082	180				
	4	-0.493	0.082	0				
TPF-I	1	0.493	0.082	270	0.520	3.041	0.482	$10^{-3.32}$
	2	0.493	-0.082	90				
	3	-0.493	-0.082	180				
	4	-0.493	0.082	0				
LIFE	1	0.493	0.082	270	0.416	3.041	0.482	$10^{-4.52}$
	2	0.493	-0.082	90				
	3	-0.493	-0.082	180				
	4	-0.493	0.082	0				

Table 6.2: Comparison table for Darwin, TPF-I and LIFE with normalised results for positions, modulation efficiency (higher is better), inner working angles (lower is better) and resolution angles (lower is better). Ap. is the aperture, φ is the assigned phase and G is the nulling ratio (higher exponent is better).

ratio and the inner working angles.

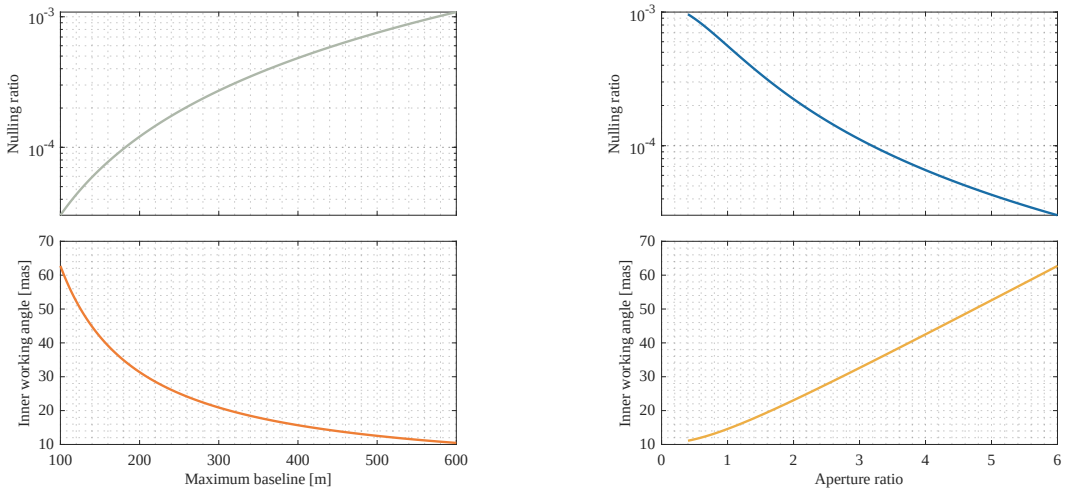

(a) Sensitivity of the baseline changes.

(b) Sensitivity to the apertures ratio changes.

Figure 6.1: Sensitivity of nulling ratio and inner working angle to variations in baseline and aperture ratio (longer baseline over smaller baseline) of an X-Array (based on the characteristics of Darwin from Table 6.1).

Therefore, Figure 6.1 provides an overview of how two key metrics in the exoplanets search change with respect to modifications in the position of the apertures. It is immediately clear why this is not an easy task: by focusing, for example, on how the baseline impacts the metrics (Figure 6.1a), it can be seen, as already introduced and verified, that a larger baseline strongly reduces the inner working angle. A lower IWA implies a better resolution and more exoplanets can be detected.

A natural consequence, however, of how the stellar angular dimension participates in the computation of the nulling ratio (given in Equation 3.18) and the fact that the resolution strongly increases, is that larger arrays start to resolve the star, hence losing rejection rates. The necessity of having a modifiable flying formation may therefore be a consequence of

different requirements over different possible targets.

The aperture ratio, being the ratio between the longest and the shortest baselines of an X-Array interferometer, is similarly affected by this optimisation problem but in the opposite way: a higher aspect ratio essentially reduces the nulling baselines (those baselines that, thanks to their destructive phase differences, contribute the most to the nulling effects, as introduced in Section 3.6), therefore enhancing their resolution and therefore more efficiently contrasting the stellar brightness.

However, a higher aperture ratio causes the inner working angle to increase, as the result of the reduction of the nulling baselines; since the IWA is inversely proportional to their lengths (as introduced in Section 3.8.3), it is only natural that the angle, as a consequence, increases.

6.2.1 Optimising Baseline and Aperture Ratio: A Design Trade-off

Is there a feasible balance possible between the nulling ratio and the aperture ratio? Looking at Figure 6.1 it seems natural to try targeting the centre of the considered interval to balance both characteristics. But how do they impact the global system?

To study this impact, a solver has been exploited in MATLAB; among the large ensemble provided, the one-dimensional bounded minimiser `fminbnd`[75] has been implemented to find the best baseline or aperture ratio to grant the cumulative best nulling ratio and inner working angle. The cost function is

$$f(x) = w \cdot \frac{\log(G(x)) - \min_{x\in X} \log(G(x))}{\max_{x\in X} \log(G(x)) - \min_{x\in X} \log(G(x))} + \\ + (1-w) \cdot \frac{\mathrm{IWA}(x) - \min_{x\in X} \mathrm{IWA}(x)}{\max_{x\in X} \mathrm{IWA}(x) - \min_{x\in X} \mathrm{IWA}(x)}, \quad (6.1)$$

where x is either the baseline or the aperture ratio in the two cases that have been implemented, w is the weight, a factor that is used to favour one parameter with respect to the other and is always found between 0 and 1, and X is the set with values that can be taken by the optimisation parameter.

Table 6.3 presents the boundaries that have been set in the two optimisation parameters, selected based on the literature data from Table 6.1; for completeness, the aperture ratio considers minor than 1 ratios, in order to study how the different separations over different assigned phases work on the system. Six optimisations have been carried out in total: three on the baseline and three on the aperture ratios. For each of the two parameters, three different weights have been considered: one where the two parameters share the same importance ($w = 0.5$), one where the nulling ratio is favoured ($w = 0.6$) and, vice-versa, one where the inner working angle is considered to be more important ($w = 0.4$). When optimising the baseline, the aperture ratio is considered constant and equal to the nominal value from Table 6.1 and the same goes for the baseline when the optimising parameter is the aspect ratio.

The results of the analysis are given in Table 6.4, which returns the optimised parameter x, the resulting nulling ratio, inner working angle and mean number of detections. Initially, let us consider the optimisation over the aperture ratio (therefore every even column): the three missions, given their similarity, return very similar results, that is that a lower aperture ratio (1.65) is preferable for a better IWA, whilst a higher value (4.23 or 4.22) is chosen to improve the nulling ratio. For Darwin and TPF-I it is clear that the preferred path is an optimisation of the nulling ratio, since the possible detections (that ultimately, is the key parameter) are strongly higher. The same cannot be said for LIFE, which from

	X	
Parameter	**Minimum**	**Maximum**
Maximum baseline [m]	100	600
Aperture ratio	0.4	6

Table 6.3: Boundaries of the optimisation problem for the baseline and the aperture ratio, selected based on the literature values for the available missions.

		Optimisation parameter x		**Nulling ratio**		**Inner working angles [mas]**		**Detections**	
Mission	**Weights**	Baseline [m]	Aperture ratio	Baseline	Aperture ratio	Baseline	Aperture ratio	Baseline	Aperture ratio
Darwin	0.4	322.52	1.65	$10^{-3.50}$	$10^{-2.12}$	19.45	3.97	211.66	126.29
	0.5	215.00	2.72	$10^{-3.86}$	$10^{-2.48}$	29.18	5.97	202.94	151.04
	0.6	143.33	4.23	$10^{-4.21}$	$10^{-2.83}$	43.77	8.96	166.25	177.80
TPF-I	0.4	322.52	1.65	$10^{-3.50}$	$10^{-2.32}$	19.45	4.97	211.66	139.58
	0.5	215.00	2.72	$10^{-3.86}$	$10^{-2.67}$	29.18	7.46	202.94	165.71
	0.6	143.33	4.23	$10^{-4.21}$	$10^{-3.02}$	43.77	11.19	166.25	191.32
LIFE	0.4	322.52	1.65	$10^{-3.50}$	$10^{-3.52}$	19.45	19.88	211.66	211.99
	0.5	215.00	2.71	$10^{-3.86}$	$10^{-3.87}$	29.18	29.82	202.94	201.72
	0.6	143.33	4.22	$10^{-4.21}$	$10^{-4.23}$	43.77	44.73	166.25	163.21

Table 6.4: Results of the optimisation process (in terms of resulting nulling ratio, inner working angle and mean number of resulting detections) over the baseline and the aperture ratio over three different weights (0.4, 0.5 and 0.6) for the three different missions.

the start has a strong nulling ratio and its optimisation comes at the price of increasing the IWA, therefore limiting the research region and producing a strong reduction in the results. On the opposite side, choosing $w = 0.4$ makes the yield go from 202 to 212 planets despite the reduction of the nulling ratio from $10^{-3.87}$ to $10^{-3.52}$.

By considering, instead, the odd columns, the optimisation is being performed on the baseline. By jumping directly to the detections, it is clear that this parameter is more determinant in getting good results, as the detections are always larger (or, at least, close) to the counterpart optimisation on the aperture ratio. In this case, favouring the inner working angle ($w = 0.4$) is always preferable, as it is the parameter that returns the higher yield, at least in the interval provided.

This section wanted to present a justification for the necessity of optimisation of the array, a task that is everything but simple. Mechanical requirements aside, the problem is key to understanding how the number of detections is affected by the global "shape" of the interferometer, therefore allowing for a better design.

6.3 Detecting Exoplanets: Performance and Capabilities

The concept of exoplanet yield has been carried over the entire work, applied to different concept missions and analysed in terms of degradation due to perturbations. Here it is extensively analysed with respect to the three proposed concept missions.

As Section 5.4.3 explained, an exoplanet is detected if found in the delimited region by the nulling ratio, the inner working angle and the outer working angle. Whilst the two latter parameters are given by the geometry and are not modifiable once the design has been set (apart from formation flying in some limited situations), the integration time allows one to essentially "shift" the population towards the upper part, hence partially overcoming this limitation.

It must be stressed, however, that the higher the integration time, the lower the possible number of exoplanets that can be studied: on one hand, nulling interferometry can help in the detection of exoplanets, but as explained in Chapter 1, the strength of the increased resolution in the considered spectral range is the possibility to actually study the planets (since other detection methods, especially the indirect ones, cannot do).

6.3.1 Astronomical Background

Not all the planets are equally interesting in the field of astrobiology and therefore a brief consideration on the considered topic is necessary. In the following analysis, therefore, the classification proposed by Kopparapu[59] will be exploited, in order to analyse the detectability and the habitability of possible different planets.

Rocky planets (i.e. those whose radius is equal to or below $1R_\oplus$) are composed predominantly of silicates and metals[83]; lacking substantial hydrogen envelopes and generally colder, they are generally harder to detect[93], whilst Super-Earths are planets with radii between 1 and $1.75R_\oplus$ (up to 10 Earth's masses), being generally rocky or with substantial volatile layers[85].

They generally display internal heating and geodynamo thanks to the carbon cycle and the shielding from cosmic rays[99],[41]. Water is usually found at stable conditions and water clouds can form in specific habitable regions when the surface pressure is sufficient[48],[82]. Around M dwarfs, in addition to that, tidal forces can provide additional heat to sustain subsurface oceans (similar to Europa)[51].

Sub-Neptunes (1.75-3.5 $R_\oplus$) typically display dominant hydrogen-dominated atmospheres

above rocky or icy cores[28],[85] and they were the most common class found by Kepler[11]. Immediately above, Sub-Jovian planets are found (3.5-6 $R_\oplus$) with intermediate densities and thick gaseous envelopes[28], whilst eventually Jovian planets are found: dominated by massive hydrogen-helium envelopes, they are the easier targets for nulling interferometers but the less interesting from an astrobiology point of view, since they are inhospitable (even though their large moons could host life in specific circumstances)[85]. Sub-Neptunes and Sub-Jovians have instead high surface pressures that may preclude liquid water surfaces, but could still display internal oceans.

Besides the planets themselves, hosting stars are as important in the determination of habitability and biosignatures. A-Type stars, for example, have short lifetimes ($\approx 10^8$ yr), effectively too brief for complex life to evolve, and, besides the emission of intense UV, they almost never display close-in planets, as proved by Kepler, which instead found many Jupiter-mass companions. They are bright and hard to detect, but planets are found at higher angular separations[40].

F-Type stars are hotter and more massive than the Sun, with moderate occurrences of Earth- and Neptune-size planets[79], whilst G-Type stars are prime targets due to the Sun being the sole known exponent with biological activity. The longer lifespan (≈10 Gyr) and moderate UV allow for evolution of life[90],[92].

K-dwarfs are cooler and longer-living, hosting more compact systems that present more small planets, making them valid candidates as well[79], but M-dwarfs are the most abundant hosts of terrestrial and mini-Neptune planets (around double) but the habitable zone is very tight, so making them generally harder to detect[79],[92].

6.3.2 Expected Yield Analysis

Parameter	Darwin	TPF-I	LIFE
Mean number of detections	197.67	206.87	111.47
Median number of detections	196.50	205.00	111.00
Median radius [$R_\oplus$]	1.32	1.32	1.32
Mean number of “Rocky” planets	20.56	22.33	28.32
Mean number of “Super-Earth” planets	39.93	43.48	29.47
Mean number of “Sub-Neptunes” planets	83.92	88.09	34.65
Mean number of “Sub-Jovian” planets	27.70	28.51	10.59
Mean number of “Jovian” planets	24.16	23.09	8.07
Mean number of planets around A, F, G and K stars	95.16	101.12	53.58
Mean number of planets around M stars	102.51	105.75	57.89
Mean temperature [K]	280.92	260.15	187.63
Mean distance [pc]	8.87	8.85	6.83
Minimum distance [pc]	1.30	1.30	1.30

Table 6.5: Statistic analysis based on P-POP[52],[53] for the three nominal configurations under ideal conditions concerning the results of possible exoplanets yield for each mission. The planet classification is based on their radius as detailed in Kopparapu et al., 2018[59],[20].

After a general introduction on the kinds of available planets, Table 6.5 provides the results of the three missions with a subdivision for the planet categories that were presented.

The first, most important result is that the mean number of detections, especially for Darwin, is completely in line with what was theorised in Table 6.1. Concerning TPF-I, as it was already addressed, the expected number was sourced from a limited pool

of exoplanets and therefore not in line with up-to-date figures, whilst, in the considered simulations, LIFE "suffered" from the minimum baseline considered in the analysis from the interval reported in the same table.

The strong limitation given by the IWA is particularly clear from the comparison graphs reported in Figure 6.2, which shows that, despite having the higher nulling ratio, at its minimum baseline of 100 m LIFE is the least-catching mission of the pool.

In general, given their high occurrence, M-type stars' exoplanets were the most detected (despite their closeness to the host star that could, theoretically, imply that the detected planets are actually too far from the habitable zone to be of interest).

In addition to that, the highest occurrence is for the sub-Neptunes planets for the three missions, again a consequence of them being the most common type. They are followed by the Super-Earths and later by the remaining part of the planets that, at least for Darwin and TPF-I, are located in the 20-30 range of detections.

6.3.3 Comparison with Ground-Based Observatories

By connecting back to the review of nulling interferometry presented in Chapter 1, now that space-based interferometers have been presented and evaluated in their most important metrics, it may be appropriate to discuss once more their validity, especially with respect to ground-based interferometry.

Clearly, the answer has not changed and ground-based systems, whilst essential for many operations, are still fundamentally constrained by the presence of the atmosphere. Not only is the infrared region (the most important both in terms of "easiness" of contrast between the planet and its host star and for key chemical signatures) significantly absorbed, but thermal background emission in the same region contributes significantly to the noise (in addition to turbulent effects, pollution and many other disturbing factors)[1],[12].

Ultimately, then, ground-based instruments can be seen, at least for the purpose of exoplanet detections, as providing a strong complementary role[1] in terms of technology demonstrations, target selection and, generally, sky coverage.

Therefore, the analysis has shown that not only would space-based interferometry fill a gap in our cosmic vision that would otherwise remain partial and secluded, but it could actually and potentially obtain a main role in the scientific and astronomical advancements in this field, leading to several fundamental discoveries in the following years after its implementation. From the results here estimated, then, whilst the upfront investment would certainly be considerable, the field of action of such a space-based instrument is not currently nor in the near future occupied by other instruments that could, in cheaper or more efficient ways, replicate its role. In definitive words, space-based nulling interferometry is the only answer to many questions we are currently facing.

6.4 Habitable Zone Analysis and Habitability Potential

As a final topic to discuss, with respect to the exoplanet yield, is the habitability of the detected planets. In general, the habitable zone is a distance region defined around each star, limited by two events:

- The runaway greenhouse, a scenario in which a planet's atmosphere becomes "thick" so that the planet is subjected to uncontrollable heating. The excessive release of carbon dioxide within the atmosphere, due, for example, to water evaporation, leads to a feedback loop of warming events. A primary example is Venus[54].
- The runaway glaciation, a climatic phenomenon where a planet experiences an ir-

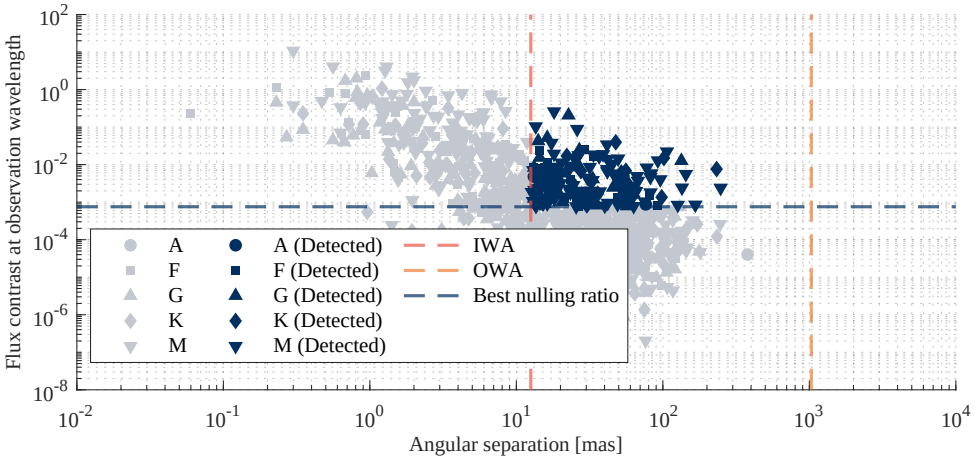

(a) Darwin.

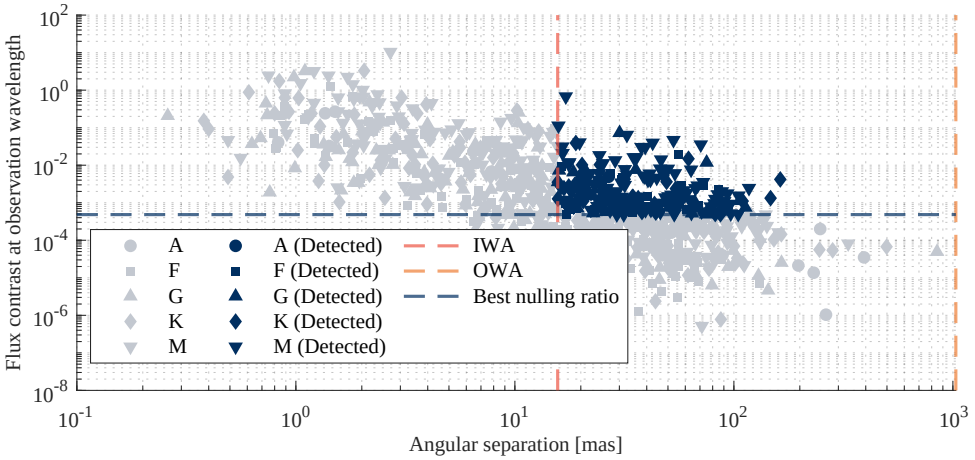

(b) TPF-I.

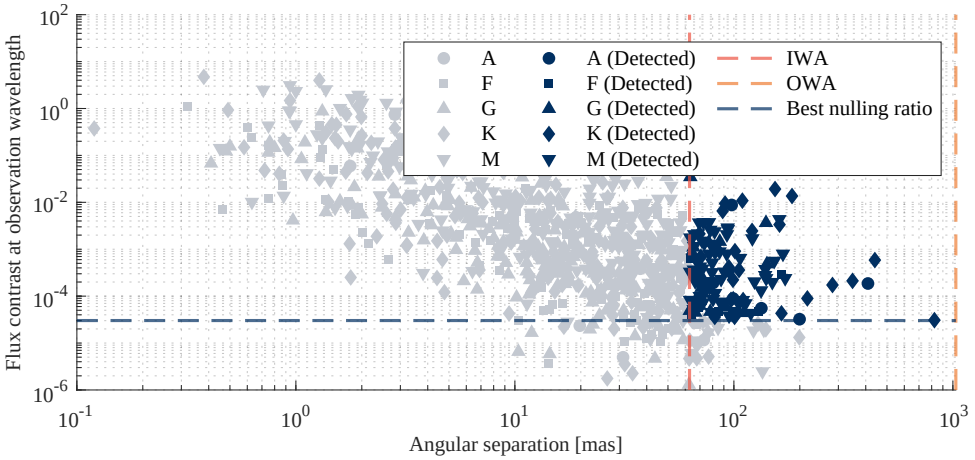

(c) LIFE.

Figure 6.2: Comparison, for three different random universes, of the possible resulting yield of the three missions.

reversible cooling leading to extensive ice coverage spread over the entire surface. As ice expands, it reflects more sunlight (increasing the planetary albedo), further cooling the planet and creating a feedback loop[54].

The habitable zone is therefore defined as the region in which a planet is realistically habitable, that is, a solid surface planet (or moon) which can maintain liquid water on its surface[54],[74].

Many factors affect the extension of the habitable zone, including the planet mass, the albedo, the density and composition of the atmosphere, the presence of clouds or the strength of internal geothermal energy, but in general, the key parameters are the star brightness and the orbit of the planet itself[54]. For the solar system, the continuous habitable zone is generally defined between 0.95 and 1.52 AU, a distance that includes both Earth and Mars[54],[74].

Kopparapu et al.[60] propose a general relation for the computation of the extensions (in astronomical units) of the habitable zone for any main sequence star whose effective temperature is found in the range 2600 K $\leqslant T_{\text{eff}} \leqslant$ 7200 K (out of the 30291 stars, spanned over the 100 universes, found in the P-POP catalogue here considered, only 743 stars were filtered out):

$$d = \sqrt{\frac{L/L_{\odot}}{S_{\text{eff}}}}, \tag{6.2}$$

where L is the luminosity and S_{eff} is the habitable zones stellar flux. The latter are defined as:

$$S_{\text{eff}} = S_{\text{eff},\odot} + aT_* + bT_*^2 + cT_*^3 + dT_*^4 \qquad \text{and} \qquad T_* = T_{\text{eff}} - 5780 \text{ K}. \tag{6.3}$$

The corresponding fluxes for the Sun, as well as the coefficients for the computation of the fluxes, are given in Table 6.6. Since all the data is already provided by the P-POP catalogue (as also reported in Appendix B), it is therefore possible to proceed with all the computations.

	Constants				
Case	$S_{\text{eff},\odot}$	a	b	c	d
Run. Green.	1.051	1.324×10^{-4}	1.541×10^{-8}	-7.989×10^{-12}	-1.832×10^{-15}
Run. Glac.	0.343	5.894×10^{-5}	1.655×10^{-9}	-3.005×10^{-12}	-5.293×10^{-16}

Table 6.6: Coefficients to be used in Equation 6.3 for the computation of habitable stellar fluxes and zones, adapted and extracted from Kopparapu et al., 2013[60] for both the runaway greenhouse (minimum limit) and runaway glaciation (maximum limit).

Figure 6.3 provides a summary of the main findings of this analysis. In particular, Figure 6.3a reports the extension of the habitable zones of every valid star in the catalogue (across all universes), divided by types, both in terms of local absolute distances (in astronomical units) and in terms of angular separation as seen from Earth. Whilst the latter is important in terms of resolution for interferometry, the real parameter of importance is the absolute distance. As already extensively discussed, M-type stars (red dwarfs) are the fainter stars (in this analysis) and therefore display a small habitable zone, limited to 0.5 AU. They have an extended angular separation range given their frequency in the closeness to Earth, providing.

K-type stars (orange dwarfs) have a wider range of absolute positions and, with respect to M stars, it can be noticed that the size of their habitable zones tends to increase

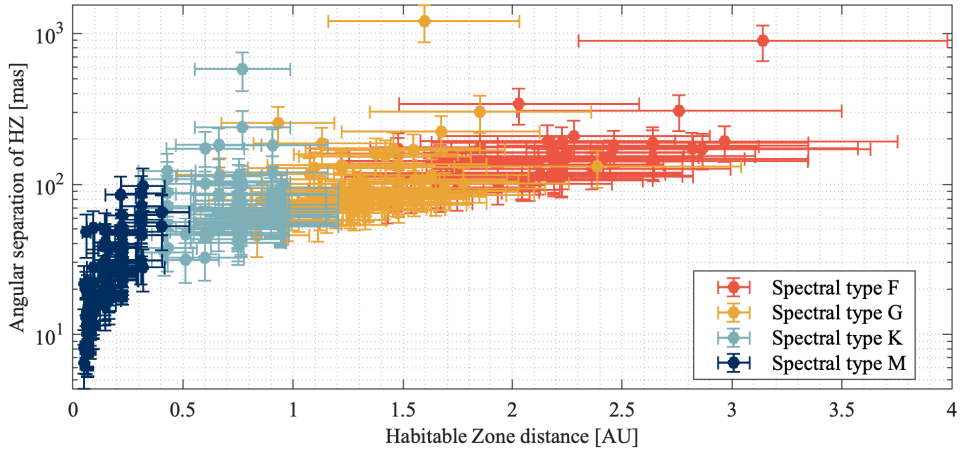

(a) Extension of the habitable zones (both in terms of absolute distances and angular separations) for each star of the catalogue.

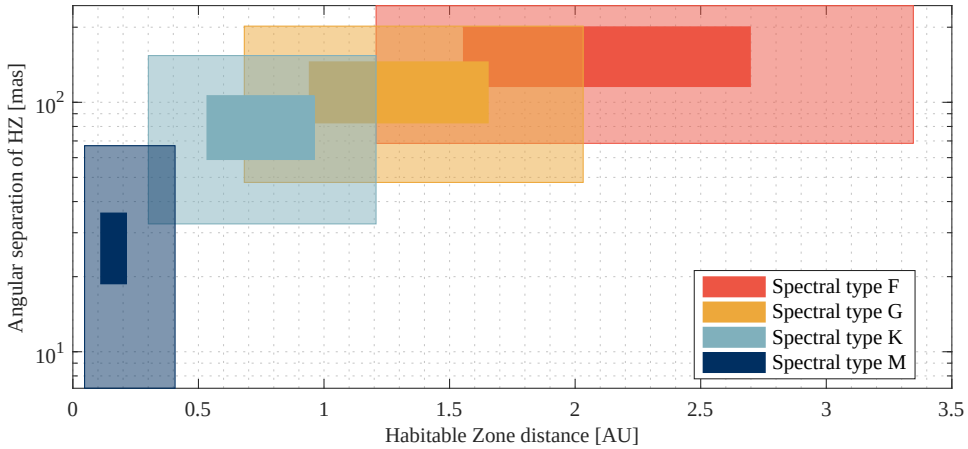

(b) Extension of the habitable zones (in terms of average values in solid colours and at respectively 10 and 90% percentiles in transparent colours) for four star types.

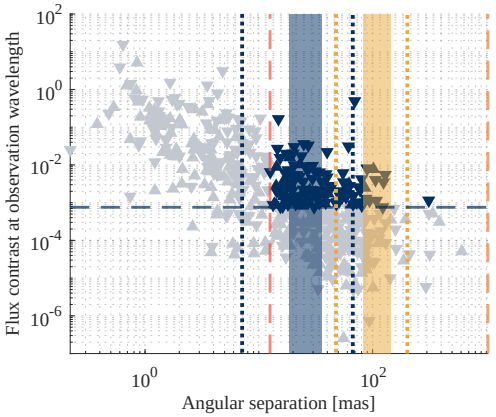

(c) Extension of the habitable zones (for types M and G only) in terms of angular separation with respect to the exoplanet yield of Darwin.

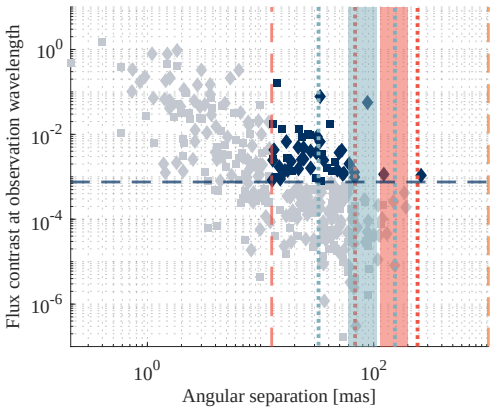

(d) Extension of the habitable zones (for types K and F only) in terms of angular separation with respect to the exoplanet yield of Darwin.

Figure 6.3: Impact of the habitable zones on the analysis of exoplanets yield. Figures 6.3c and 6.3d use the same colour scale and markers as all the previous images.

significantly, meaning that, locally, the search region is larger.

The trend continues with both G- and F-type stars, which have their habitable zones located at higher angular positions (and absolute distances). What can be concluded, essentially, is that there is a sort of inverse proportionality between the physical size and positions with respect to the angular separation distribution of the habitable zones.

This is more clear from Figure 6.3b, which visualises the average position for the runaway greenhouse and the runaway glaciation in solid colours. It is particularly evident that the M-type stars box is more vertically extended than the other ones, spanning larger angular separation distances, whilst being the least horizontally extended one.

In addition to the average values, the 10% percentile for the runaway greenhouse and the 90% percentile for the runaway glaciation are also represented in transparent colours. Whilst the distributions appear to be quite centred, it can be noticed that there is a slight tendency to present a further extended runaway glaciation than a runaway greenhouse.

Eventually, the key results of the analysis are finally given in Figures 6.3c and 6.3d for M-, G- and K-, F-type stars respectively (to avoid extended overlapping that would have crowded a single figure). In addition to that, the results are shown for a random universe and only for the exoplanets of the considered star types for each plot (the markers are the same as in all the other figures with exoplanet yields). The solid colour region represents the mean values, whilst the dotted region represents the 10-90% percentiles as in Figure 6.3b.

As can be seen, all the regions are within the inner and outer working angles, meaning that they can be resolved with Darwin at its maximum baseline (with the only exception of the 10% percentile line of M-type stars, which is instead outside the region). This is particularly remarkable because, as can be seen, especially for M- and G-type stars, the region of exoplanets that can be seen is particularly populated (as opposed to K and F stars, which would instead require higher integration times to shift the flux contrast to the higher range).

This ultimately answers the question that was at the base of the entire analysis: valid exoplanets can be seen and studied with the implementation of space-based nulling interferometry.

Conclusions

This work has introduced many concepts linked to nulling interferometry, highlighting both positive and negative aspects of its possible implementation. This final chapter wants to draw a general and complete conclusion linked to the main findings of this work.

Unique opportunities

Nulling interferometry stands as a unique method for direct exoplanet detection: not only is it more versatile than coronography, but it also offers advantages that alternatives cannot replicate. In particular, the model implemented in this work has achieved that space-based nulling interferometry offers:

- High angular resolution and contrast, as demonstrated through the extensive discussions on transmission maps, nulling ratio, and planet modulation efficiencies. This is true both for the ideal system and a realistically perturbed model, showing that in a deployment scenario, the instrument will be able to fulfil its role and behave as expected.

  This is particularly clear from results in Chapter 5 that show that, under the influence of the compensator, the instrument is able to reach considerable nulling ratios even under disturbances and, with the "minimum working example" in terms of baseline size considered in that chapter, is able to study, throughout its life, an average of 20 exoplanets.

- The capability to simulate realistic optical perturbations and incorporate compensators to recover performance. The analysis considered in Chapters 4 and 5 made use of extensive simulation data resulting from real-world existing tolerance values, later corrected with the aid of the compensator implemented through the bisection method, replicating the behaviour of the wavefront sensor on real hardware.

  As statistics have shown, the optical path difference improves by over 50%, going from the median value of 0.2 µm to 0.1 µm. More significantly, the maximum of the corrected distribution is below the median value of the uncorrected one, highlighting once more the potentiality of the instrument. The response function evaluated with the integration of the pupil plane integrated at different angular positions once more highlights the importance of a strong disturbance suppression, as the nulling power is rapidly lost, reducing the contrast.

- The validation through comparative mission analysis that shows the feasibility and potential scientific yield. The main findings of Chapter 6, coherent with the expected literature data, have shown that the array dimensions selected for the three missions are indeed the best possible, as Table 6.4 has shown that the inner working angle is a stronger and worse limit than the nulling ratio in the yields.

  The analysis has also shown that not only baselines in the order of those considered

for Darwin could ideally see hundreds of exoplanets (an average of 198 planets over 100 universes), but also that, on average, the habitable zones of F- to M-type stars are completely within the visibility window (with only the latter being partially exiting the limit).

Since the times of Darwin and TPF-I, the technological feasibility in light of maturing programmes has significantly advanced, thus making the future brighter for this kind of mission searching for biosignatures in a field that has yet a lot to offer in terms of possible breakthroughs.

A complex way forward: challenges to realisation

There are still many barriers that need to be addressed before making nulling interferometry a reality, that is to deploy such instruments into space.

There are technological constraints linked to formation flying precision and robustness, as addressed in the development of Darwin and TPF-I. There have been strong advancements in the TRL of many pivots, yet the deployment of a constellation is always extremely challenging in the sector. In addition to that, phase stability and control in optical path lengths must be ensured to be way below 5 µm when the wavelength is 10 µm. To grant that within a single branch is already challenging enough; if the possibility of small digressions in the global position or the orbital insertion of the different spacecraft were to be considered, the limitations that should be considered would be overwhelming.

In addition to that, as seen in Chapter 4, disturbances are not only due to internal sources (which can, at minimum, be mitigated), but also, and significantly, to instrumental stellar leakage, exozodiacal dust interference and off-axis suppression limitations. These effects cause a quantifiable degradation from phase errors, as also highlighted by the significant sensitivity coefficients values seen in Table 4.2. Once more, the risks of having too low nulling or contrast can be extremely catastrophic in terms of visible exoplanets that should be studied.

Once again, Chapter 6 showed the necessity of mission design trade-offs, with a strong preference for better inner working angles (that is, larger baselines and smaller aperture ratios) than nulling ratios (at least in static analysis). This is particularly challenging in an environment where large satellites require complex deployment mechanisms and strong disturbance suppressions, which, in turn, increase the complexity of the service module, with subsystems that must uphold the standards of high-precision pointing and stability.

Ultimately, the role of system engineering will be extremely challenging and fundamental in bringing such a mission to life, balancing tight and extreme scientific requirements with the availability of today's technology. Since ideally such an interferometer should operate from L_2 (to suppress the local zodiacal influence and sunlight), the road to its launch is still long and filled with challenges.

Next steps: beyond this work

The model that has been presented in this work has provided many interesting results and conclusions, yet many future integrations can be implemented to increase the complexity of the instrument.

First and foremost, many other disturbances can be included in the analysis, including thermal instabilities, polarisation errors and the presence of dynamic effects. Only a more detailed error representation, including orbital effects, can, for example, correctly establish

if the system is suitable for deployment and better compute the requirements that shall be granted to have a minimum working instrument. For example, the full line of sensitivity coefficients addressed in Section 4.2.5 have been left open for a wider implementation on the computation of the different sensitivity variables that are derived from a more refined mechanical model.

That is why a stronger integration with an experimental analysis could also be of particular high interest, offering a coupling with real optical systems or testbeds that can offer a higher degree of validation.

Ultimately, the introduction of mission-level considerations can offer strong refinements in terms of yield optimisation, target selection and stronger risk mitigation, as well as further analysis of different possible instruments that can be used in addition to the proposed interferometer. This work has proposed a foundational tool that can be integrated into future analysis.

Epilogue

In the broad horizons of the cosmos, the question of whether we are alone remains one of the most compelling scientific and philosophical pursuits of our time. Nulling interferometry is being built with a focus on listening for the faintest signals from distant worlds. This work contributes a small step toward that goal, offering an ensemble of tools to sharpen our vision. While the technological barriers are real, so too is the potential for discovery.

If one day we do find something—anything—it will be thanks to the interface between science, engineering and imagination, theory and curiosity. In that sense, every solution found, every compensated perturbation, is not just a technical success but a step closer to what we dream to find.

After all, science is the most human way of dreaming with our eyes open.

A Mathematical derivations

This chapter includes all the mathematical derivations that are deemed to be of interest in the discussion elaborated in the previous chapters.

A.1 Nulling ratio for a general interferometer

As reported in Section 3.7, the nulling ratio is defined as, in the common case where all the apertures behave the same way and have the same geometric characteristics:

$$G = \frac{N_g}{\sum_j^N N_{*,j}} \qquad \text{where:} \quad \begin{cases} N_g = 2A^2 \sum_j^N \sum_k^N F_* \dfrac{J_1\left(\frac{2\pi b_{jk}\vartheta_*}{\lambda}\right)}{\frac{2\pi b_{jk}\vartheta_*}{\lambda}} \cos\left(\varphi_j - \varphi_k\right) \\ \sum_j^N N_{*,j} = NA^2F_* \end{cases} . \tag{A.1}$$

The stellar brightness, in particular depends on the first kind first order Bessel function:

$$B^\star_{jk} = \frac{2F_\star\, J_1\left(\frac{2\pi\, b_{jk}\,\theta_\star}{\lambda}\right)}{2\pi\, b_{jk}\,\theta_\star/\lambda}. \tag{A.2}$$

When $j = k$ (that is, when the baseline is zero) caution must be taken by considering the limit as for the properties of the Bessel functions, leading to a simplified expression for the self-convolution term:

$$J_1(x) \sim \frac{x}{2} \quad \text{for } x \to 0 \qquad \Rightarrow \qquad B^\star_{jj} = F_\star. \tag{A.3}$$

The nulling ratio is, therefore:

$$G = \frac{N_g}{N\,F_\star A^2} = \frac{1}{N}\sum_{j,k=1}^{N} \cos(\phi_j - \phi_k)\,\frac{B^\star_{jk}}{F_\star}\,. \tag{A.4}$$

Splitting the sum into the diagonal ($j = k$) and off-diagonal ($j \neq k$) parts:

- **Diagonal terms:** For $j = k$:

$$\frac{B^\star_{jj}}{F_\star} = 1 \quad \text{and} \quad \cos(\phi_j - \phi_j) = 1. \tag{A.5}$$

- **Off-diagonal terms:** For $j \neq k$ the situation is unchanged:

$$\frac{B^\star_{jk}}{F_\star} = \frac{2J_1\left(\frac{2\pi\, b_{jk}\,\theta_\star}{\lambda}\right)}{2\pi\, b_{jk}\,\theta_\star/\lambda}. \tag{A.6}$$

Therefore, in the end:

$$G = \frac{1}{N}\left[N + \sum_{j\neq k} \cos(\phi_j - \phi_k)\, \frac{2J_1\left(\frac{2\pi\, b_{jk}\, \theta_\star}{\lambda}\right)}{2\pi\, b_{jk}\, \theta_\star/\lambda}\right]. \tag{A.7}$$

A.2 Approximate relations for instrumental leakage

The general response function for an N-aperture interferometer is given by:

$$R = \frac{1}{2}\sum_{j=1}^{N}\sum_{k=1}^{N} A_j(1+\delta A_j)A_k(1+\delta A_k)\cos\left(\Delta\Phi_{jk} + \Delta\delta\Phi_{jk}\right). \tag{A.8}$$

For a general two apertures interferometer this reduces to:

$$\begin{aligned} R = \frac{1}{2}\Big[& A_1^2(1+2\delta A_1+\delta A_1^2) + A_2^2(1+2\delta A_2+\delta A_2^2) \\ & + 2A_1A_2(1+\delta A_1+\delta A_2+\delta A_1\delta A_2)\cos\left(\Delta\Phi_{12}+\Delta\delta\Phi_{12}\right)\Big]. \end{aligned} \tag{A.9}$$

A.2.1 Phase Error

Expanding the cosine sum and using the known limit $\sin x \to x$ for small values of x:

$$\cos(\Delta\Phi_{12}+\Delta\delta\Phi_{12}) \approx \cos\Delta\Phi_{12} - \Delta\delta\Phi_{12}\sin\Delta\Phi_{12} - \frac{1}{2}(\Delta\delta\Phi_{12})^2\cos\Delta\Phi_{12}, \tag{A.10}$$

Under nulling conditions where $\Delta\Phi_{12} = \pi$, then $\cos\pi = -1$ and $\sin\pi = 0$, so the linear term vanishes, leading to:

$$\cos(\pi+\Delta\delta\Phi_{12}) \approx -1 - \frac{1}{2}(\Delta\delta\Phi_{12})^2 \qquad \Rightarrow \qquad R \approx \frac{1}{2}A_1A_2\left(-1-\frac{1}{2}(\Delta\delta\Phi_{12})^2\right). \tag{A.11}$$

Since we are interested in the on-axis transmission, we focus on the deviation from perfect nulling:

$$R(0,0) \approx \frac{1}{2}A_1A_2\cdot\left(-\frac{1}{2}(\Delta\delta\Phi_{12})^2\right). \tag{A.12}$$

Rearranging and taking unitary apertures, the desired expression is found:

$$R(0,0) = \frac{\Delta\phi^2}{4}. \tag{A.13}$$

A.2.2 Wavefront Error

The phase variance over each pupil leads to a mismatch between beams, resulting in, directly from the previous derived expression:

$$R(0,0) = \frac{1}{4}(\sigma_{\phi_1}^2 + \sigma_{\phi_2}^2). \tag{A.14}$$

A.2.3 Intensity Error

An imbalance in intensity between the two arms leads to an additional non-null contribution. Let the relative intensity mismatch be defined as:

$$\Delta I = \frac{A_2 - A_1}{A_1 + A_2}. \tag{A.15}$$

Expanding the intensity terms in the response function, assuming $A_2 = A_1(1+\Delta I)$:

$$R = \frac{1}{2}A_1 A_2 \cos(\pi) = \frac{1}{2}A_1 A_2(-1) \ = -\frac{1}{2}A_1^2(1+\Delta I). \tag{A.16}$$

The deviation from perfect nulling comes from the quadratic term in ΔI:

$$R(0,0) = \frac{A_1^2}{2}\left(-1 + \frac{\Delta I^2}{2}\right). \tag{A.17}$$

Since the perfect null term cancels, it is found:

$$R(0,0) = \frac{\Delta I^2}{16}. \tag{A.18}$$

A.2.4 Polarisation Error

Differential phase shift and rotation contribute to the errors as phase errors, leading to the found expression:

$$R(0,0) = \frac{1}{4}(\Delta\phi_{s-p}^2 + \alpha_{rot}^2). \tag{A.19}$$

A.3 Period associated to the nulling ratio

As Equation 3.20 affirms, the nulling ratio depends on the phase difference between all the considered branches; let us consider only two apertures for brevity and assuming that the former has a little imbalance in its optical path (so that OPD $= x$):

$$G \propto \sum_{j \neq k} \cos\left(\varphi_j - \varphi_k\right) \qquad \text{where:} \qquad \begin{cases} \varphi_1 = \Phi_1 + \frac{2\pi(\Lambda + x)}{\lambda} \\ \varphi_2 = \Phi_2 + \frac{2\pi(\Lambda)}{\lambda} \end{cases}. \tag{A.20}$$

By replacing and knowing that the cosine as a 2π period, one finds that:

$$\cos\left(\frac{2\pi x}{\lambda} + \Phi_1 - \Phi_2\right) = \cos\left(\frac{2\pi(x+T)}{\lambda} + \Phi_1 - \Phi_2\right). \tag{A.21}$$

By focusing on the arguments and simplifying:

$$\frac{2\pi(x+T)}{\lambda} = \frac{2\pi x}{\lambda} + 2\pi k, \quad k \in \mathbb{Z} \quad \Rightarrow \quad \frac{2\pi T}{\lambda} = 2\pi k. \tag{A.22}$$

The first repetition is found for $k = 1$, therefore proving that the nulling ratio is periodic in the wavelength:

$$T = \lambda. \tag{A.23}$$

A.3.1 Derivative of the Bessel's function

Making use of the properties of the derivative of the first kind of Bessel's functions[23], it is found that:

$$\frac{dJ_n}{dx} = \frac{1}{2}\left[J_{n-1}(x) - J_{n+1}(x)\right]. \tag{A.24}$$

Making use of the chain rule in the derivation, one finds:

$$\frac{\partial B_{*,jk}}{\partial x_j} = \frac{\partial B_{*,jk}}{\partial b_{jk}}\frac{\partial b_{jk}}{\partial x_j} \qquad \Rightarrow \qquad \begin{cases} \frac{\partial b_{jk}}{\partial x_j} = \frac{x_j}{\sqrt{x_j^2+y_j^2}} \\ \frac{\partial B_{*,jk}}{\partial b_{jk}} = \frac{2F_*}{\left(\frac{2\pi b_{jk}\vartheta_*}{\lambda}\right)^2}\left[\frac{1}{2}\frac{2\pi\vartheta_*}{\lambda}\left(J_0 - J_2\right) - \frac{2\pi b_{jk}\vartheta_*}{\lambda}J_1\right] \end{cases}. \tag{A.25}$$

Using the recurrence relation on the Bessel's functions:

$$J_{n-1}(z) + J_{n+1}(z) = \frac{2n}{z}J_n(z) \qquad \text{for } n = 1: \quad J_0(z) + J_2(z) = \frac{2}{z}J_1(z). \tag{A.26}$$

Therefore, the relation simplifies to the shown form:

$$\frac{\partial B_{*,jk}}{\partial x_j} = -2x_j F_* \frac{J_2\left(\frac{2\pi b_{jk}\vartheta_*}{\lambda}\right)}{b_{jk}^2}. \tag{A.27}$$

B Synthetic exoplanet populations with the P-Pop catalogue

Up to April 2025, more 5876 exoplanets have been discovered (mainly by NASA's Kepler mission) and 7576 are other possible candidates that require more studies[84], therefore, at first, the need of a statistical instrument to generate exoplanets may seem not motivated, given the available amount of data.

However, despite the success of the Kepler mission, its critical failure in 2013 has severely limited the yield of results, limiting the search field to a very small research area[46]. Therefore, a statistical instrument based on a Monte Carlo simulation to generate test populations of exoplanets has been created to study possible yields of future instruments[53].

B.1 Overview of the tool

The P-POP generating tool is a statistical Monte Carlo tools based around the generation of 2000 systems around 326 nearby stars (i.e. closer than 20 pc) from selectable catalogues that have been filtered for distance, type and declination range[53].

Depending on the spectral type of the star, a different occurrence model for exoplanets (in terms of size and distance from its host) can be used based on statistical distributions based on previous works[10],[35],[53]. While eccentricities can be considered circular in most case, random orientations and orbital phases can be assumed; mass is estimated using a forecaster model[14],[52], albedo is uniformly sampled and exozodiacal dust can be optionally included in the model[53].

B.2 Output of the tool

The tool generates a table where each row represents an exoplanet and its defining characteristics, including stellar properties, orbital elements, physical characteristics and flux definitions, enabling a quantitative yield predictions based on instrumental performance, as studied by the two authors themselves for a mid-infrared interferometer[53].

This model has been used-exploiting the already generated populations by Kammerer and Quanz[53]-to simulate the yield of the example configurations used in this work to provide a general consideration on the obtainable yields of mid-infrared nulling interferometers: while NASA provides an extensive catalogue of exoplanets[84], due to the lack of inferred data, especially on the planets found close to their host stars (which are the desired target of this analysis), the results provided by this catalogue alone where not meaningful enough to validate the tool (out of the 5876 discovered exoplanets, only 1326 presents all the necessary fields, out of which around a thousand are larger than thrice the Earth,

making them not of particular interest in astrobiology).

Type	Variable		Description
	Name	Unit	
Simulation	`Nuniverse`	-	Simulation associated to the planet
Planet data	`Rp`	$R_\oplus$	Planetary radius
	`Porb`	d	Orbital period of the planet
	`Mp`	$M_\oplus$	Planet mass
	`ep`	-	Orbital eccentricity of the planet
	`ip`	rad	Orbital inclination of the planet
	`Omegap`	rad	Longitude of ascending node
	`omegap`	rad	Argument of periapsis
	`thetap`	rad	True anomaly of the planet
	`Abond`	-	Bond albedo of the planet
	`AgeomVIS`	-	Geometric albedo in the visible range
	`AgeomMIR`	-	Geometric albedo in the mid-infrared
Planet-star relation	`z`	-	Level of exozodiacal dust
	`ap`	AU	Semi-major axis of the planetary orbit
	`rp`	AU	Planet's physical separation from the star
	`AngSep`	arcsec	Projected angular separation of the planet
	`maxAngSep`	arcsec	Maximum projected angular separation
	`Fp`	$S_\oplus$	Incident flux from host star
	`fp`	-	Lambertian reflectance of the planet
	`Tp`	K	Equilibrium temperature of the planet
Star data	`Nstar`	-	Identifier number for the host star
	`Rs`	$R_\odot$	Radius of the host star
	`Ms`	$M_\odot$	Mass of the host star
	`Ts`	K	Effective temperature of the host star
	`Ds`	pc	Distance to the host star
	`Stype`	-	Spectral type of the host star
System	`RA`	deg	Right ascension of the host star
	`Dec`	deg	Declination of the host star
	`lGal`	deg	Galactic longitude of the host star
	`bGal`	deg	Galactic latitude of the host star

Table B.1: Parameter descriptions for simulated planetary populations from P-POP[52], including planetary and stellar characteristics used in modelling and observation simulations.

Table B.1 provides a summary of the elements provided by the P-POP simulation tools, a portion of which has been used in this work.

Bibliography

[1] O. Absil et al. 'Performance study of ground-based infrared Bracewell interferometers - Application to the detection of exozodiacal dust disks with GENIE'. In: (2005). DOI: 10.48550/ARXIV.ASTRO-PH/0511223. URL: https://arxiv.org/abs/astro-ph/0511223 (visited on 19/05/2025).

[2] Olivier Absil. 'Astrophysical studies of extrasolar planetary systems using infrared interferometric techniques'. PhD thesis. 2006. URL: https://theses.hal.science/tel-00124720v1/file/Absil06_thesis.pdf.

[3] Olivier Absil. 'Nulling Interferometry with IRSI-Darwin: Detection and Characterization of Earth-like Exoplanets'. In: (2001).

[4] J. R. P. Angel and N. J. Woolf. 'An Imaging Nulling Interferometer to Study Extrasolar Planets'. In: *The Astrophysical Journal* 475.1 (20th Jan. 1997), pp. 373–379. ISSN: 0004-637X, 1538-4357. DOI: 10.1086/303529. URL: https://iopscience.iop.org/article/10.1086/303529 (visited on 28/09/2024).

[5] arianegroup. *Ariane 6 User's Manual (Issue 2, revision 0)*. Feb. 2021. URL: https://ariane.group/app/uploads/sites/4/2024/10/Mua-6_Issue-2_Revision-0_March-2021.pdf.

[6] J.-P. Berger et al. 'Integrated optics for astronomical interferometry. II. First laboratory white-light interferograms'. In: *Astronomy and Astrophysics Supplement Series* 139.1 (Oct. 1999), pp. 173–177. ISSN: 0365-0138, 1286-4846. DOI: 10.1051/aas:1999504. arXiv: astro-ph/9907032. URL: http://arxiv.org/abs/astro-ph/9907032 (visited on 11/03/2025).

[7] Antonin H. Bouchez et al. 'The Giant Magellan Telescope adaptive optics program'. In: SPIE Astronomical Telescopes + Instrumentation. Ed. by Enrico Marchetti, Laird M. Close and Jean-Pierre Véran. Montréal, Quebec, Canada, 21st July 2014, 91480W. DOI: 10.1117/12.2057613. URL: http://proceedings.spiedigitallibrary.org/proceeding.aspx?doi=10.1117/12.2057613 (visited on 07/02/2025).

[8] R. N. Bracewell. 'Detecting nonsolar planets by spinning infrared interferometer'. In: *Nature* 274.5673 (Aug. 1978), pp. 780–781. ISSN: 0028-0836, 1476-4687. DOI: 10.1038/274780a0. URL: https://www.nature.com/articles/274780a0 (visited on 16/05/2025).

[9] Robert A. Brown. 'Obscurational Completeness'. In: *The Astrophysical Journal* 607.2 (June 2004), pp. 1003–1013. ISSN: 0004-637X, 1538-4357. DOI: 10.1086/383586. URL: https://iopscience.iop.org/article/10.1086/383586 (visited on 14/03/2025).

[10] Christopher J. Burke et al. 'Terrestrial Planet Occurrence Rates for the *Kepler* Gk Dwarf Sample'. In: *The Astrophysical Journal* 809.1 (4th Aug. 2015), p. 8. ISSN: 1538-4357. DOI: 10.1088/0004-637X/809/1/8. URL: https://iopscience.iop.org/article/10.1088/0004-637X/809/1/8 (visited on 22/04/2025).

[11] Remo Burn et al. 'A radius valley between migrated steam worlds and evaporated rocky cores'. In: *Nature Astronomy* 8.4 (9th Feb. 2024), pp. 463–471. ISSN: 2397-3366. DOI: 10.1038/s41550-023-02183-7. URL: https://www.nature.com/articles/s41550-023-02183-7 (visited on 16/05/2025).

[12] Manuel Cagigal and Vidal Canales. 'Exoplanet detection using a nulling interferometer'. In: *Optics Express* 9.1 (2nd July 2001), p. 36. ISSN: 1094-4087. DOI: 10.1364/OE.9.000036. URL: https://opg.optica.org/oe/abstract.cfm?uri=oe-9-1-36 (visited on 19/05/2025).

[13] Claudia Carboni. 'Opto-mechanical design of a 4 apertures nulling interferometer'. thesis. Université de Liège, 2025.

[14] Jingjing Chen and David Kipping. 'Probabilistic Forecasting of the Masses and Radii of Other Worlds'. In: *The Astrophysical Journal* 834.1 (1st Jan. 2017), p. 17. ISSN: 0004-637X, 1538-4357. DOI: 10.3847/1538-4357/834/1/17. URL: https://iopscience.iop.org/article/10.3847/1538-4357/834/1/17 (visited on 22/04/2025).

[15] Charles S. Cockell et al. 'Darwin—an experimental astronomy mission to search for extrasolar planets'. In: *Experimental Astronomy* 23.1 (Mar. 2009), pp. 435–461. ISSN: 0922-6435, 1572-9508. DOI: 10.1007/s10686-008-9121-x. URL: http://link.springer.com/10.1007/s10686-008-9121-x (visited on 09/05/2025).

[16] M. M. Colavita et al. 'The Keck Interferometer'. In: *Publications of the Astronomical Society of the Pacific* 125.932 (Oct. 2013), pp. 1226–1264. ISSN: 00046280, 15383873. DOI: 10.1086/673475. URL: http://iopscience.iop.org/article/10.1086/673475 (visited on 12/03/2025).

[17] Consortium by TU Delft, KU Leuven and Centre Spatial de Liège. *TN2- ESA nulling interferometry - Technology review and trade-off analysis*. 2024.

[18] Luigi d'Arcio et al. 'Search for extraterrestrial planets: the DARWIN mission'. In: *International Conference on Space Optics — ICSO 2006*. International Conference on Space Optics 2006. Ed. by Errico Armandillo, Josiane Costeraste and Nikos Karafolas. Noordwijk, Netherlands: SPIE, 2006, p. 121. ISBN: 978-1-5106-1623-3 978-1-5106-1624-0. DOI: 10.1117/12.2308153. URL: https://www.spiedigitallibrary.org/conference-proceedings-of-spie/10567/2308153/Search-for-extraterrestrial-planets-the-DARWIN-mission/10.1117/12.2308153.full (visited on 24/02/2025).

[19] W. C. Danchi et al. 'The Importance of Phase in Nulling Interferometry and a Three-Telescope Closure-Phase Nulling Interferometer Concept'. In: *The Astrophysical Journal* 645.2 (10th July 2006), pp. 1554–1559. ISSN: 0004-637X, 1538-4357. DOI: 10.1086/504511. URL: https://iopscience.iop.org/article/10.1086/504511 (visited on 23/02/2025).

[20] Colin Dandumont. 'Exoplanet detection yield with nulling interferometry'. PhD thesis. University of Liège.

[21] Colin Dandumont et al. 'Exoplanet detection yield of a space-based Bracewell interferometer from small to medium satellites'. In: *Journal of Astronomical Telescopes, Instruments, and Systems* 6.3 (23rd Sept. 2020). ISSN: 2329-4124. DOI: 10.1117/1.JATIS.6.3.035004. URL: https://www.spiedigitallibrary.org/journals/Journal-of-Astronomical-Telescopes-Instruments-and-Systems/volume-6/issue-03/035004/Exoplanet-detection-yield-of-a-space-based-Bracewell-interferometer-from/10.1117/1.JATIS.6.3.035004.full (visited on 23/02/2025).

[22] Felix A. Dannert et al. 'Large Interferometer For Exoplanets (LIFE): II. Signal simulation, signal extraction, and fundamental exoplanet parameters from single-epoch observations'. In: *Astronomy & Astrophysics* 664 (Aug. 2022), A22. ISSN: 0004-6361, 1432-0746. DOI: 10.1051/0004-6361/202141958. URL: https://www.aanda.org/10.1051/0004-6361/202141958 (visited on 06/02/2025).

[23] Joella Deal. 'Basics of Bessel Functions'. PhD thesis. Portland State University, 26th May 2018. DOI: 10.15760/honors.552. URL: http://archives.pdx.edu/ds/psu/25251 (visited on 21/02/2025).

[24] D Defrere et al. 'Update on the LBTI: a versatile high-contrast and high-resolution infrared imager for a 23-m telescope'. In: ().

[25] Denis Defrère. 'Characterizing extrasolar planetary systems using infrared interferometry'. PhD thesis. 2009.

[26] Denis Defrère et al. 'L-band nulling interferometry at the VLTI with Asgard/NOTT: status and plans'. In: *Optical and Infrared Interferometry and Imaging IX*. Optical and Infrared Interferometry and Imaging IX. Ed. by Stephanie Sallum, Joel Sanchez-Bermudez and Jens Kammerer. Yokohama, Japan: SPIE, 28th Aug. 2024, p. 14. ISBN: 978-1-5106-7513-1 978-1-5106-7514-8. DOI: 10.1117/12.3019922. URL: https://www.spiedigitallibrary.org/conference-proceedings-of-spie/13095/3019922/L-band-nulling-interferometry-at-the-VLTI-with-Asgard-NOTT/10.1117/12.3019922.full (visited on 12/03/2025).

[27] David W. Draper et al. 'Planet Signal Extraction for the *Terrestrial Planet Finder* Interferometer'. In: *The Astronomical Journal* 131.3 (Mar. 2006), pp. 1822–1836. ISSN: 0004-6256, 1538-3881. DOI: 10.1086/499528. URL: https://iopscience.iop.org/article/10.1086/499528 (visited on 25/03/2025).

[28] Samridhi Dwivedi and Suresh Chandra. 'Quantitative study of habitability of various classes of exoplanets'. In: *Advances in Space Research* (May 2025), S0273117725004776. ISSN: 02731177. DOI: 10.1016/j.asr.2025.05.019. URL: https://linkinghub.elsevier.com/retrieve/pii/S0273117725004776 (visited on 16/05/2025).

[29] Frank Eisenhauer, John D. Monnier and Oliver Pfuhl. 'Advances in Optical/Infrared Interferometry'. In: *Annual Review of Astronomy and Astrophysics* 61.1 (18th Aug. 2023), pp. 237–285. ISSN: 0066-4146, 1545-4282. DOI: 10.1146/annurev-astro-121622-045019. URL: https://www.annualreviews.org/content/journals/10.1146/annurev-astro-121622-045019 (visited on 25/02/2025).

[30] European Space Agency. *Darwin factsheet*. Science & Exploration. URL: https://www.esa.int/Science_Exploration/Space_Science/Darwin_factsheet.

[31] European Space Agency. *Exoplanets in the spotlight*. URL: https://www.esa.int/Science_Exploration/Space_Science/Exoplanets/Exoplanets_in_the_spotlight.

[32] *European Space Observatory (ESO). The Very Large Telescope Interferometer*. URL: https://www.eso.org/sci/facilities/paranal/telescopes/vlti.html.

[33] Europeans Southern Observqtory. *ELT Instruments: METIS*. URL: https://elt.eso.org/instrument/METIS/ (visited on 12/03/2025).

[34] Reinhold Flatscher et al. 'DARWIN nulling interferometer breadboard I: System engineering and measurements'. In: Earths: DARWIN/TPF and the Search for Extrasolar Terrestrial Planets. Vol. 539. 1st Oct. 2003, pp. 283–291. URL: https://ui.adsabs.harvard.edu/abs/2003ESASP.539..283F (visited on 14/05/2025).

[35] François Fressin et al. 'The False Positive Rate of *Kepler* and the Occurrence of Planets'. In: *The Astrophysical Journal* 766.2 (12th Mar. 2013), p. 81. ISSN: 0004-637X, 1538-4357. DOI: 10.1088/0004-637X/766/2/81. URL: https://iopscience.iop.org/article/10.1088/0004-637X/766/2/81 (visited on 22/04/2025).

[36] C V M Fridlund. 'Darwin – The Infrared Space Interferometry Mission'. In: (2000).

[37] C.V.M Fridlund. 'The Darwin mission'. In: *Advances in Space Research* 34.3 (Jan. 2004), pp. 613–617. ISSN: 02731177. DOI: 10.1016/j.asr.2003.05.031. URL: https://linkinghub.elsevier.com/retrieve/pii/S0273117703011955 (visited on 24/02/2025).

[38] Jonathan P. Gardner et al. 'The James Webb Space Telescope'. In: *Space Science Reviews* 123.4 (Apr. 2006), pp. 485–606. ISSN: 0038-6308, 1572-9672. DOI: 10.1007/s11214-006-8315-7. URL: https://link.springer.com/10.1007/s11214-006-8315-7 (visited on 07/02/2025).

[39] Germain Garreau et al. 'Asgard/NOTT: L-band nulling interferometry at the VLTI. II. Warm optical design and injection system'. In: *Journal of Astronomical Telescopes, Instruments, and Systems* 10.1 (15th Feb. 2024). ISSN: 2329-4124. DOI: 10.1117/1.JATIS.10.1.015002. URL: https://www.spiedigitallibrary.org/journals/Journal-of-Astronomical-Telescopes-Instruments-and-Systems/volume-10/issue-01/015002/Asgard-NOTT--L-band-nulling-interferometry-at-the-VLTI/10.1117/1.JATIS.10.1.015002.full (visited on 12/03/2025).

[40] Steven Giacalone and Courtney D. Dressing. 'Small and Close-In Planets are Uncommon Around A-type Stars'. In: (2024). DOI: 10.48550/ARXIV.2411.13363. URL: https://arxiv.org/abs/2411.13363 (visited on 16/05/2025).

[41] Cedric Gillmann et al. 'Interior Controls on the Habitability of Rocky Planets'. In: *Space: Science & Technology* 4 (Jan. 2024), p. 0075. ISSN: 2692-7659. DOI: 10.34133/space.0075. URL: https://spj.science.org/doi/10.34133/space.0075 (visited on 16/05/2025).

[42] Adrian M. Glauser et al. 'The Large Interferometer For Exoplanets (LIFE): a space mission for mid-infrared nulling interferometry'. In: *Optical and Infrared Interferometry and Imaging IX*. Optical and Infrared Interferometry and Imaging IX. Ed. by Stephanie Sallum, Joel Sanchez-Bermudez and Jens Kammerer. Yokohama, Japan: SPIE, 28th Aug. 2024, p. 48. ISBN: 978-1-5106-7513-1 978-1-5106-7514-8. DOI: 10.1117/12.3019090. URL: https://www.spiedigitallibrary.org/conference-proceedings-of-spie/13095/3019090/The-Large-Interferometer-For-Exoplanets-LIFE--a-space-mission/10.1117/12.3019090.full (visited on 25/02/2025).

[43] A. Glindemann et al. 'The VLTI — A Status Report'. In: *Astrophysics and Space Science* 286.1 (2003), pp. 35–44. ISSN: 0004640X. DOI: 10.1023/A:1026145709077. URL: http://link.springer.com/10.1023/A:1026145709077 (visited on 24/02/2025).

[44] Olivier Guyon et al. 'Optimal beam combiner design for nulling interferometers'. In: *Publications of the Astronomical Society of the Pacific* 125.930 (Aug. 2013), pp. 951–965. ISSN: 00046280, 15383873. DOI: 10.1086/671816. arXiv: 1306.0179[astro-ph]. URL: http://arxiv.org/abs/1306.0179 (visited on 07/02/2025).

[45] Jonah T. Hansen, Michael J. Ireland and the LIFE Collaboration. 'Large Interferometer For Exoplanets (LIFE): IV. Ideal kernel-nulling array architectures for a space-based mid-infrared nulling interferometer'. In: *Astronomy & Astrophysics* 664 (Aug. 2022), A52. ISSN: 0004-6361, 1432-0746. DOI: 10.1051/0004-6361/202243107. URL: https://www.aanda.org/10.1051/0004-6361/202243107 (visited on 09/05/2025).

[46] J.D. Harrington. 'NASA Ends Attempts to Fully Recover Kepler Spacecraft, Potential New Missions Considered'. In: (15th Aug. 2013). URL: https://www.nasa.gov/news-release/nasa-ends-attempts-to-fully-recover-kepler-spacecraft-potential-new-missions-considered/.

[47] Eugene Hecht. *Optics*. 5 edition. Global edition. Boston: Pearson Education, Inc, 2017. 1 p. ISBN: 978-0-13-397722-6 978-1-292-09696-4.

[48] Oliver Herbort et al. 'Habitability constraints by nutrient availability in atmospheres of rocky exoplanets'. In: *International Journal of Astrobiology* 23 (2024), e12. ISSN: 1473-5504, 1475-3006. DOI: 10.1017/S1473550424000077. URL: https://www.cambridge.org/core/product/identifier/S1473550424000077/type/journal_article (visited on 16/05/2025).

[49] P. M. Hinz et al. 'Overview of LBTI: a multipurpose facility for high spatial resolution observations'. In: SPIE Astronomical Telescopes + Instrumentation. Ed. by Fabien Malbet, Michelle J. Creech-Eakman and Peter G. Tuthill. Edinburgh, United Kingdom, 4th Aug. 2016, p. 990704. DOI: 10.1117/12.2233795. URL: http://proceedings.spiedigitallibrary.org/proceeding.aspx?doi=10.1117/12.2233795 (visited on 24/02/2025).

[50] Philip M. Hinz et al. 'Status of the LBT interferometer'. In: SPIE Astronomical Telescopes + Instrumentation. Marseille, France, 14th July 2008, p. 701328. DOI: 10.1117/12.790211. URL: http://proceedings.spiedigitallibrary.org/proceeding.aspx?doi=10.1117/12.790211 (visited on 24/02/2025).

[51] Brian Jackson, Rory Barnes and Richard Greenberg. 'Tidal Heating of Terrestrial Extra-Solar Planets and Implications for their Habitability'. In: (2008). DOI: 10.48550/ARXIV.0808.2770. URL: https://arxiv.org/abs/0808.2770 (visited on 16/05/2025).

[52] J. Kammerer, S. P. Quanz and E. Fontanet. 'P-pop user documentation'. In: *Astronomy & Astrophysics* (2021).

[53] Jens Kammerer and Sascha P. Quanz. 'Simulating the exoplanet yield of a space-based mid-infrared interferometer based on *Kepler* statistics'. In: *Astronomy & Astrophysics* 609 (Jan. 2018), A4. ISSN: 0004-6361, 1432-0746. DOI: 10.1051/0004-6361/201731254. URL: https://www.aanda.org/10.1051/0004-6361/201731254 (visited on 18/04/2025).

[54] Hannu Karttunen et al., eds. *Fundamental Astronomy*. Berlin, Heidelberg: Springer Berlin Heidelberg, 2017. ISBN: 978-3-662-53044-3 978-3-662-53045-0. DOI: 10.1007/978-3-662-53045-0. URL: http://link.springer.com/10.1007/978-3-662-53045-0 (visited on 06/02/2025).

[55] *Keck Telescope and Facility Instrument Guide*. URL: https://www2.keck.hawaii.edu/observing/kecktelgde/ktelinstupdate.pdf.

[56] T. Kelsall et al. 'The *COBE* Diffuse Infrared Background Experiment Search for the Cosmic Infrared Background. II. Model of the Interplanetary Dust Cloud'. In: *The Astrophysical Journal* 508.1 (20th Nov. 1998), pp. 44–73. ISSN: 0004-637X, 1538-4357. DOI: 10.1086/306380. URL: https://iopscience.iop.org/article/10.1086/306380 (visited on 21/02/2025).

[57] Chris Kitchin. *Exoplanets*. Astronomers' Universe. New York, NY: Springer New York, 2012. ISBN: 978-1-4614-0643-3 978-1-4614-0644-0. DOI: 10.1007/978-1-4614-0644-0. URL: http://link.springer.com/10.1007/978-1-4614-0644-0 (visited on 06/02/2025).

[58] B. S. Konrad et al. 'Large Interferometer For Exoplanets (LIFE): III. Spectral resolution, wavelength range, and sensitivity requirements based on atmospheric retrieval analyses of an exo-Earth'. In: *Astronomy & Astrophysics* 664 (Aug. 2022), A23. ISSN: 0004-6361, 1432-0746. DOI: 10.1051/0004-6361/202141964. URL: https://www.aanda.org/10.1051/0004-6361/202141964 (visited on 12/03/2025).

[59] Ravi Kumar Kopparapu et al. 'Exoplanet Classification and Yield Estimates for Direct Imaging Missions'. In: *The Astrophysical Journal* 856.2 (1st Apr. 2018), p. 122. ISSN: 0004-637X, 1538-4357. DOI: 10.3847/1538-4357/aab205. URL: https://iopscience.iop.org/article/10.3847/1538-4357/aab205 (visited on 09/05/2025).

[60] Ravi Kumar Kopparapu et al. 'Habitable zones around main-sequence stars: new estimates'. In: *The Astrophysical Journal* 765.2 (26th Feb. 2013), p. 131. ISSN: 0004-637X, 1538-4357. DOI: 10.1088/0004-637X/765/2/131. URL: https://iopscience.iop.org/article/10.1088/0004-637X/765/2/131 (visited on 19/05/2025).

[61] Romain Laugier, Nick Cvetojevic and Frantz Martinache. 'Kernel nullers for an arbitrary number of apertures'. In: *Astronomy & Astrophysics* 642 (Oct. 2020), A202. ISSN: 0004-6361, 1432-0746. DOI: 10.1051/0004-6361/202038866. arXiv: 2008.07920[astro-ph]. URL: http://arxiv.org/abs/2008.07920 (visited on 23/02/2025).

[62] P R Lawson et al. 'Terrestrial Planet Finder Interferometer (TPF-I)'. In: (31st Mar. 2009).

[63] Peter R Lawson and Jennifer A Dooley. 'Technology Plan for the Terrestrial Planet Finder Interferometer'. In: (June 2005).

[64] Peter R. Lawson. *Principles of Long Baseline Stellar Interferometry*.

[65] Oliver P Lay. 'Imaging properties of rotating nulling interferometers'. In: (2005).

[66] Oliver P Lay. 'Systematic errors in nulling interferometers'. In: (2004).

[67] Oliver P. Lay. 'Removing instability noise in nulling interferometers'. In: SPIE Astronomical Telescopes + Instrumentation. Ed. by John D. Monnier, Markus Schöller and William C. Danchi. Orlando, Florida , USA, 14th June 2006, 62681A. DOI: 10.1117/12.670603. URL: http://proceedings.spiedigitallibrary.org/proceeding.aspx?doi=10.1117/12.670603 (visited on 14/05/2025).

[68] Oliver P. Lay and Serge Dubovitsky. 'Nulling interferometers: the importance of systematic errors and the X-array configuration'. In: SPIE Astronomical Telescopes + Instrumentation. Ed. by Wesley A. Traub. USA, 20th Oct. 2004, p. 874. DOI: 10.1117/12.552109. URL: http://proceedings.spiedigitallibrary.org/proceeding.aspx?doi=10.1117/12.552109 (visited on 13/02/2025).

[69] Oliver P. Lay, Stefan R. Martin and Sarah L. Hunyadi. 'Planet-finding performance of the TPF-I Emma architecture'. In: Optical Engineering + Applications. Ed. by Daniel R. Coulter. San Diego, CA, 13th Sept. 2007, 66930A. DOI: 10.1117/12.732230. URL: http://proceedings.spiedigitallibrary.org/proceeding.aspx?doi=10.1117/12.732230 (visited on 13/02/2025).

[70] A. Léger and T. Herbst. 'Darwin - Science Across Disciplines - A Proposal for the Cosmic Vision 2015-2025 ESA Plan'. In: (). URL: https://arxiv.org/pdf/0707.3385.

[71] C. Lovis et al. 'Atmospheric characterization of Proxima b by coupling the SPHERE high-contrast imager to the ESPRESSO spectrograph'. In: *Astronomy & Astrophysics* 599 (Mar. 2017), A16. ISSN: 0004-6361, 1432-0746. DOI: 10.1051/0004-6361/201629682. URL: http://www.aanda.org/10.1051/0004-6361/201629682 (visited on 12/03/2025).

[72] Lucas Viseur. 'Development of a performance modeling tool for nulling interferometry'. Université de Liège, 2024.

[73] Frantz Martinache and Michael J. Ireland. 'Kernel-nulling for a robust direct interferometric detection of extrasolar planets'. In: *Astronomy & Astrophysics* 619 (Nov. 2018), A87. ISSN: 0004-6361, 1432-0746. DOI: 10.1051/0004-6361/201832847. URL: https://www.aanda.org/10.1051/0004-6361/201832847 (visited on 23/02/2025).

[74] John W. Mason. *Exoplanets: detection, formation, properties, habitability*. Vol. 46. 1st Nov. 2008. URL: http://choicereviews.org/review/10.5860/CHOICE.46-1450 (visited on 06/02/2025).

[75] MATLAB. *fminbnd - Find local minimum of single-variable function on fixed interval*. 2006. URL: https://www.mathworks.com/help/matlab/ref/fminbnd.html.

[76] Bertrand Mennesson, Alain Léger and Marc Ollivier. 'Direct detection and characterization of extrasolar planets: The Mariotti space interferometer'. In: *Icarus* 178.2 (Nov. 2005), pp. 570–588. ISSN: 00191035. DOI: 10.1016/j.icarus.2005.05.012. URL: https://linkinghub.elsevier.com/retrieve/pii/S0019103505001843 (visited on 19/03/2025).

[77] Bertrand Mennesson and Jean Marie Mariotti. 'Array Configurations for a Space Infrared Nulling Interferometer Dedicated to the Search for Earthlike Extrasolar Planets'. In: *Icarus* 128.1 (July 1997), pp. 202–212. ISSN: 00191035. DOI: 10.1006/icar.1997.5731. URL: https://linkinghub.elsevier.com/retrieve/pii/S0019103597957316 (visited on 06/02/2025).

[78] *Miniature Motorized Actuators - Nanometer-Precision Actuators: Piezoelectric and Motorized Linear Motion for Nanometer Accuracy Applications*. URL: https://www.nanoactuators.com/nano-actuator.php.

[79] Gijs D. Mulders, Ilaria Pascucci and Daniel Apai. 'A stellar-mass-dependent drop in planet occurrence rates'. In: (2014). DOI: 10.48550/ARXIV.1406.7356. URL: https://arxiv.org/abs/1406.7356 (visited on 16/05/2025).

[80] *NASA. Keck Telescope*. URL: https://en.wikipedia.org/wiki/W._M._Keck_Observatory#/media/File:Kecknasa.jpg.

[81] *NASA. The Large Binocular Telescope Interferometer*. URL: https://assets.science.nasa.gov/dynamicimage/assets/science/astro/exo-explore/2023/09/lbti20150120-16.png?w=1600&h=900&fit=clip&crop=faces%2Cfocalpoint.

[82] National Aeronautics and Space Administration. *Astrobiology, Exoplanets and ROCKE-3D*. 3rd Apr. 2025. URL: https://www.giss.nasa.gov//projects/astrobio/.

[83] National Aeronautics and Space Administration. *NASA - Glossary*. In: 22nd Apr. 2024. URL: https://science.nasa.gov/exoplanets/glossary/.

[84] National Aeronautics and Space Administration. *NASA Exoplanet Archive*. 16th Apr. 2025. URL: https://exoplanetarchive.ipac.caltech.edu/cgi-bin/TblView/nph-tblView?app=ExoTbls&config=PS (visited on 18/04/2025).

[85] National Aeronautics and Space Administration. *What Is a Super-Earth? - A potentially rocky world, larger than Earth*. In: 28th Oct. 2024. URL: https://science.nasa.gov/exoplanets/super-earth/.

[86] Jerry Nelson and Gary H. Sanders. 'The status of the Thirty Meter Telescope project'. In: SPIE Astronomical Telescopes + Instrumentation. Ed. by Larry M. Stepp and Roberto Gilmozzi. Marseille, France, 27th Aug. 2008, 70121A. DOI: 10.1117/12.788238. URL: http://proceedings.spiedigitallibrary.org/proceeding.aspx?doi=10.1117/12.788238 (visited on 07/02/2025).

[87] Rogier Norbruis. 'Detecting exoplanets with a smallsat-based multi-aperture nulling interferometry telescope'. In: (2023).

[88] P. R. Lawson, O. P. Lay and alia. 'Terrestrial Planet Finder Interferometer (TPF-I) Whitepaper for the AAAC Exoplanet Task Force'. In: (2nd Apr. 2007).

[89] G. L. Pilbratt et al. '*Herschel* Space Observatory: An ESA facility for far-infrared and submillimetre astronomy'. In: *Astronomy and Astrophysics* 518 (July 2010), p. L1. ISSN: 0004-6361, 1432-0746. DOI: 10.1051/0004-6361/201014759. URL: http://www.aanda.org/10.1051/0004-6361/201014759 (visited on 07/02/2025).

[90] Pavel Pintr et al. 'Relative stellar occurrence of exoplanets in habitable zones of the main sequence F, G, K stars'. In: *Planetary and Space Science* 99 (Sept. 2014), pp. 1–6. ISSN: 00320633. DOI: 10.1016/j.pss.2014.06.001. URL: https://linkinghub.elsevier.com/retrieve/pii/S003206331400172X (visited on 16/05/2025).

[91] S. P. Quanz et al. 'Large Interferometer For Exoplanets (LIFE): I. Improved exoplanet detection yield estimates for a large mid-infrared space-interferometer mission'. In: *Astronomy & Astrophysics* 664 (Aug. 2022), A21. ISSN: 0004-6361, 1432-0746. DOI: 10.1051/0004-6361/202140366. URL: https://www.aanda.org/10.1051/0004-6361/202140366 (visited on 05/02/2025).

[92] Sascha P. Quanz et al. *Exoplanet science with a space-based mid-infrared nulling interferometer*. 2018. DOI: 10.48550/ARXIV.1807.06088. URL: https://arxiv.org/abs/1807.06088 (visited on 16/05/2025).

[93] Daniel Rouan. 'Ultra deep nulling interferometry using fractal interferometers'. In: *Comptes Rendus. Physique* 8.3 (1st Apr. 2007), pp. 415–425. ISSN: 1878-1535. DOI: 10.1016/j.crhy.2007.05.001. URL: https://comptes-rendus.academie-sciences.fr/physique/articles/10.1016/j.crhy.2007.05.001/ (visited on 16/05/2025).

[94] M. Schöller, R. Wilhelm and B. Koehler. 'Modeling the imaging process in optical stellar interferometers'. In: *Astronomy and Astrophysics Supplement Series* 144.3 (June 2000), pp. 541–552. ISSN: 0365-0138, 1286-4846. DOI: 10.1051/aas:2000229. URL: http://aas.aanda.org/10.1051/aas:2000229 (visited on 11/03/2025).

[95] E. Serabyn and M. M. Colavita. 'Fully symmetric nulling beam combiners'. In: *Applied Optics* 40.10 (1st Apr. 2001), p. 1668. ISSN: 0003-6935, 1539-4522. DOI: 10.1364/AO.40.001668. URL: https://opg.optica.org/abstract.cfm?URI=ao-40-10-1668 (visited on 19/02/2025).

[96] E. Serabyn et al. 'Deep nulling of visible laser light'. In: *Applied Optics* 38.34 (1st Dec. 1999), p. 7128. ISSN: 0003-6935, 1539-4522. DOI: 10.1364/AO.38.007128. URL: https://opg.optica.org/abstract.cfm?URI=ao-38-34-7128 (visited on 19/02/2025).

[97] Eugene Serabyn. 'Nulling interferometry: symmetry requirements and experimental results'. In: Astronomical Telescopes and Instrumentation. Ed. by Pierre J. Lena and Andreas Quirrenbach. Munich, Germany, 5th July 2000, p. 328. DOI: 10.1117/12.390223. URL: http://proceedings.spiedigitallibrary.org/proceeding.aspx?doi=10.1117/12.390223 (visited on 19/02/2025).

[98] Keto Soosaar. 'DESIGN OF OPTICAL MIRROR STRUCTURES'. In: ().

[99] Tim Stephens. 'Radioactive elements may be crucial to the habitability of rocky planets'. In: (10th Nov. 2020). URL: https://news.ucsc.edu/2020/11/planet-dynamos/.

[100] Synopsys. *CODE V*. Version 2024. URL: www.synopsys.com.

[101] Synopsys. *CODE V Macro-PLUS*. Version 2024. 2024.

[102] J.Y. Tien et al. 'Formation acquisition sensor for the terrestrial planet finder (TPF) mission'. In: *2004 IEEE Aerospace Conference Proceedings (IEEE Cat. No.04TH8720)*. 2004 IEEE Aerospace Conference Proceedings (IEEE Cat. No.04TH8720). Vol. 4. Big Sky, MT, USA: IEEE, 2004, pp. 2680–2690. ISBN: 978-0-7803-8155-1. DOI: 10.1109/AERO.2004.1368063. URL: http://ieeexplore.ieee.org/document/1368063/ (visited on 25/02/2025).

[103] John T. Trauger and Wesley A. Traub. 'A laboratory demonstration of the capability to image an Earth-like extrasolar planet'. In: *Nature* 446.7137 (Apr. 2007), pp. 771–773. ISSN: 0028-0836, 1476-4687. DOI: 10.1038/nature05729. URL: https://www.nature.com/articles/nature05729 (visited on 07/02/2025).

[104] Brent Ware and Curt Henry. 'Modeling the TPF interferometer'. In: SPIE Astronomical Telescopes + Instrumentation. Ed. by Simon C. Craig and Martin J. Cullum. USA, 16th Sept. 2004, p. 193. DOI: 10.1117/12.550265. URL: http://proceedings.spiedigitallibrary.org/proceeding.aspx?doi=10.1117/12.550265 (visited on 25/02/2025).

[105] M W Werner et al. 'The Spitzer space telescope mission'. In: (2004).

[106] Xiaobin Zhang et al. 'Optical compensation for the perturbed three mirror anastigmatic telescope based on nodal aberration theory'. In: *Optics Express* 25.11 (29th May 2017), p. 12867. ISSN: 1094-4087. DOI: 10.1364/OE.25.012867. URL: https://opg.optica.org/abstract.cfm?URI=oe-25-11-12867 (visited on 09/05/2025).